DUAL-ELECTRODE CAPACITIVE MICROMACHINED ULTRASONIC TRANSDUCERS FOR MEDICAL ULTRASOUND APPLICATIONS

A Dissertation
Presented to
The Academic Faculty

By

Rasim O. Guldiken

In Partial Fulfillment
Of the Requirements for the Degree
Doctor of Philosophy in the
Mechanical Engineering

Georgia Institute of Technology

December 2008

DUAL-ELECTRODE CAPACITIVE MICROMACHINED ULTRASONIC TRANSDUCERS FOR MEDICAL ULTRASOUND APPLICATIONS

Approved by:

Dr. F. Levent Degertekin, Chair
School of Mechanical Engineering
Georgia Institute of Technology

Dr. Yves Berthelot
School of Mechanical Engineering
Georgia Institute of Technology

Dr. Paul Benkeser
Department of Biomedical Engineering
Georgia Institute of Technology

Dr. Oliver Brand
School of Electrical and Computer Engineering
Georgia Institute of Technology

Dr. Peter Hesketh
School of Mechanical Engineering
Georgia Institute of Technology

Date Approved: July 30th 2008

ACKNOWLEDGEMENTS

Most of my sincere thanks go to my Ph.D advisor – Professor F. Levent Degertekin – for his undisputed expertise in his field, his wise technical suggestions, his friendship and his faith in me. I also would like to thank my thesis committee members – Professors Yves Berthelot, Paul Benkeser, Oliver Brand and Peter Hesketh – for serving on my committee and their constructive feedback throughout the course of this study.

I also would like to thank all MIST group members for their help, support, friendship and technical discussions. I especially thank Jaime Zahorian for help with fabrication, experimental characterization and reviewing my dissertation, Dr. Mujdat Balantekin for electronics design and imaging experiments, M. Shakeel Qureshi and Gokce Gurun for IC chip and CMOS wafer design.

I owe special thanks to Gary Spinner and all MiRC cleanroom staff for keeping the equipments in excellent condition and addressing fabrication related issues promptly. This thesis couldn't have been completed without them. Professor Mustafa Karaman from Isik University, Turkey, is greatly acknowledged for his guidance, help with imaging experiments and reviewing my dissertation. I also would like to thank National Institutes of Health (NIH) and Boston Scientific Corporation for financial support of this research.

Last but not least, I would like to thank my wife, Burcu. Words are ineffective to show my gratitude to you. Thanks for being part of my life, thanks for making every moment of my life memorable…This thesis is dedicated to you…

TABLE OF CONTENTS

LIST OF TABLES

LIST OF FIGURES

SUMMARY

Capacitive Micromachined Ultrasonic Transducers (CMUTs) have been introduced as a viable alternative to piezoelectric transducers in medical ultrasound imaging in the last decade. CMUTs are especially suitable for applications requiring small size such as catheter based cardiovascular applications. Despite these advantages and their broad bandwidth, earlier studies indicated that the overall sensitivity of CMUTs need to be improved to match piezoelectric transducers. This dissertation addresses this issue by introducing the dual-electrode CMUT concept. Dual electrode configuration takes advantage of leveraged bending in electrostatic actuators to increase both the pressure output and receive sensitivity of the CMUTs.

Static and dynamic finite element based models are developed to model the behavior of dual-electrode CMUTs. The devices are then successfully fabricated and characterized. Experiments illustrate that the pulse echo performance is increased by more than 15dB with dual-electrode CMUTs as compared to single electrode conventional CMUT. Further device optimization is explored via membrane shape adjustment by adding a center mass to the design. Electromechanical coupling coefficient (k_c^2) is investigated as a figure of merit to evaluate performance improvement with non-uniform/uniform membrane dual-electrode CMUTs. When the center mass is added to the design, the optimized non-uniform membrane increases the electromechanical coupling coefficient from 0.24 to 0.85 while increasing one-way 3dB fractional bandwidth from 80% to 140% and reducing the DC bias requirement from 160V to

132V. The results of this modeling study are successfully verified by experiments. With this membrane shape adjustment, significant performance improvement (nearly 20dB) is achieved with the dual-electrode CMUT structure that enables the CMUT performance to exceed that of piezoelectric transducers for many applications.

CHAPTER 1

BACKGROUND AND MOTIVATION

1.1 Medical Ultrasound Imaging

Ultrasonics is the study of sound waves with frequencies above the human ear's audible range – 20KHz. Medical ultrasound imaging is one of the most widely used diagnostic tools in modern medicine. The technology is relatively inexpensive and portable as compared to its alternatives: X-Ray, Computed Tomography (CT), and Magnetic Resonance Imaging (MRI). It is a safe test because it does not use ionizing radiation, which imposes hazards such as causing cancer [1]. Medical ultrasound imaging modality has unique advantages such as revealing the anatomy, obtaining the blood flow information, dynamic imaging of the abdominal organs, heart, and vessels in real time [2]. These unique advantages allow realization of many applications. For instance, ultrasonic imaging makes Intravascular Ultrasound (IVUS) – imaging of coronary arteries – possible as image stability problems associated with heart beating is minimized with real time imaging. In medical ultrasound imaging, the transmitter transducer generates waves; the waves travel through the medium of interest and reflect from organ and tissue boundaries (such as the vessel wall or bone). The reflected waves travel back to the transducer and are detected by receiver transducer. In most applications where area is limited by physical constraints, a single transducer is used both as transmitter and receiver. As a result, the transducer operates in two separate modes: transmit mode to generate the waves and receive mode to detect the incoming waves. The most common and well known application of medical ultrasound imaging is detecting a fetus in the

mother's womb (sonography) as illustrated in brightness mode (B-mode) in Figure 1. In this figure, the ultrasonic transducer is located above the image and the scale on the left side indicates the distance (depth) from the transducer. By convention, the brighter points in the image indicate high reflection boundaries such as bones, and darker regions indicate low reflectors such as blood [3]. Note that strong reflectors such as bone do not allow sufficient ultrasonic energy to pass through that is necessary to image further depths. This common phenomenon is observed in Figure 1 as the skull shadows the imaging of the brain. Ultrasonics is the only diagnostic tool for fetus imaging as it does not use radiation that causes chromosome breakage [2]. In the following sections, current transducer technologies in the medical ultrasonic imaging will be discussed.

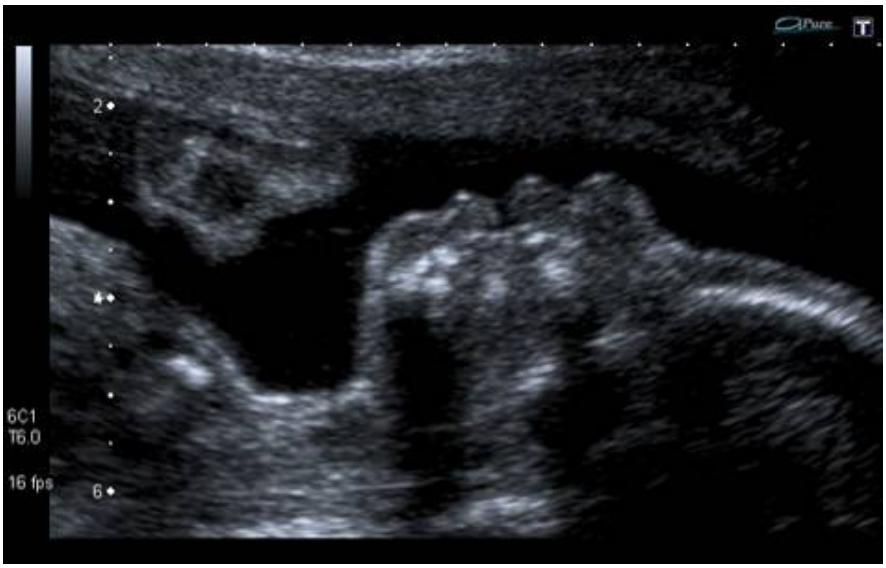

Figure 1 Ultrasonic image of a fetus in the mother's womb [4]

1.1.1 Intravascular Ultrasound (IVUS) & Intracardiac Echocardiography (ICE)

In the United States, coronary heart disease was the number one cause of death and claimed more than 525,600 lives in 2007 [5]. To this end, ultrasonic imaging catheters are used to inspect coronary arteries that supply blood to the heart (ICE) and heart muscles (IVUS).Ultrasonic catheters are also used for imaging and placement of stent and balloon. Figure 2 (a) and (b) illustrates the IVUS image of a coronary arteries. Both images show the imaging transducer (region A), the lumen where the blood flows (region B) and the vessel wall (region C). However, Figure 2 (b) has an extra region in the image illustrated by region D – the lipid layer – which clearly reduces the active area for blood flow. When the lipid layer completely occludes the blood flow, the heart muscle can not receive enough oxygen that is necessary to pump the blood. This phenomenon is called myocardial infarction (heart attack). Although the lipid formation first occurs outside of the vessel before forming inside of the vessel wall, the outside of the vessel cannot be imaged due to limited resolution (as can be seen from Figure 2) even with the current state of the art ultrasonic transducer technology [6]. Increasing the resolution and penetration depth is one of the motivations for this thesis.

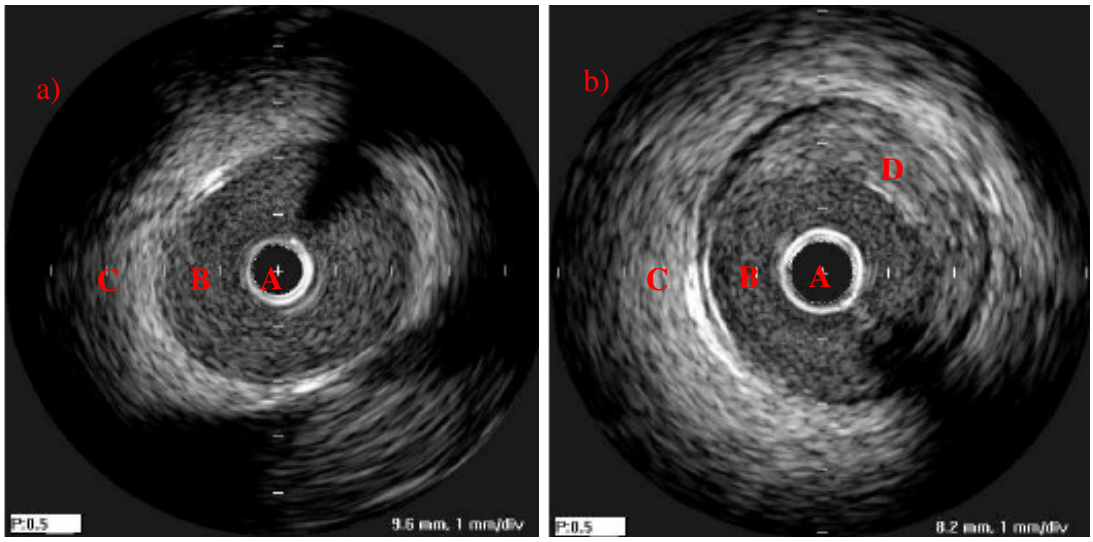

Figure 2 Ultrasonic image of a)healthy coronary artery b) coronary artery with lipid formation as indicated by region D [7].

1.2 Transducer Technologies in Medical Ultrasound Imaging

1.2.1 Piezoelectric Transducers

Piezoelectricity is the ability of a material to generate an internal electric field when subjected to mechanical stress/strain. Piezoelectric materials can be used as an ultrasonic transducer operating in receive mode, as the deflection of the piezoelectric material caused by the incoming waves is transferred to measurable electric field. The piezoelectricity effect was discovered by Curie Brothers in 1880 [8]. Piezoelectric materials also exhibit the reverse piezoelectric effect which is the production of stress/strain when an electric field is applied. This reverse piezoelectric effect allows a piezoelectric transducer to act as a transmitter, since an applied field (voltage) generates strain in the material which is coupled to the medium. Piezoelectric transducer technology currently dominates medical ultrasonic imaging [6, 9]. There are two variations for transducer array configuration for IVUS and ICE: phased array and rotating

array. In the phased array configuration, side looking array elements (typically consisting of 64 elements) are used for imaging (Figure 3 (a)). In this imaging mode, at one time, a single array element is used as a transmitter and the signal is received from the remaining array elements. This procedure is repeated for each array element acting as transmitter. Alternatively, in the rotating array configuration, there is only one transmitter/receiver element located at the tip of the catheter facing the side vessel wall which is rotated fast enough to obtain real time image of the entire vessel wall (Figure 3 (b)).

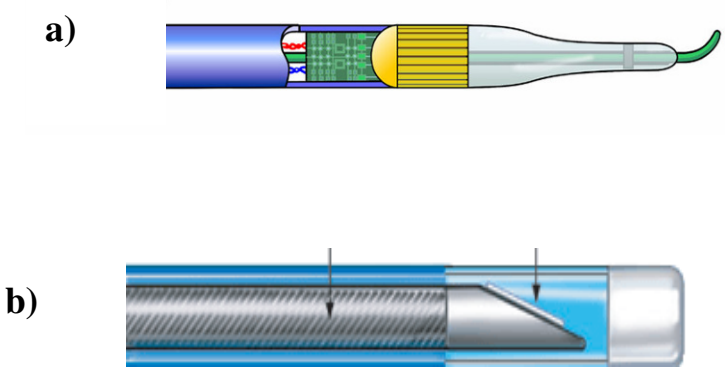

Figure 3 Illustration of a) phased array ultrasonic imaging catheter [10] b) Rotating array ultrasonic imaging catheter [11].

Although piezoelectric based ultrasonic catheters have long dominated the medical ultrasonic imaging arena, this mature technology has reached its limits in some applications requiring small area implementation such as IVUS and ICE. One of the limitations of piezoelectric transducers is the coupling coefficient which is an efficiency measure of energy transfer between the electrical and mechanical domain, the higher the coupling coefficient, the higher the performance of the transducer. On the other hand, the

mechanical impedance of the piezoelectric transducer is very high compared to that of typical media for ultrasound waves. For instance, the impedance of water ($1.5x10^6$ kg/m^2s) is much smaller than that of a typical piezoelectric material (~ $30x10^6$ kg/m^2s). Therefore, a suitable matching layer should be inserted in front of the transducer for effective energy transfer [8, 12]. However, an inherent problem of these matching layers is their effectively narrow frequency band. In addition, unrealizable thickness and un-availability of matching layer materials required for very high frequency operation are significant problems. Even with proper matching layers, the bandwidth of high impedance piezoelectric material is limited. This is a significant drawback as the bandwidth of the transducers determines the lateral resolution of the image. Also, dicing brittle piezoelectric ceramics for small area implementation is both expensive and cumbersome especially for element sizes below 200μm. As a result, due to area constraint, current piezoelectric transducer based catheters lack forward looking capability [13]. This is a significant disadvantage as there is no guidance capability and completely occluded arteries cannot be imaged.

1.2.2 Capacitive Micromachined Ultrasonic Transducers (CMUTs)

Some of the problems of piezoelectric transducer technology can be addressed by using a thin membrane with capacitive actuation to generate ultrasonic waves. The main advantage of this alternative is the small impedance of the thin membrane that vibrates to generate or detect ultrasonic waves. Low impedance of the ultrasonic generator eliminates the need for matching layers. Furthermore, bandwidth of low impedance materials are significantly higher than that of a high impedance materials [14-16].

Although the idea of electrostatic transducers is as old as piezoelectric transducers, the electric field requirements, on the order of million volts per centimeter, made them unrealizable for decades [17]. Actually, there have been publications using capacitive transducers for air applications as early as the 1950's [18] and the late 1970's for immersion applications [19]. However those devices were operating in the KHz to low MHz range with low efficiencies with respect to piezoelectric transducers due to limited electric field strengths. Recent advances in the microfabrication technology have allowed fabrication of tiny evacuated distances between the electrodes enabling GV/m electric fields. A capacitive ultrasonic transducer taking advantage of micromachining was introduced by Haller and Khuri-Yakub that can compete with piezoelectric transducers in terms of transducer efficiency with higher bandwidth [20]. It is commonly referred as Capacitive Micromachined Ultrasonic Transducer (CMUT). As illustrated in Figure 4, the CMUT has a top electrode buried in its compliant membrane. The membrane is separated from the substrate with a gap.

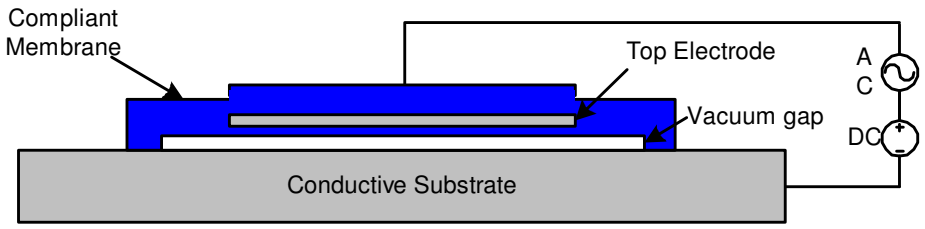

Figure 4 One-dimensional scaled rendering of CMUT

During both transmit and receive modes of operation, a DC bias is applied to increase the sensitivity and linearity of the response. During transmit mode, an AC pulse is applied along with a DC bias to vibrate the membrane for generating waves that can

couple to the medium of interest. During receive mode, the waves hitting the membrane cause the membrane to deflect (capacitance change) which causes a detectable output current. By proper design and taking advantage of the microfabrication techniques to manufacture optimized structures, CMUTs can provide wide bandwidth and high coupling efficiency which are important figures of merit for traditional transducer evaluation. Additionally, CMUTs are very advantageous for applications where space is limited and array implementation is required such as IVUS and ICE. Note that at 20 MHz, the wavelength in water is only 75μm and for the phased array imaging mode, the lateral dimension of the transducer should be half the wavelength according to the Nyquist criteria in aperture sampling [21]. Hence, for such applications involving small physical sizes, piezoelectric transducer implementation is a more formidable and costly task than the microfabrication alternative. In addition, CMUTs offer advantages such as ease of manufacturing, on chip electronics integration, CMOS compatibility, low cost (batch fabrication), high yield, and reliability due to microfabrication implementation. As material and dielectric losses associated with the CMUT membrane are smaller compared to piezoelectric materials, the thermal performance of CMUTs is expected to be better [22]. In addition, the membranes can be vacuum sealed, hence, CMUTs can be used both in air and immersion applications. In the late 1990's and early 2000's, there has been extensive research about the design and modeling [14, 15, 20, 23-33]; fabrication and experimental characterization of this new transducer technology [13, 34-39]. Furthermore, there have been several successful array implementations by CMUTs [40, 41] especially for forward looking intravascular imaging (FL-IVUS) applications [42-46] (see Figure 5).

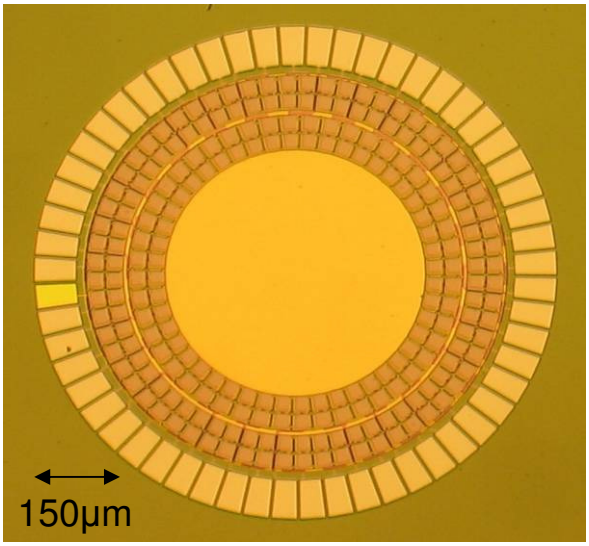

Figure 5 Micrograph of a completed CMUT array for forward looking IVUS imaging [47]. The outmost ring is the bondpads, while mid ring and inner ring is receive and transmit rings respectively.

Despite this initial success, when real-time in vivo images obtained by 1-D CMUT arrays were compared with the ones acquired by piezoelectric transducer array, the results suggested that although CMUTs offer superior performance in terms of bandwidth, their overall sensitivity is inferior as compared to piezoelectric transducers by about 10dB, especially due to lower output pressure [48, 49]. The CMUT output pressure, limited by the available gap thickness was noted as the main reason for this performance gap.

It is well known that electrostatic parallel plate devices have a limited actuation range due to the collapse (pull-in) phenomenon [50]. The electrostatic collapse of the parallel-plate structure occurs when the movable membrane travels 1/3 of the gap, leaving 2/3 of the gap region unusable. This collapse phenomenon will be discussed in detail in Chapter 2. Although the electrode size can be optimized, this phenomenon

ultimately limits receive sensitivity which requires smaller gaps. Membrane collapse also limits the output pressure of the CMUT as one needs a large gap to improve the displacement range of the membrane. Consequently, this single electrode structure creates a conflict in gap optimization; in receive mode, a small gap is advantageous since it results in higher capacitance change for small displacements —higher sensitivity; while in transmit mode, large gaps are needed for higher output pressure.

As a drastic and effective way to overcome this limitation, CMUTs have been operated in collapse-snap back mode where the CMUT membrane is brought in and out of contact to the substrate every transmission cycle to maximize the volumetric displacement [51]. Although the collapse-snap back mode successfully increases the maximum transmit pressure by about 4 dB [52] to 6dB [53], this mode can be problematic due to the uncontrolled nature of the output signals, and the reliability issues due to frequent membrane-substrate contact. Moreover, adjusting the membrane shape has been investigated by several groups. One method is placing a center mass on the CMUT membrane [13, 54, 55] . With this design change, the transduction performance is increased 2dB (out of 10dB). Another approach is introducing notches to the design to increase receive sensitivity and output pressure [56, 57]. Although a 5dB increase in transduction performance is reported by simulations (when 4 trenches are employed in design), the results should be verified by experimental studies.

In this thesis, the dual-electrode CMUT design implementation that addresses the performance gap between CMUT and piezoelectric transducers is presented. The dual-electrode structure uses three electrodes in the CMUT membrane where the two side electrodes are connected in parallel to form transmit/membrane shape electrode while the

center electrode is reserved for the receive mode of operation (see Figure 6). Using the side electrode actuation increases the CMUT membrane motion from 1/3 of the gap to almost full gap without collapsing the membrane, which results in increased transmit pressure. Moreover, during receive mode, the membrane shape can be adjusted by the side electrodes so that center receive electrode is brought closer to the bottom electrode which results in higher sensitivity. Furthermore, as the side electrodes are used for transmit and center electrode are used for receive mode of operation, this results in simplified electronics.

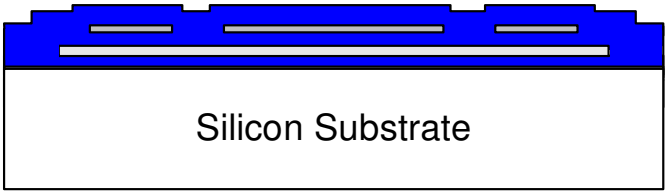

Figure 6 One-dimensional scaled rendering of a dual-electrode CMUT

In Chapter 2, analytical models of CMUT are introduced and a small signal equivalent circuit is discussed also, relevant figures of merit such as coupling coefficient and transformer ratio are derived. With this preliminary knowledge, the dual-electrode concept is explained in detail. After the finite element simulations are presented in Chapter 3, the design and optimization of dual-electrode CMUTs are discussed in Chapter 4. In Chapter 5, the fabrication process is presented and CMUT-on-CMOS implementation is introduced. Then, in Chapter 6, experimental characterization and model verifications are presented. Chapter 7 concludes this thesis by summary and recommendations.

CHAPTER 2

CONVENTIONAL AND DUAL-ELECTRODE CMUT CONCEPTS

In this chapter, CMUT operation principles, and the equivalent circuit of a CMUT are introduced first. The equivalent circuit analysis enables us to define the figures of merit that measure the transducer performance. After these concepts are developed, dual-electrode CMUT concepts will be presented, and the derived figures of merit will be used to quantify receive and transmit modes of operation performance improvements.

2.1 Operation Principle of CMUTs

To understand the operation of CMUTs, analytical models that were originally developed for parallel plate electrostatic actuators will be used. Although the parallel plate electrostatic actuator does not capture the bending of the membrane or deflection of the membrane edges with applied voltage, it provides a first order approximation and understanding of the CMUT operation. CMUT is essentially a complaint membrane device which deforms under the electrostatic forces generated by the electrode embedded in the membrane itself and substrate. A first order model consisting of spring-mass-dashpot (Figure 7) can be used to model the behavior of the membrane under load. The dashpot, as illustrated in Figure 7, adds dynamic response to the membrane and can be neglected as static response is the main interest in this section. As a result, this first order approximation can further be simplified to an equation of two forces on the membrane, namely the electrostatic force and the spring force.

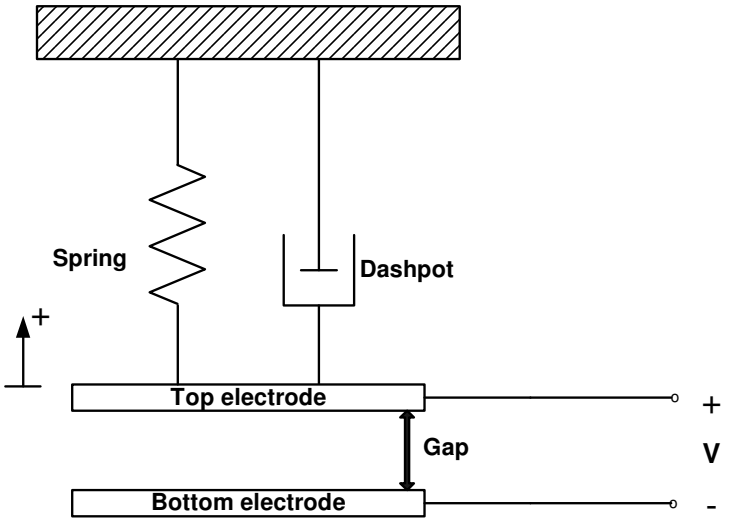

Figure 7 Illustration of the first-order model for a CMUT membrane

The electrostatic force on the membrane is given by

$$F_{electrostatic} = -\frac{\varepsilon \cdot A \cdot V^2}{2 \cdot g^2} \quad \textbf{(1)}$$

where ε is the permittivity of material between the capacitance plates, A is the cross sectional area of the plate, V is the applied DC voltage, and g is the distance between the top and bottom plate while deformed under applied bias (V). The negative sign in front of the equation comes from the fact that when bias is increased, the distance between plates is reduced and the electrostatic force is increased in the negative direction (as indicated by Figure 7). The first order approximation for spring force is given by:

$$F_{spring} = k \cdot (g_0 - g) \quad \textbf{(2)}$$

where k is the spring constant of the membrane, g_o is the initial distance between top and bottom plate without applied DC bias. Note that when bias is increased, the gap (g) becomes smaller; hence, the spring force increases in the positive direction (as indicated by Figure 7). Figure 8 illustrates the electrostatic and spring force as a function of normalized gap thickness to initial gap thickness when actuated by 60% of its collapse voltage. Note that when electrostatic and spring forces are equal in magnitude, the net force on the membrane is zero. As a result, the membrane is at its equilibrium point. One can observe from Figure 8 that there are two displacements where the electrostatic and spring forces are equal and opposite in direction, namely point A and point B. However, for point B, when the equilibrium is disturbed in such a way to increase the displacement, the electrostatic force becomes more than the spring force. Hence the membrane displacement does not return back to its equilibrium point, rather it further increases the displacement. As a result, although point B is mathematically a solution to the equivalency of spring and electrostatic forces, it is an un-steady equilibrium point. On the other hand, for point A, when the equilibrium is disturbed in a way to increase the displacement, the spring force becomes more than the electrostatic force, and the membrane is pushed back to its equilibrium. Similar behavior is observed when the equilibrium is disturbed to reduce the displacement: the force balance increases the displacement to its equilibrium point. As a result, point A is the only steady equilibrium point.

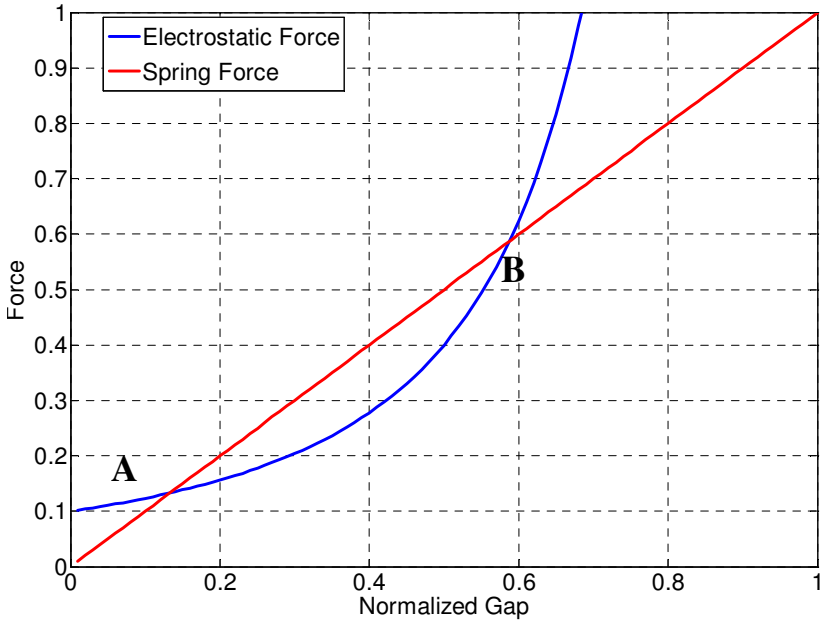

Figure 8 Analytical electrostatic and spring forces as a function of normalized gap with a normalized DC bias of 60% of the collapse voltage

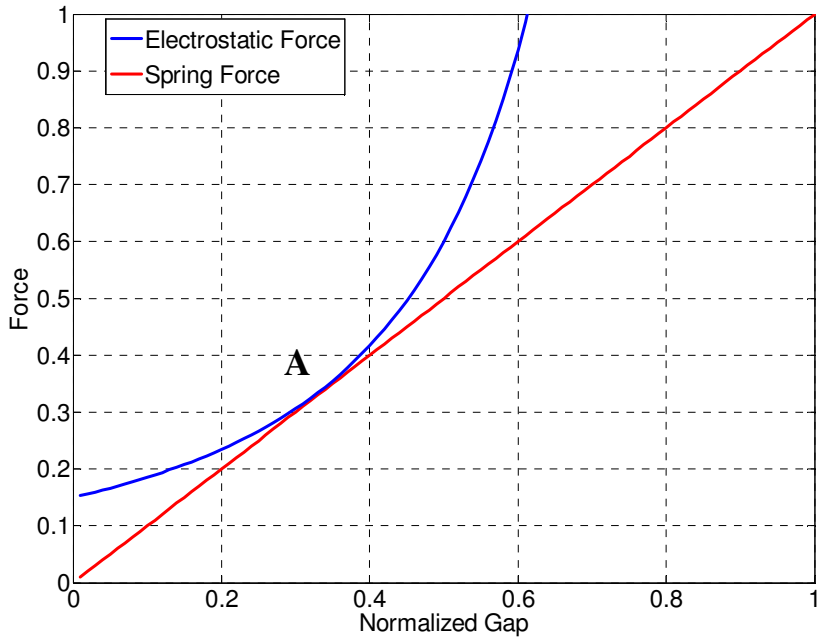

Figure 9 Analytical electrostatic and spring forces as a function of the gap with collapse voltage DC bias

When the voltage is increased, the spring force as a function of normalized gap stays the same as the spring force is independent of the bias but depends only on the displacement. On the other hand, as the electrostatic force has square dependence on voltage, the electrostatic force increases. As a result, when the voltage reaches a certain value, the equilibrium points of force equivalency reduces to one, as illustrated by point A in Figure 9. This maximum voltage that can be applied to the membrane is commonly referred as collapse or pull-in voltage. Note that the displacement of the membrane at this voltage is 1/3 of the gap as observed in Figure 9.

$$g_{col} = \frac{2 \cdot g_o}{3} \tag{3}$$

At this maximum displacement, when forces in (1) and (2) are equated, by using (g) as given in equation (3), the collapse voltage is obtained as:

$$V_{col} = \sqrt{\frac{8 \cdot k \cdot g_o^{\,3}}{27 \cdot \varepsilon_o \cdot A}} \tag{4}$$

When the bias is increased further, there exists no equilibrium point where the electrostatic force and spring force are equal. As a result, when the normalized gap is plotted as a function of applied bias normalized to collapse voltage, Figure 10 is obtained. One can observe from this figure that the membrane displacement has a non-linear response to applied bias for displacements less than 1/3 of the gap. Actually, when the voltage is increased beyond the collapse voltage, the membrane simply collapses to the bottom substrate. Hence, there is no stable operation point for displacements exceeding 1/3 of the gap. As a result, both the maximum displacement of the membrane and the

minimum gap height (maximum capacitance) are limited. This puts an upper limit to achievable performance for both transmit and receive modes. Also, to bring the membrane back from the collapsed state, applied bias should be reduced below the snap-back voltage and as a result the displacement versus voltage curve has a hysteresis. This snap-back voltage can be calculated by using equations (1) and (2) and inserting (g) as zero.

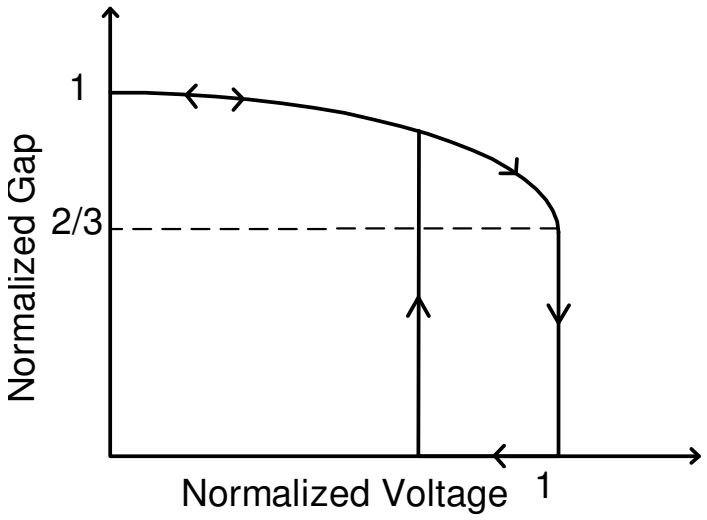

Figure 10 Analytical membrane displacement as a function of normalized bias

2.1.1 Equivalent Circuit Model

The Mason equivalent circuit model is a useful tool to evaluate the overall performance of the CMUT. It is based on a small signal model for parallel plate transducers [58]. There are two separate equivalent circuits for transmit and receive operation modes of CMUTs. Figure 11 shows the transmit mode equivalent circuit for CMUTs.

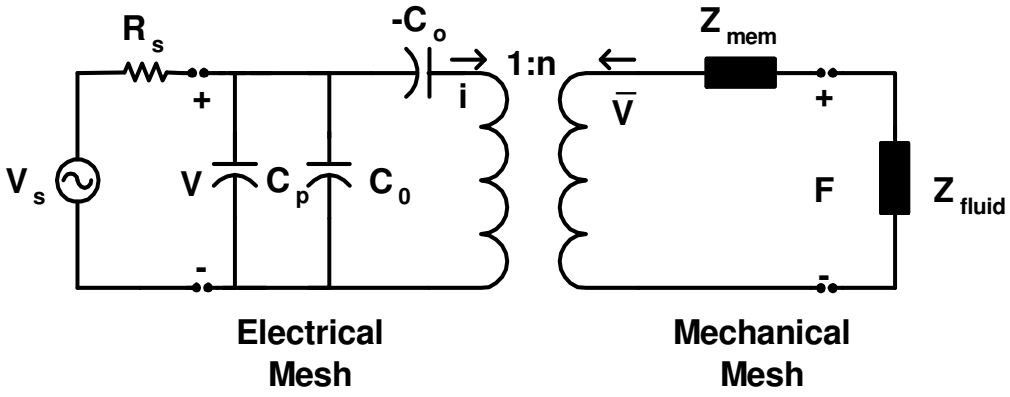

Figure 11 Parallel plate electrical equivalent circuit of the CMUT operating in immersion.

CMUT is basically an energy converting transducer between mechanical and electrical domains. When it operates as a transmitter, the applied electrical AC energy is converted to the vibration of the membrane; when it operates as a receiver, the vibration on the membrane caused by the incoming waves are converted to a measurable change in current. This energy conversion is represented by the transformer with a transformer ratio "*n*". In this representation, the current in the electrical domain corresponds to membrane velocity in the mechanical domain while the voltage in the electrical domain corresponds to force in the mechanical domain. In the mechanical domain, there are two impedances in series with each other, the membrane impedance (Z_{mem}) and medium impedance (Z_{fluid}). The mechanical impedance of the membrane can be modeled by a mass-spring-dashpot system as illustrated in Figure 7. The analytical mechanical impedance is derived for circular CMUTs [24]. In the electrical domain, there are three energy storage elements: The static capacitance of the membrane with applied DC bias (C_o), the negative

imaginary device capacitance that models the spring softening effect ($-C_o$), and the parasitic capacitance that is caused by the overlapping electrical connections and ground plane (C_p). In transmit mode of operation, as high voltage is directly applied to the transducer, the parasitic capacitance is of little concern. On the other hand, for receive mode of operation, to detect small capacitance changes, special attention should be given to minimize parasitic capacitance. For a parallel plate capacitor, capacitance can be defined as

$$C = \frac{\varepsilon_o \cdot \varepsilon_r \cdot A}{g} \tag{5}$$

where ε_o is the permittivity of free space, ε_r is the relative permittivity of the material between conductor plates, A is the area of the capacitor plates, and g is the distance between capacitor plates.

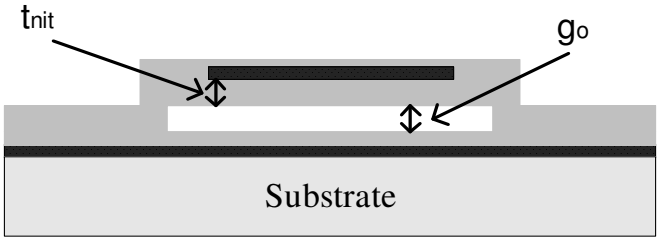

Figure 12 Cross-section of a CMUT illustrating the layers between top and bottom capacitor plates

One can observe from Figure 12 that there are two layers between top and bottom electrodes of CMUT, nitride isolation (t_{nit}) and gap (g_o). These two layers form a series capacitance where C_{nit} and C_{gap} are represented respectively as

$$C_{nit} = \frac{\varepsilon_o \cdot \varepsilon_r \cdot A}{t_{nit}} \tag{6}$$

and

$$C_{gap} = \frac{\varepsilon_o \cdot A}{g} \tag{7}$$

Note that relative permittivity (ε_r) is 1 for vacuum. These two capacitances can be simplified to a single capacitance with an effective gap, g_{eff}, and relative permittivity (ε_r) of 1. As a result the following equations are obtained:

$$C_o = \frac{\varepsilon_o \cdot A}{g_{eff}} \tag{8}$$

where

$$g_{eff} = g + \frac{t_{nit}}{\varepsilon_r} \tag{9}$$

In transmit mode of operation, an AC voltage, V_{AC}, is applied in addition to DC bias voltage, V_{DC}. Hence, the voltage applied can be written as:

$$V = V_{AC} + V_{DC} \tag{10}$$

V_{AC} can be written as a harmonic function with frequency ω

$$V_{AC} = V_o \cdot \cos(\omega \cdot t) \tag{11}$$

From equation (1), the electrostatic force on the CMUT membrane is proportional to the square of the applied voltage:

$$F_{electrostatic} = -\frac{\varepsilon_o \cdot A \cdot V^2}{2 \cdot g_{eff}^{\ 2}} \propto V^2 \tag{12}$$

The square of the total voltage is calculated as:

$$V^2 = {V_{DC}}^2 + 2 \cdot V_{DC} \cdot V_o \cdot \cos(\omega \cdot t) + (V_o \cdot \cos(\omega \cdot t))^2 \quad \textbf{(13).}$$

When equation (13) is substituted into equation (12), the electrostatic force on the CMUT membrane is found as

$$F_{electrostatic} = \frac{\varepsilon_o \cdot A}{2.(g + \frac{t_{nit}}{\varepsilon_r})^2} \left[\frac{V_o}{2} + {V_{DC}}^2 + 2 \cdot V_{DC} \cdot V_o . \cos(\omega \cdot t) + V_o \cdot \cos(2 \cdot \omega \cdot t) \right] \quad \textbf{(14)}$$

Now, from equation (14); there are three voltage components that generate the electrostatic force, DC bias, V_{DC}, AC component with frequency ω, and another AC component with frequency 2ω. To linearize the response of the transducer, the effect of second harmonic AC component should be limited. To do this, typically the AC signal amplitude is kept much lower than the DC bias voltage. Note that the maximum DC bias that can be applied is limited by the collapse phenomenon. In the case of $V_{DC} >> V_{AC}$, time varying linear force on the membrane is calculated from equation (14) by:

$$F_{AC} \cong \frac{\varepsilon_o \cdot A \cdot V_{DC}}{(g + \frac{t_{nit}}{\varepsilon_r})^2} \cdot V_o \cdot \cos(\omega . t) \quad \textbf{(15)}$$

Referring to the transmit equivalent circuit shown in Figure 11, the transformer ratio is the ratio of the force at the mechanical mesh to the voltage at the electrical mesh. Therefore, the transformer ratio of the equivalent circuit is obtained as:

$$n = \frac{F_{AC}}{V_{AC}} = \frac{\varepsilon_o \cdot A \cdot V_{DC}}{(g + \frac{t_{nit}}{\varepsilon_r})^2} = \frac{\varepsilon_o \cdot A}{g + \frac{t_{nit}}{\varepsilon_r}} . \frac{V_{DC}}{g + \frac{t_{nit}}{\varepsilon_r}} = C_o \cdot E \quad \textbf{(16)}$$

where E is the electric field between the top membrane electrode and bottom electrode. One can observe from equation (16) that at a given DC bias, the transformer ratio is inversely proportional to the square of the effective gap thickness, g_{eff}.

$$n \propto V_{DC} \propto \frac{1}{g_{eff}^{\ 2}} \tag{17}$$

On the other hand, given the design of the CMUT with fixed gap thickness, the transformer ratio is linearly proportional to the applied DC bias, hence the bias should be increased to close to collapse not only to linearize the response but also to increase the efficiency of the transducer. Now, it is interesting to observe that at collapse, when the expression of V_{col} in equation (4) is substituted into equation (16), the transformer ratio at collapse is found as:

$$n = \sqrt{\frac{8 \cdot k \cdot \varepsilon_o \cdot A \cdot g_o^{\ 3}}{27 \cdot (\frac{2g_o}{3} + \frac{t_{nit}}{\varepsilon_r})^2}} \tag{18}$$

Note that the transformer ratio is not dependent on the value of collapse voltage but only on the initial gap thickness and nitride isolation thickness. Moreover, the maximum achievable transformer ratio is inversely proportional to the square root of initial gap:

$$n \propto \frac{1}{\sqrt{g_o}} \tag{19}$$

Hence smaller an initial gap height results in a more efficient transducer.

2.1.2 Electromechanical Coupling Coefficient

The CMUT converts electrical energy to mechanical energy in transmit mode of operation and mechanical energy to electrical energy in receive mode of operation. Electromechanical coupling coefficient (k_c^2) is a measure of mechanical energy delivered to the load to the total energy stored in the transducer:

$$k_c^{\,2} = \frac{E_{mech}}{E_{total}} = \frac{E_{mech}}{E_{mech} + E_{elec}} \tag{20}$$

The electromechanical coupling coefficient is an important parameter because it measures the degree of energy coupling from the electrical to mechanical domain. Moreover, for piezoelectric transducers, the transducer bandwidth is related to the coupling coefficient (k_c^2) [8]. The electromechanical coupling coefficient for a parallel plate actuator is derived from equivalent circuit analysis [50] and written here as a reference:

$$k_c^{\,2} = \frac{Q_o^{\,2}}{\varepsilon \cdot A \cdot k \cdot g_o} \tag{21}$$

where Q_o is the total charge on the capacitor plates, and k is the stiffness of the membrane. It is well known that charge (Q) can be represented as a function of capacitance (C) and applied voltage (V) as:

$$Q_o = C_o \cdot V \tag{22}$$

when the capacitance definition (equation (5)) is substituted into equation (22), the charge as a function of applied bias and gap can be obtained as:

$$Q_o = \frac{\varepsilon \cdot A}{g_o} \cdot V \tag{23}$$

One can substitute equation (23) into equation (21) to obtain the electromechanical coupling coefficient as a function of applied voltage (V) and initial gap (g_o) as:

$$k_c^{\,2} = \frac{\varepsilon \cdot A \cdot V_{DC}^{\,2}}{k \cdot g_o^{\,3}} \tag{24}$$

Similar to the transformer ratio (n), the operation point should be moved close to collapse and the initial gap thickness should be minimized to increase the electromechanical coupling coefficient. For a parallel plate capacitor, the applied voltage can be represented as a function of the membrane deflection as:

$$V_{DC}^{\,2} = \frac{2 \cdot k}{\varepsilon \cdot A} \cdot g^2 \cdot (g_o - g) \tag{25}$$

where g is the gap height with applied voltage. When the applied voltage expression (equation(25)) is substituted into equation (24), after some manipulation, the electromechanical coupling expression simplifies to:

$$k_c^{\,2} = \frac{2 \cdot (g_o - g)}{g} \tag{26}$$

Note that the electromechanical coupling coefficient (k_c^2) expression is only dependent on the gap with the applied bias. The initial gap thickness does not change the electromechanical coupling coefficient (k_c^2) for a normalized DC bias; however, with

higher initial gap thickness, the required bias is increased. At zero bias, the electromechanical coupling coefficient (k_c^2) is zero, regardless of the initial gap thickness, and the electromechanical coupling coefficient (k_c^2) goes to 1 at collapse. As a result, for a parallel plate capacitor, the electromechanical coupling coefficient (k_c^2) versus normalized voltage curve is independent of initial gap and membrane thickness (Figure 13).

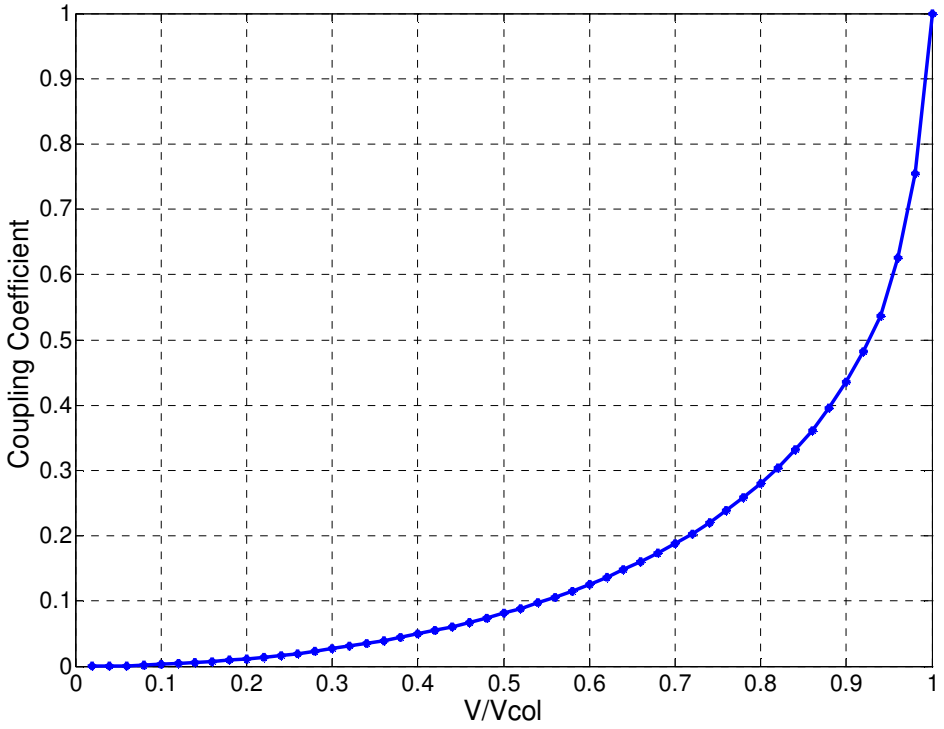

Figure 13 Analytical coupling coefficient as a function of normalized applied voltage for a parallel plate capacitor

We observe from Figure 13 that the electromechanical coupling coefficient (k_c^2) has a strong non-linear dependence on how far the operation point is from collapse. For instance, at 40% of the collapse, the electromechanical coupling coefficient (k_c^2) is 0.05 while at 80% of the collapse, the electromechanical coupling coefficient (k_c^2) is increased

more than 5 times to 0.28. Therefore, it is important to operate the CMUT at or close to collapse for maximum efficiency.

It is interesting to observe the relation between the electromechanical coupling coefficient (k_c^2) and the transformer ratio (n). When the expression for the electromechanical coupling coefficient (k_c^2) (equation (24)) is divided by the transformer ratio expression (n) (equation (16)) for a CMUT with no isolation layer, the following expression is obtained:

$$\frac{k_c^{\,2}}{n} = \frac{V}{k.g} = \frac{E}{k} \qquad \textbf{(27)}$$

where E is the electric field and k is the stiffness of the membrane.

2.2 Dual-Electrode CMUT Concept

CMUTs have so far been fabricated with a single top electrode as illustrated in Figure 14 (a) whose size and location can be optimized for coupling efficiency. However, the flexibility of microfabrication processes used for making CMUTs offer a much larger design space that can be explored to realize transducers with improved performance and functionality. An example of such an approach is based on using three electrodes in a rectangular CMUT membrane as shown in Figure 14 (b). Two side electrodes are connected in series to form transmit/membrane shape electrode while the center electrode is reserved for receive mode. Having extra side electrodes in the design has several advantages. Using the side electrodes to actuate the dual-electrode CMUT membrane, the stable range of static motion of the membrane can be increased by making use of the effect known as “leveraged bending” [59]. As depicted schematically in Figure 14 (c),

leveraged bending has been shown to increase the stable travel range of electrostatically actuated MEMS devices to nearly the full gap as opposed to the typical displacement of one third of the gap for a conventional CMUT membrane structure. By increasing the range of motion of the CMUT membrane, the volumetric displacement can be increased resulting in increased maximum transmit pressure. This comes at the cost of higher applied AC voltage, but in this configuration, the maximum available displacement -full gap operation- is achieved without collapsing the membrane providing better control of the pressure output.

Since the DC bias of the electrodes can be controlled independently, during receive operation, the membrane shape can be adjusted by the side electrodes so that center receive electrode can be brought closer to the bottom electrode as in Figure 14 (c). Note that in this case, there are two advantages as compared to conventional CMUT operation. First, the biased gap thickness can be reduced by more than two thirds of the initial gap increasing both the active capacitance and the capacitance change for a given displacement. In addition, with a smaller gap thickness under the center electrode, the DC bias on the center electrode required to collapse the membrane is significantly reduced. As shown in this thesis, both analytically and experimentally, this combination results in an improved receive sensitivity with reduced DC bias requirement for the center receive electrode. Therefore, the dual-electrode CMUT has an effectively larger gap as compared to a conventional CMUT during transmit mode of operation, and it has an effectively smaller gap during receive mode. This is in contrast with a conventional CMUT with a large gap which only improves transmit pressure, or having separate transmit and receive transducers which reduces the active area. Real-time operation of dual-electrode CMUT

requires dynamic adjustment of the bias voltage for the side electrodes between transmit and receive cycles, but this can be an easier task with electrically isolated transmit and receive electrodes. In this thesis, dynamic biasing is also investigated, and the experimental results will be documented. The use of isolated electrodes can also result in simplified electronics and may eliminate the need for problematic transmit-receive switches. Consequently, it may be possible to decrease the dead-zone in ultrasonic images by decreasing the ringing in receive amplifiers.

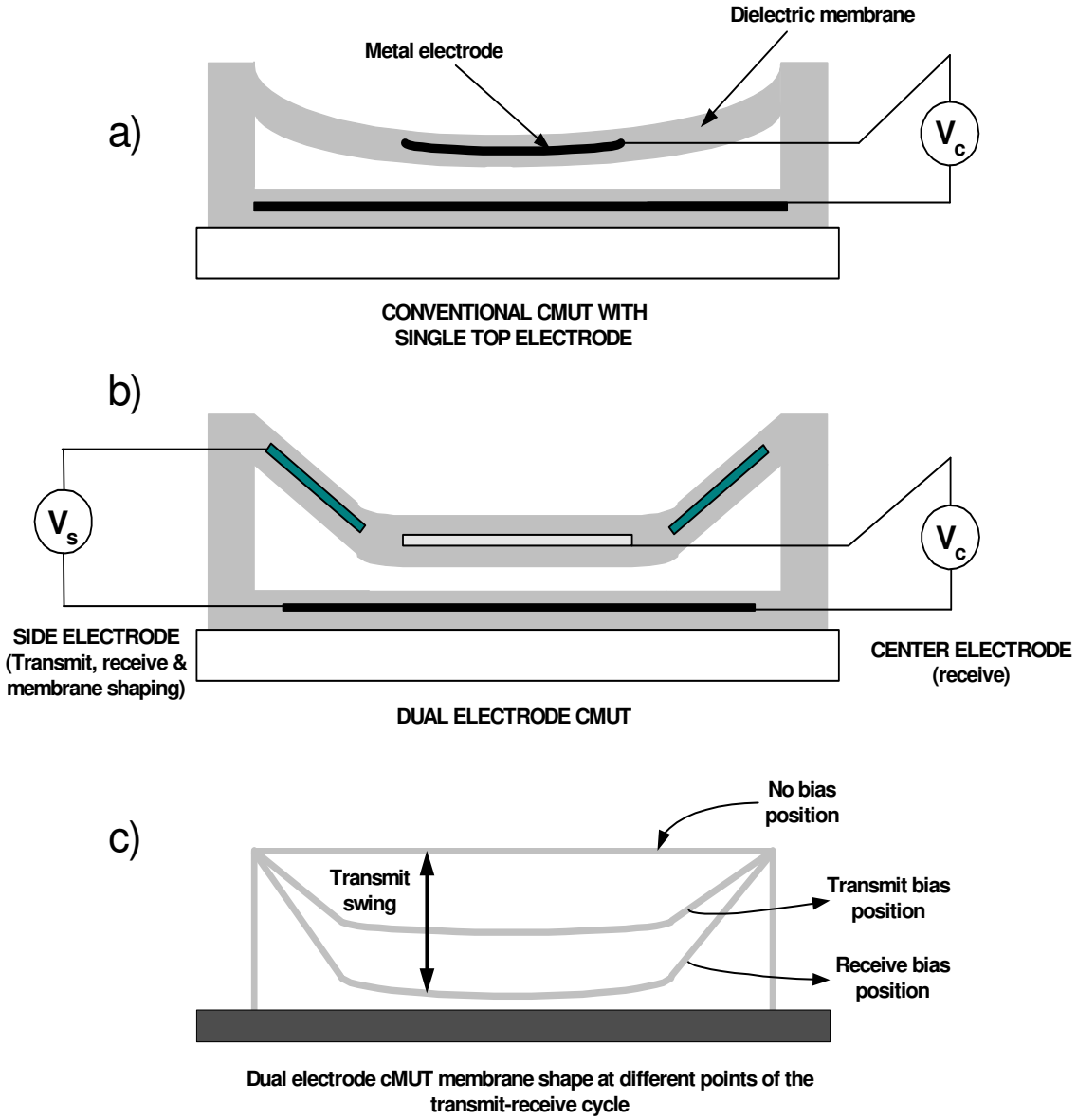

Figure 14 Schematics of a (a) Conventional CMUT with a single top electrode, (b) Dual-electrode CMUT with electrically isolated electrodes in dielectric membrane, (c) Dual-electrode CMUT bias positions during transmit and receive cycles.

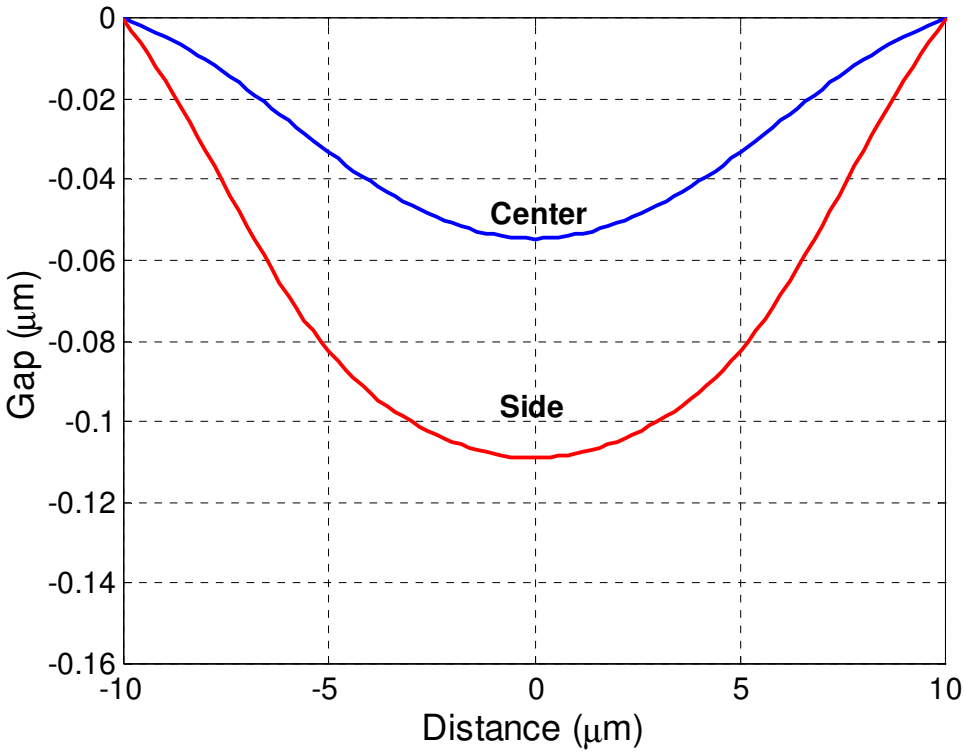

Figure 15 Deflection of the CMUT membrane just before the collapse when excited with center electrode and side electrodes.

Figure 15 shows the deflection of the CMUT membrane just before collapse as calculated using finite element analysis (FEA) for the case when only the center electrode is used to apply electrostatic pressure, as well as the case when the side electrodes are used. The silicon nitride membrane is 20µm wide 0.9µm thick and it is suspended over a 0.16µm gap on the rigid substrate. The dual-electrode CMUT has two 4µm wide electrodes on the sides and an 8µm center electrode in the middle embedded in the membrane. The details of the analysis are described in Chapter 3 of this thesis. As expected, the membrane collapses at approximately one third of the gap at 72V as is the case for the traditional single electrode CMUT, i.e. center electrode case. However, when side electrodes are used, the maximum membrane displacement before collapse at 208V

has increased to nearly two thirds of the gap (~1.97×). The actual improvement in output pressure is higher since, with leveraged bending, the deflection of the membrane is more uniform. As expected, the improvement in volume displacement as compared to center electrode actuation is calculated as 2.3× for this particular case. It has been shown that the side electrodes can be designed to achieve stable full gap actuation, so nearly 10dB improvement in maximum output pressure alone should be possible [59]. Note that these static calculations will be valid especially for the frequency range where the lowest vibration mode of the CMUT membrane is dominant. Furthermore, CMUTs with rectangular membranes have already been shown to be more efficient in terms of pressure output and active area as compared to CMUTs with circular membranes [60]. Consequently, dual-electrode CMUTs with rectangular membranes as described here can result in more improvement in maximum pressure output as compared to CMUTs with circular membranes, which are used for CMUT-piezoelectric array comparisons [48].

Since in dual-electrode CMUTs transmit and receive mode of operation can be optimized separately, one can use a different design criterion for maximum receive sensitivity. Although some equivalent circuit parameters also change with DC bias and initial gap, our simulations based on the linear equivalent circuit of Figure 11 show that the electromechanical transformer ratio can be used as a simple metric for relative performance improvement in receive mode, given that other mechanical and electrical circuit parameters are kept constant and reasonable values of parasitic capacitance are used. Moreover, this figure can be easily calculated from static coupled finite element analysis. The transformer ratio at the onset of collapse is derived in section 2.2 and given here as:

$$n_{col} = \sqrt{\frac{8 \cdot k \cdot \varepsilon_o \cdot A \cdot g_o^{\,3}}{27 \cdot (\frac{2 \cdot g_o}{3} + \frac{t_{nit}}{\varepsilon_r})^2}} \qquad \textbf{(28)}$$

One can observe from equation (28) that, for a given finite initial gap thickness and nitride isolation, the transformer ratio reaches a finite, maximum value at the collapse voltage. The important conclusion of this simple analysis is that, at or close to collapse voltage, the transformer ratio depends only on the initial gap, but not on the absolute value of the DC bias required for collapse. In other words, one can achieve high conversion efficiency in receive mode with low bias voltage as long as the gap between the CMUT electrodes is small enough. A significant feature of a dual-electrode CMUT structure is that by biasing the side electrodes during receive operation, a small gap between the center receive electrode and the ground electrode can be maintained and hence high sensitivity can be achieved with a low DC bias. Reduced DC bias requirement can also help in designing low voltage receive electronics using standard CMOS processes.

CHAPTER 3

FINITE ELEMENT MODELING OF DUAL-ELECTRODE CMUTS

3.1 Acoustic Model

To simulate transmit and receive characteristics of the dual-electrode CMUT structure and to predict the performance improvements by employing extra electrodes in the membrane design, the coupled field electrostatic simulation capability of the commercial FEA program, ANSYS v11.0 (ANSYS Inc., Canonsburg, PA) is used. The simulations make use of the multi-physics capabilities of ANSYS in which structural disturbances in the solid are coupled to the motion of the fluid, and vice-versa. The finite element model consists of four major components: the device to be modeled, the fluid, the fluid-structure interface, and the absorbing boundary as illustrated schematically in Figure 16 [61]. The fluid in the simulation is assumed to be linear and lossless. Vibrations of the solid are coupled to the fluid through the Fluid Structure Interface (FSI) region which forces the normal stress to be continuous across the interface. This results in two-way coupling from the solid to the fluid. Since a harmonic analysis is carried out to obtain acoustical response, an absorbing boundary condition is required to prevent waves from reflecting off of the model edge and generating an unrealistic standing wave field. This allows one to simulate an infinite fluid domain with a finite number of elements. In this chapter, first, the radiation impedance of a baffle piston is simulated and compared with well-known radiation impedance results. After validation of the developed model, possible improvements over the current design are explored. First, for the simulation of CMUTs, the material constants are determined by matching the measured collapse

voltage, resonance frequency, and capacitance of existing CMUTs. A 1-D model is used after verifying that the long rectangular CMUT membranes can be accurately modeled with this approach.

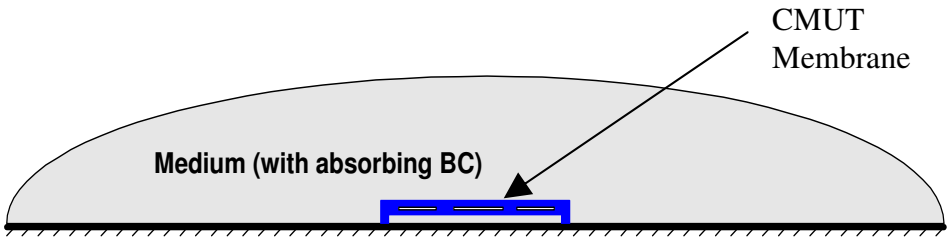

Figure 16 Schematic of a 1-D finite element model used in simulations

3.1.1 Model Verification

The radiation impedance of a piston in a rigid baffle has a well known solution that can be used to verify the Finite Element Modeling (FEM) results. In mechanics, the ratio of force amplitude to velocity amplitude is referred to as impedance. Although this definition has a pure mechanical meaning, it is also introduced to electric-circuit theory as a ratio of voltage amplitude to current amplitude. Note that voltage and current can be used as the electrical counterpart of force and velocity respectively. In acoustics, the radiation (acoustical) impedance is defined as the ratio of force amplitude to the velocity amplitude. The radiation impedance (Z) leads to a boundary condition describing a surface:

$$Z = \left(\frac{P}{v_{in}}\right)_s \tag{29}$$

In the above equation, Z is the radiation impedance, P is complex pressure amplitude, V_{in} is the complex velocity amplitude in the direction into the surface, and s represents the surface where the radiation impedance is evaluated. For a plane wave propagating along the n_i direction, the radiation impedance expression can be simplified to:

$$Z = \rho \cdot c \tag{30}$$

where ρ is the fluid density and c is the speed of sound in fluid. Note that the radiation impedance is a complex quantity as both the pressure and velocity are complex quantities.

To simulate the radiation impedance of a baffle piston, a uniform displacement is applied to the membrane of a CMUT. Uniform displacement makes the CMUT membrane move like a piston. The pressure on the membrane is obtained by the harmonic analysis of the ANSYS. With the known complex displacement and pressure, Matlab 7.0 (Natick, MA) is used as a tool to find the real and imaginary radiation impedance as a function of frequency. More specifically, with the known displacement, one can convert the displacement field to the velocity field by:

$$V = j \cdot 2 \cdot \pi \cdot \omega \cdot D \tag{31}$$

where D is the complex displacement and ω is the frequency. Then, the radiation impedance defined by equation (29) is calculated with the known pressure and velocity. This analysis is repeated for the membrane size of 50μm and 120μm to observe the effect of membrane size. The simulated radiation impedances of 50μm and 120μm membrane are shown in Figure 17 (a) and (b) respectively.

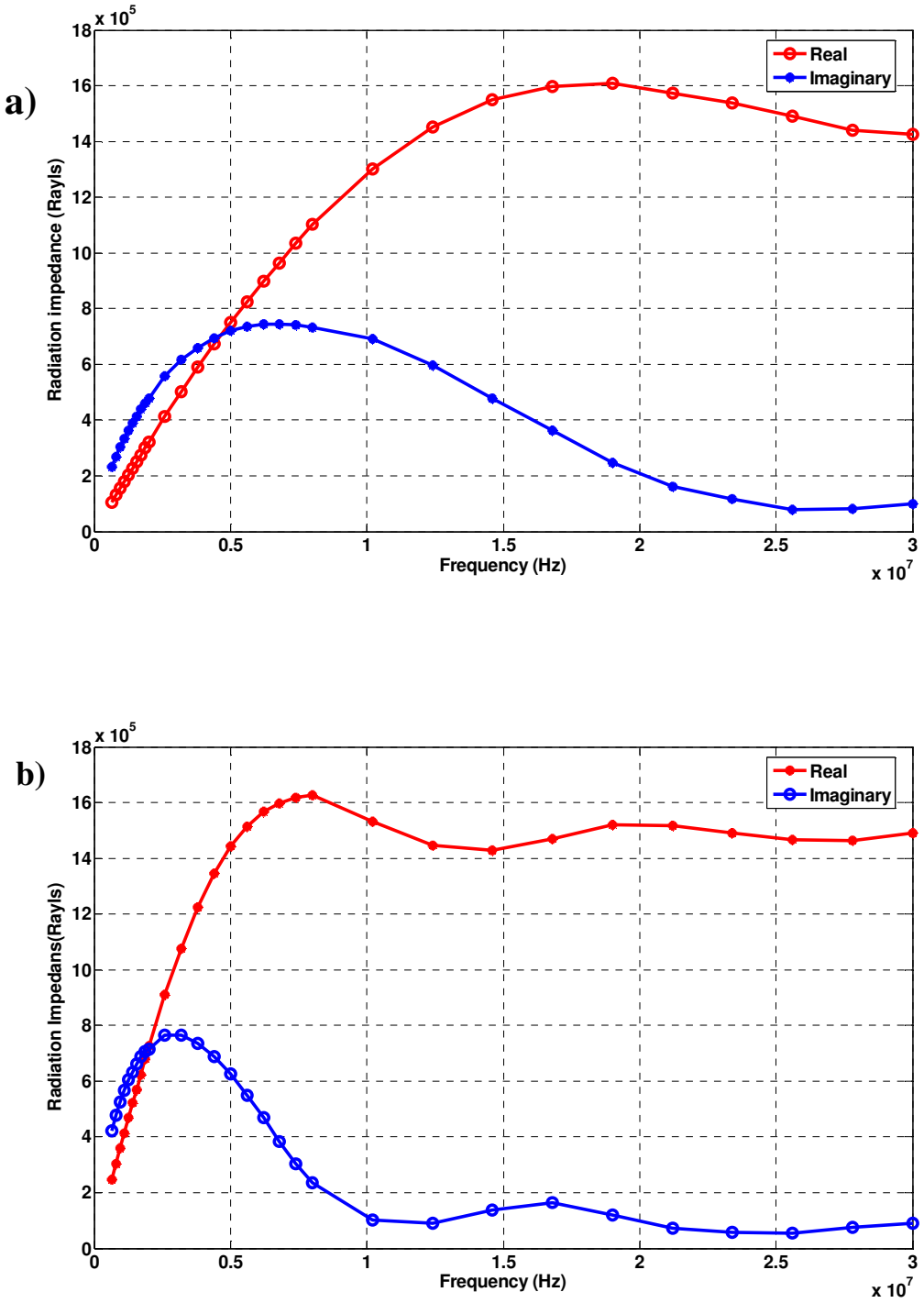

Figure 17 Simulated real and imaginary radiation impedance of a a) 50µm baffled piston b) 120µm baffled piston

One can observe from Figure 17 that both 50µm and 120µm pistons follow a common trend similar to the closed form radiation impedance solution of a circular baffled piston illustrated elsewhere [62, 63]. It is important to note that both real and imaginary parts of the radiation impedance increase up to a certain frequency then the imaginary part decays approaching zero while the real part of both Figure 17 (a) and (b) converge to 1.5MRayls. According to far field approximation, the radiation impedance value should converge to the radiation impedance of the medium which is given in equation (30). In this simulation, the medium is assumed to be water with properties: ρ=1000 kg/m^3 and c=1500 m/s. Hence the theoretical far field radiation impedance should be 1.5Mrayls which is the same value obtained from the simulation. Moreover, one can observe that the larger (120µm) membrane reaches its far field faster than the smaller (50µm) membrane. This is an expected result as the larger membrane generates waves closer to the plane wave than the smaller membrane; as a result. the far field approximation is applicable at lower frequency for wider membranes. To sum up, the results illustrated in Figure 17 verify the accuracy of developed simulation models and its ability to capture the radiation impedance dependence on the membrane parameters.

3.2 Coupled Field Electrostatic Model

3.2.1 Collapse Voltage and Frequency Response Simulations

Before quantifying performance improvements achievable with dual-electrode CMUTs, finite element simulations should be developed to extract the collapse voltages for side and center electrodes and immersion frequency response to compare the conventional and dual-electrode CMUTs. To simulate a CMUT membrane, load

conditions should be changed as compared to the baffled piston case. In the baffled piston case, uniform displacement is applied to the membrane to simulate piston behavior. However, pressure should be used as the input to simulate bending and edge deformation of a CMUT membrane. To find the collapse voltage, the displacement as a function of applied voltage is simulated. The maximum bias that results in a non-gap height displacement is recorded as the collapse voltage. As a reference, the displacement as a function of applied bias for a CMUT with physical dimensions listed in Table 1 is shown in Figure 18. One can observe from this figure that the displacement of the membrane increases as a non-linear function of the bias voltage. Operation close to collapse results in a higher sensitivity as a small voltage change creates a relatively large membrane displacement. In addition, for bias values exceeding collapse voltage, simulations show that maximum displacement of the membrane is the gap height itself. Note that the analysis developed in this study does not have contact analysis capability.

The accuracy of the FEA model is also verified by comparing theoretical and calculated collapse voltage values for a parallel plate membrane. The theoretical collapse voltage value is calculated by using equation (4). For various membrane sizes, the collapse voltage results from FEA agree with theoretical values within 10%, while less than 5% error is typical for most of the cases. Therefore, FEA calculations can be used to predict important parameters for dual-electrode CMUTs such as the transformer ratio (n) and electromechanical coupling coefficient (k_c^2).

Table 1 Physical parameters of a non-optimal CMUT membrane used in simulations

Membrane Width/Thickness	20µm/1µm
Gap/isolation thickness	0.16µm/0.6µm
Center/side electrode sizes	8µm/4µm

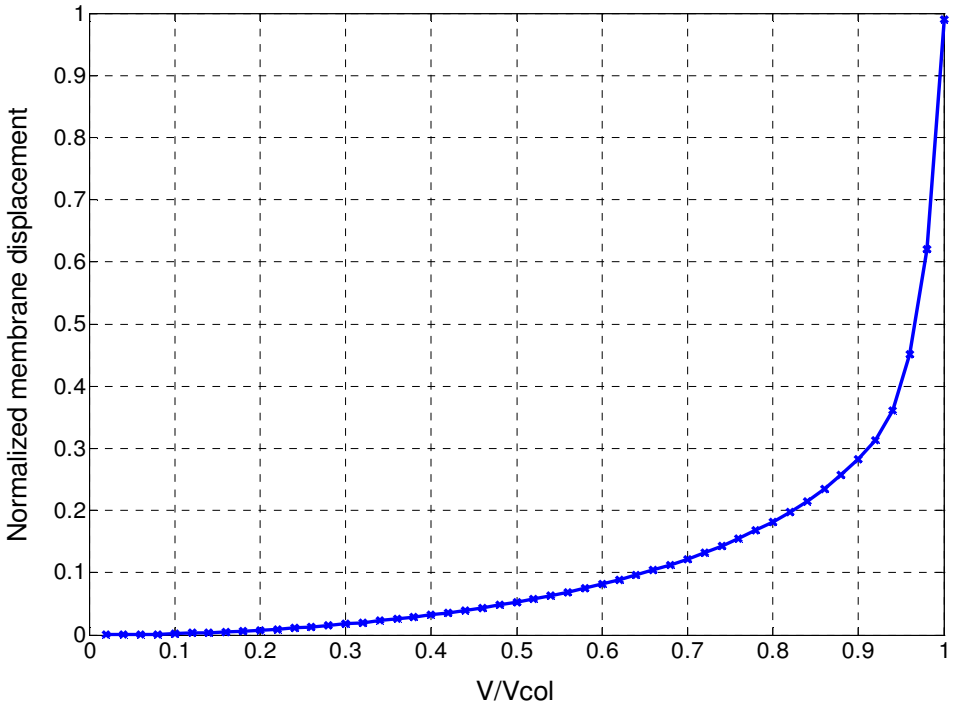

Figure 18 Normalized displacement for a CMUT membrane with dimensions given in Table 1 as a function of applied bias

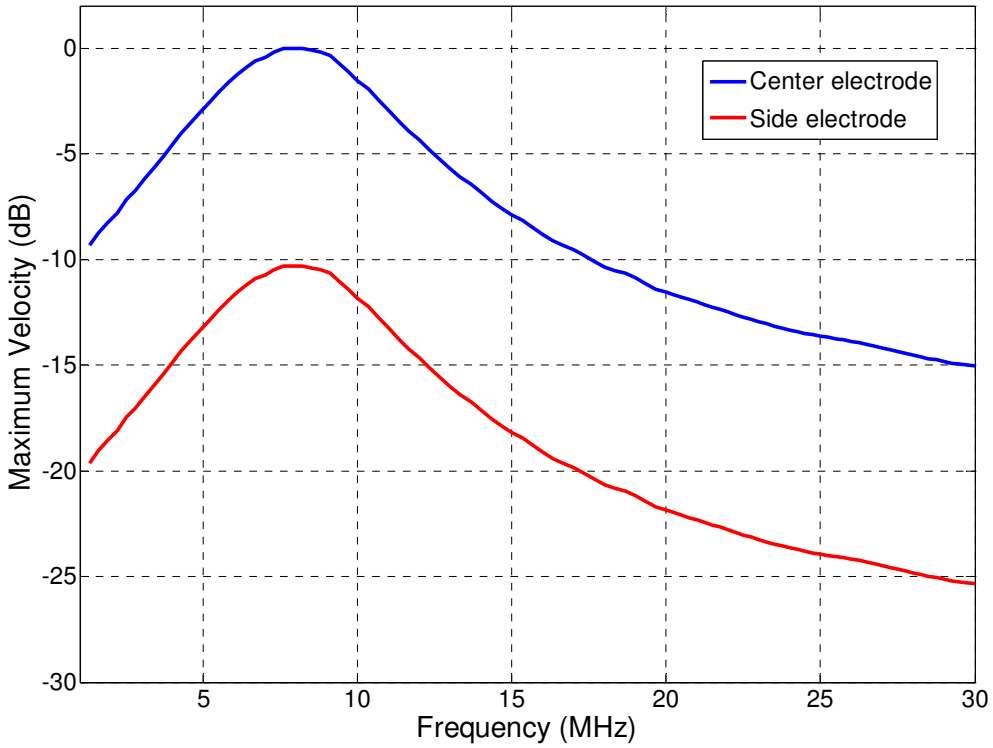

Figure 19 Simulated average membrane velocity obtained by harmonic acoustic FEA when harmonic pressure is applied to the center and side electrodes.

The frequency response of the same dual-electrode CMUT membrane when excited with same pressure for side and center electrodes is illustrated in Figure 19**.** This figure indicates that the first resonant mode of the structural membrane is around 8MHz both for side and center electrode excitation. Moreover, the frequency response of both side and center excitation looks similar. This is an important result for performance improvement comparison of conventional and dual-electrode CMUTs. It will be assumed that the frequency response is not altered by employing extra side electrodes in the CMUT membrane design.

3.2.2 Transmit and Receive Mode Performance Evaluation

To model transmit displacement improvement for maximum pressure generation with dual-electrode CMUTs, we calculated the membrane shape just before collapse or alternatively the pressure value is directly obtained from the solid-fluid interface (FSI) node during the acoustic analysis. One can extract transmit efficiency of side and center excitation from Figure 19 as well. It can be observed from this figure that the transmit efficiency of the side electrode is nearly 10dB lower in terms of Pa/V over the whole bandwidth. This is expected as the CMUT membrane deflects less with the same electrostatic force applied to the side electrodes located at the edges as compared to the center electrode. Note that the FEA analysis assumed that the dual-electrode CMUT membranes were over a perfectly rigid substrate. Furthermore, since the same AC electrostatic force is applied in this linear FEA, the center electrode experiences larger forces since it is driven closer to its collapse voltage.

To predict the improvement in receive performance and compare the results with the ideal parallel plate model, one needs to evaluate C_0 and E values using FEA results to obtain the transformer ratio, (n) as illustrated in equation (16). For this purpose, we first compared the capacitance values obtained by the parallel plate model and FEA results for the same CMUT. The results are within 7% in the whole DC bias range from zero to collapse voltage, indicating that CMUT membrane behaves very similar to a parallel plate capacitor for the purpose of C_0 and E calculations. This shows that the fringing capacitance and the curvature of the electrodes on the membrane are not significant. Since only the center electrode is used as a receiver for this study, the values of capacitance and electric field under this electrode are considered while side electrodes are

used to deform the CMUT membrane controlling the position of the center electrode. Note that each dual-electrode CMUT has two collapse voltages corresponding to the side and center electrodes.

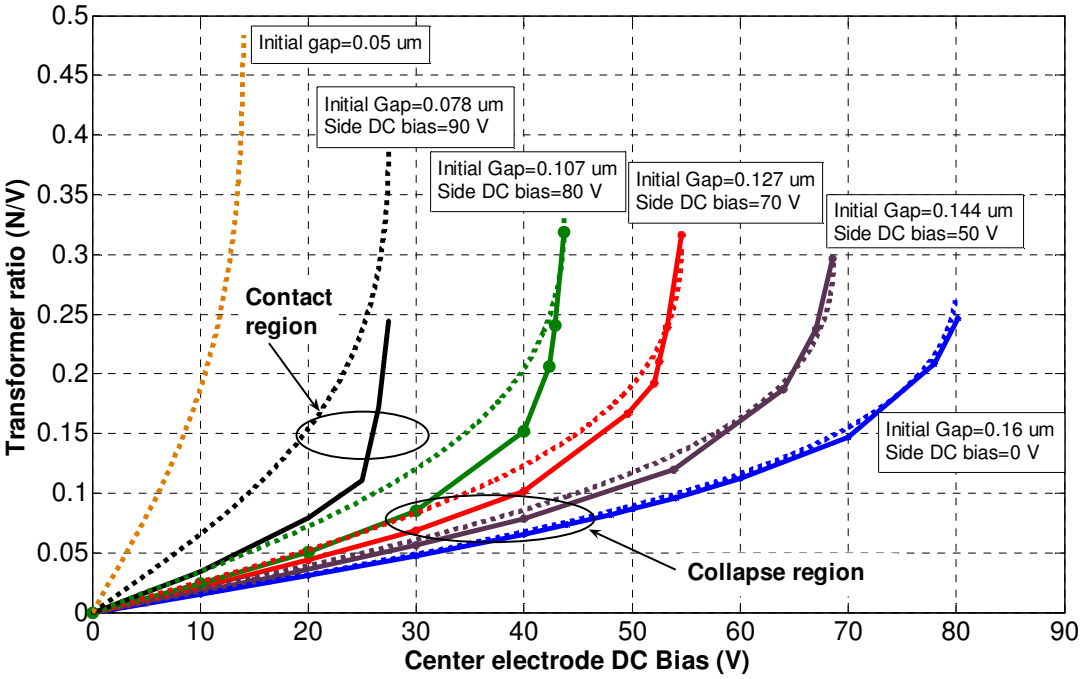

Figure 20 Calculated transformer ratio as a function of initial gap thickness and applied voltage for the parallel plate CMUT model (dotted lines). Simulated transformer ratio for the center electrode of the CMUT for various side electrode bias values (solid lines)

To illustrate the improvement in receiver sensitivity for the ideal parallel plate case and realistic CMUT design with equivalent mechanical properties (spring constant k_s= 1315 N/m) we refer to Figure 20. Each dotted line in Figure 20 shows the variation of transformer ratio with bias voltage applied to the top electrode for an ideal parallel plate CMUT with a different initial gap thickness. The bias voltage is varied from zero to 95% of the collapse voltage for the corresponding CMUT. Note that with an initial gap of 0.16μm, the maximum n value that can be achieved is 0.26N/V with V_{DC} = 80V. In

comparison, with an initial gap of 0.05μm, *n* can be as high as 0.48N/V, an improvement of 5.3dB, with only 13.5V required bias. The improvement in transformer ratio becomes significant especially when the membrane approaches to collapse, where theoretically this figure can further increase by reducing the gap height. Since membrane displacements are expected to be small in receive mode, small gap thickness on the order of 50nm are feasible. One would think that this limits the output pressure, but the dual-electrode structure with time varying bias voltage effectively decouples the transmit and receive optimization problems.

In the same figure, the FEA results for a dual-electrode CMUT are also shown. For a fair comparison, the mechanical characteristics of the membrane, i.e. the spring constant is same as the parallel plate CMUT. When no bias is applied to the side electrodes, the variation of transformer ratio with DC bias applied to the center electrode follows the parallel-plate CMUT, reaching 0.25N/V at 80V (95% of collapse). The advantage of the dual-electrode structure in receive mode becomes apparent when non-zero DC bias is applied to the side electrodes. For example, consider the case where 70V is applied to the side electrodes (middle solid red curve in Figure 20). When the center electrode bias is increased from 0V the transformer ratio increases more rapidly reaching 0.32N/V at a bias of 54V, which corresponds to 95% of the collapse voltage for the center electrode. Therefore, a higher transformer ratio is achieved with less DC bias applied to either electrode. Clearly the DC bias applied to the side electrodes reduces the effective gap thickness for the center electrode improving the receive performance. However, in contrast to the ideal parallel plate CMUT, the maximum increase in transformer ratio is limited. When the bias voltage applied to the side electrodes is

increased over a certain value, the bottom of the silicon nitride membrane underneath the center electrode makes contact with the bottom surface. Since this contact occurs well below the collapse voltage for the given initial gap, determined by the side electrode bias, the transformer ratio cannot be increased beyond a certain value. As shown in the leftmost black solid curve, when 90V bias applied to the side electrodes membrane contact occurs at a center electrode DC bias of 27V, and the maximum transformer ratio is below 0.25N/V. Note that at this point the side electrodes, which have a collapse voltage of 115V, are not collapsed. Also note that receive improvements with a dual-electrode CMUT is limited by the existence of a contact region. By using thin isolation and gap thickness, the bias voltage for contact region initiation can be increased, causing higher receive mode gains attainable. To test this hypothesis, the 15µm wide center and 10µm wide side electrodes are placed over the last 250nm of the 3.5µm thick, 48µm wide membrane while reducing the gap to 0.12µm (Table 2). The optimization study is explained in detail in chapter 4. The variation of the transformer ratio simulated for the center electrode as a function of side bias values are illustrated in Figure 21.

Table 2 Physical parameters of an optimized CMUT membrane used in simulations

Membrane Width/Thickness	48µm/3.5µm
Gap/isolation thickness	0.12µm/0.25µm
Center/side electrode sizes	15µm/10µm

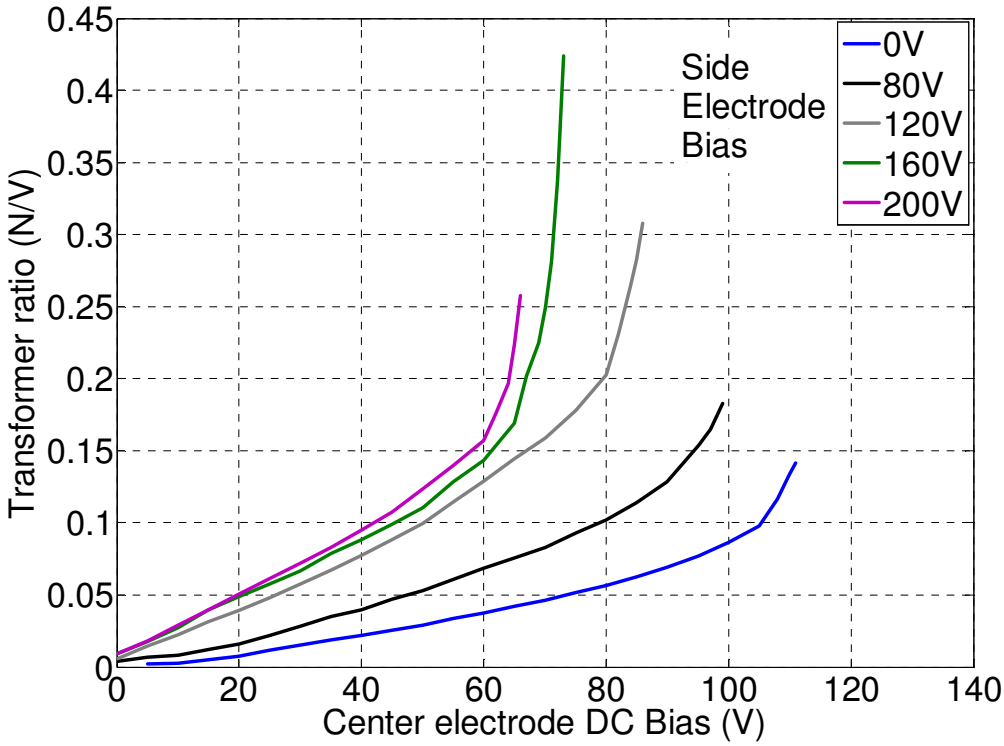

Figure 21 Transformer ratio variation calculated by FEA for the center electrode of dual-electrode CMUT for various side electrode bias values

We observe from Figure 21 that the electromechanical transformer ratio is increased from 0.14 for the conventional CMUT to 0.42 for optimized dual electrode structure. This corresponds to receive mode improvement of 10dB with dual electrode structure as compared to conventional CMUT. Note that the performance improvements are in addition to transmit performance improvement achievable with this structure. Contact and collapse regimes are present in these membrane parameters as well, but initiation of contact region occurs after higher performance improvement. As a result, thinning down the isolation layer and having a smaller gap in the design significantly improves receive performance i.e. transformer ratio of the transducer. Also note that this graph is by no means a limit to the performance improvements achievable with dual-electrode CMUTs, it rather serves the purpose of illustrating optimization possibility.

3.2.3 Electromechanical Coupling Coefficient Simulation

As introduced and discussed in detail in section 2.3, the electromechanical coupling coefficient (k_c^2) can also be used as a figure of merit for the receive mode of operation. Calculation of k_c^2 is based on the energy definition:

$$k^2 = \frac{E_{mech}}{E_{mech} + E_{elec}} \tag{32}$$

In this thesis, two methods of calculating the electromechanical coupling coefficient (k_c^2) are investigated. The first method is simulating the mechanical energy (E_{mech}) and electrical energy (E_{elec}) values directly. As coupled field analysis between mechanical and electrical domain is used in harmonic analysis, the electrical and mechanical energies values can be extracted at any bias value. As a second alternative, electromechanical coupling coefficient (k_c^2) can be calculated using the capacitance definition as shown in equation (33) [28, 64]. This capacitance definition is adapted from the coupling coefficient definition for piezoelectric transducers based on the strain definition [65].

$$k^2 = 1 - \frac{C^s}{C^T} \tag{33}$$

In this equation, the C^S is the fixed capacitance and C^T is the free capacitance which is defined as the slope of the charge-voltage curve. The expressions for fixed and free capacitances are shown in equations (34) and (35) respectively.

$$C^s = \frac{Q(x)}{V}\Big|_{x_{DC},V_{DC}} \tag{34}$$

and

$$C^T = \frac{dQ(x)}{dV}\Big|_{x_{DC},V_{DC}} \tag{35}$$

The capacitance based alternative involves calculating derivatives to obtain the free capacitance (C^T). To calculate the derivative, the operation bias (V) is increased slightly from its value (to $V+\Delta V$) and the differential is calculated by subtracting the respective charge (Q) and bias voltage (V) values. The electromechanical coupling coefficient (k_c^2) as a function of normalized voltage step (ΔV) for derivative calculation is illustrated in Figure 22. It can be observed from this figure that there is significant round-off error for a small voltage step (ΔV). Actually, when the voltage step (ΔV) approaches zero; the electromechanical coupling coefficient (k_c^2) reaches unity regardless of the applied bias. On the other hand smaller voltage step (ΔV) results in more accurate results for coupling coefficient calculation. We observe from Figure 22 that the voltage step of 0.8% of the applied bias produces a ± 3% error in the electromechanical coupling coefficient (k_c^2). The voltage step (ΔV) of 0.8% is used in this study.

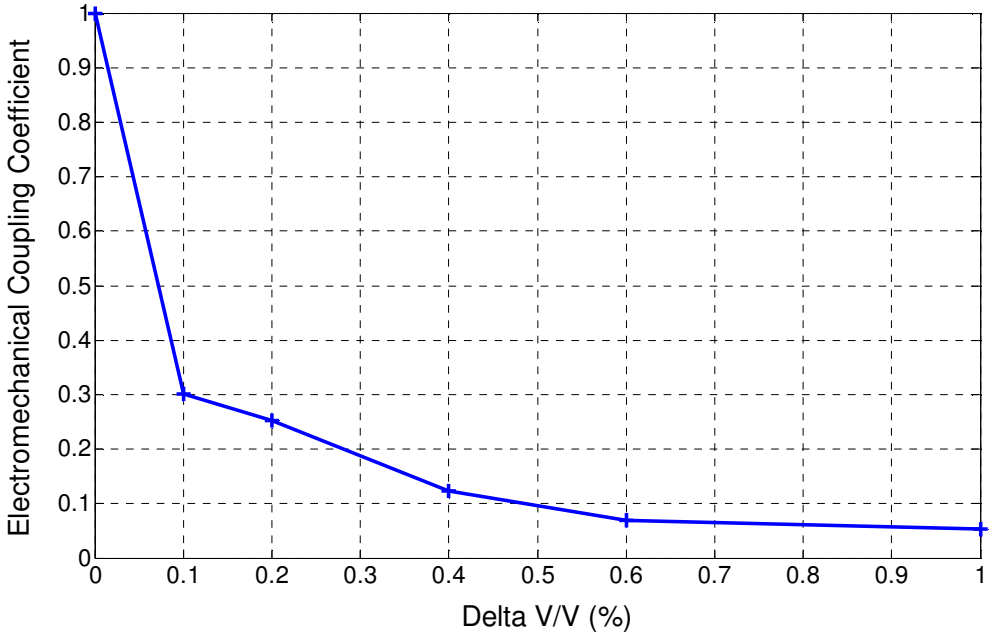

Figure 22 Electromechanical coupling coefficient versus normalized voltage step (ΔV) used in the free capacitance (C^T) calculation

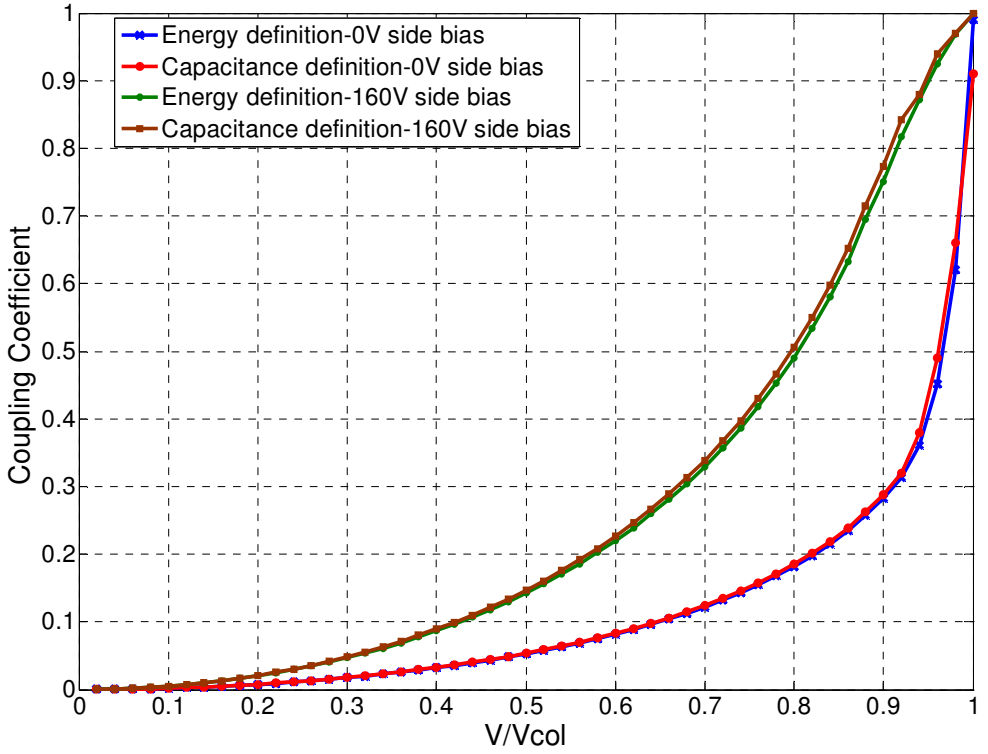

Figure 23 Electromechanical coupling coefficient as a function of normalized bias by using the capacitance and energy definition for 0 and 160V side electrode bias values.

Comparison of simulated coupling coefficient for 0 and 160V side electrode bias values using direct energy method and capacitance method is illustrated in Figure 23. Both methods give very similar results and can be used to assess the coupling coefficient effectively. Note also from Figure 23 that the coupling coefficient approaches one at the collapse point regardless of the membrane parameters as electrical energy stored in the membrane is orders of magnitude lower than the stored mechanical energy. In the other extreme, at 0 bias condition, as the membrane is not deflected, the mechanical energy is much smaller than the stored electrical energy; hence, the coupling coefficient approaches 0.

Variation of the coupling coefficient for the dual-electrode CMUT with center electrode bias voltage normalized to center electrode collapse voltage is illustrated in Figure 24. The optimized membrane parameters used in the simulations are shown in Table 2. One can observe from Figure 24 that regardless of side electrode bias (in the collapse regime) that the coupling coefficient approaches 1 at collapse. However when 90% of the collapse voltage is considered, the coupling coefficient is increased from 0.24 to 0.71 when the optimized dual electrode structure is employed in the design. In the contact regime, the electromechanical coupling coefficient does not reach “1” as the contact regime is reached before the onset of the collapse phenomenon.

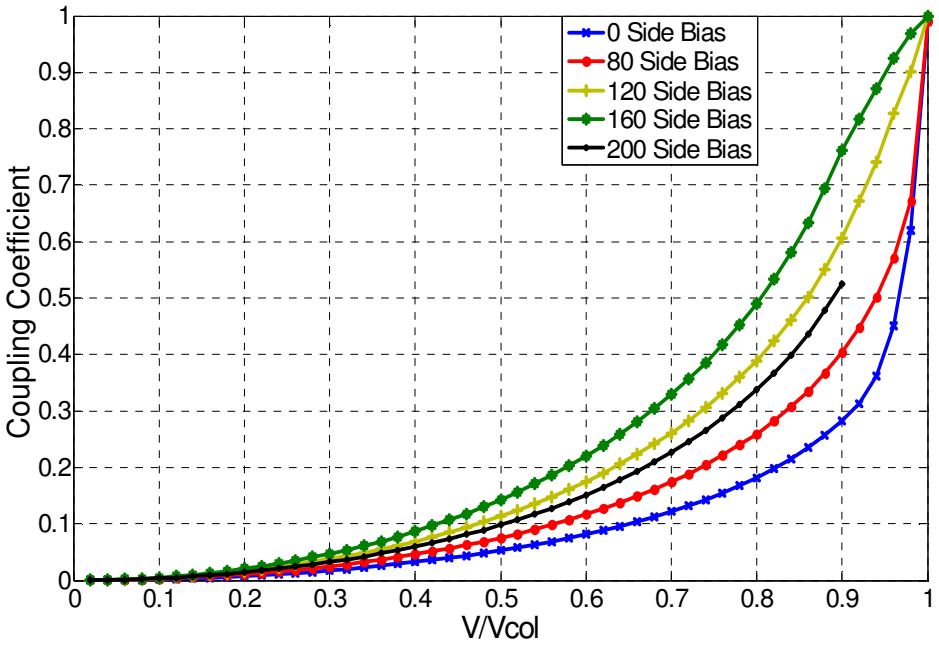

Figure 24 The coupling coefficient variation calculated by FEA for normalized bias on the center electrode of the dual-electrode CMUT for various side electrode bias values

Although Figure 24 illustrates the performance increase by dual-electrode implementation, the collapse voltage values for the center electrode can not be extracted as a function of side electrode bias. To obtain this information, the coupling coefficient for the dual-electrode CMUT with center electrode bias for various side electrode bias values are illustrated in Figure 25. One can observe that the collapse voltage, as a function of side electrode bias, is similar to the one that is observed from Figure 21. Moreover, in both Figure 24 and Figure 25, the collapse and contact regimes are observed, and the onset of contact regime matches the calculations obtained from the transformer ratio.

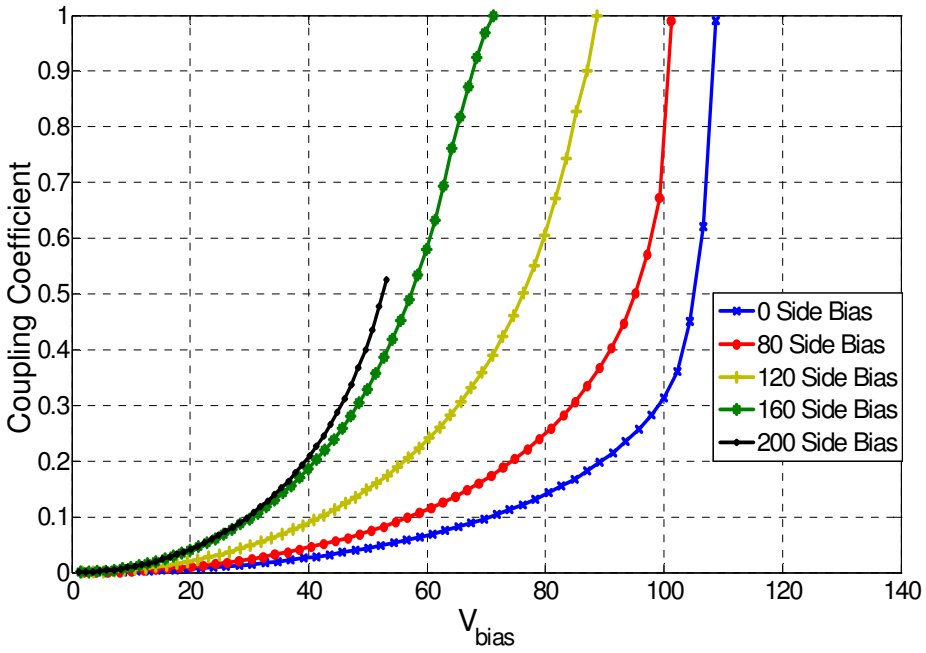

Figure 25 The coupling coefficient variation calculated by FEA for applied bias on the center electrode of the dual-electrode CMUT for various side electrode bias values

3.2.4 Electrical Isolation Simulation

We also modeled the internal cross-talk capacitance between the electrodes of the dual-electrode CMUT, which is important for transmit and receive electronics isolation. To evaluate the internal cross talk between side and center electrodes, ANSYS 11.0 has been used. The CMATRIX macro is employed to find the active capacitance of receive center electrode ($C_{receive}$) and cross capacitance between transmit and receive electrodes (C_{cross}) as illustrated in Figure 26 [66]. The medium of interest in contact with the membrane is also modeled. Before solving the capacitance values, deflection of the membrane with the given optimum side and center electrode bias values is simulated and the deflection profile is used as an initial condition to the capacitance finding macro. We found that for a 20μm wide, 0.9μm thick silicon nitride dual-electrode CMUT membrane

operating in air with a 2μm gap between the center and side electrodes, C_{cross}, is 37 times less than $C_{receive}$ corresponding to 31dB of isolation [67]. This indicates that the electrodes have good AC isolation in addition to DC isolation between the multiple electrodes. This result is for air operation only and different media may alter the isolation between the side and center electrodes significantly. The effect of medium and membrane parameters on the electrical isolation will be investigated in Chapter 4 of this thesis.

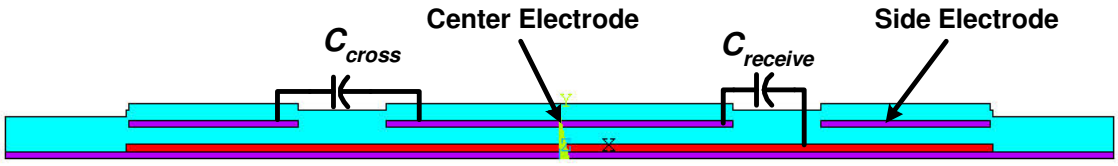

Figure 26 Scaled rendering of a dual-electrode CMUT and relevant capacitance values used for electrical isolation analysis

3.3 Coupled Field Dynamic Model

In the static simulations, the dual-electrode CMUT is modeled in a quasi-static state in which the membrane is only capable of responding to an applied input without time delay. As a result, dynamic effects are not taken into consideration. Moreover, applied AC bias is limited as the simulation codes are developed based on the small-signal model. To capture the dynamic response of CMUT membranes in immersion, transient simulations are developed. The transient analysis can be used to observe the effect of any combination of AC and DC combinations applied to the membrane. Hence more realistic results can be obtained by using transient analysis. By using transient analysis, one can determine the collapse voltage for both side and center electrodes, dynamic displacement profile and the frequency response of the CMUT membrane, and

the net output pressure at the membrane fluid interface. In the transient analysis, ANSYS trans126 transducer element is employed to model the electromechanical coupling [61]. Trans126 has several advantages over the Essolve macro that we used in the static simulations. The capacitance or alternatively displacement as a function of applied voltage relation is internally calculated within the Emtgen macro which handles the trans126 elements [66]. Moreover, spring softening, collapse phenomena are already handled by the same macro, therefore it is a much faster implementation than the Essolve macro. In addition, the fluid in contact with the membrane is also modeled to observe the effect of fluid damping in the dynamic response of the membrane. The transient code developed can be used to investigate the larger design space that dual-electrode CMUTs offer. Note that as a trade-off, transient analysis is very operationally intensive as compared to static analysis because of solving the problem at each time step.

Figure 27 illustrates the calculated membrane displacement as a function of time for the optimized CMUT geometry shown in Table 2. At initial time (t=0), DC bias which is equal to half the collapse voltage for each electrode (collapse voltage: 120V for center electrode; 240V for side electrodes) is applied to the respective electrodes. After the membrane reaches its steady state at time 600ns, a 20ns uni-polar pulse with amplitude of half the collapse voltage is applied to the respective electrodes (60V for center electrode, 120V for side electrodes). We observe from the displacement plot of Figure 27 that the single electrode configuration can only reach 1/3 of the gap height (40nm). On the other hand, the dual-electrode CMUT increases the movable range to 80nm which corresponds to 2/3 of the gap. These displacement results obtained by transient analysis match the displacement obtained by the static simulation case. Note

also that the collapse voltage obtained by transient analysis matches the values obtained by the static analysis. These results show that using trans126 elements and employing the transient capability of ANSYS does not alter the results as compared to static analysis simulation. Figure 28 illustrates the operation mode when there is no bias applied to the CMUT membrane and at initial time (time=0), a 20ns, uni-polar pulse with maximum pulse amplitude that does not collapse the membrane is applied. The maximum pulse amplitude that does not cause collapse is 210V for the center electrode and 380V for the side electrodes. It is interesting to note that these voltages are above the static collapse voltage for the respective electrodes. For center electrode excitation, the displacement is increased as well from 1/3 of the gap to 2/5 (40%) of the gap. This phenomenon has been observed before by others [31, 54]. More interestingly, the motion range for the dual-electrode CMUT membrane is also increased from 2/3 of the gap (66%) to 4/5 of the gap (80%).

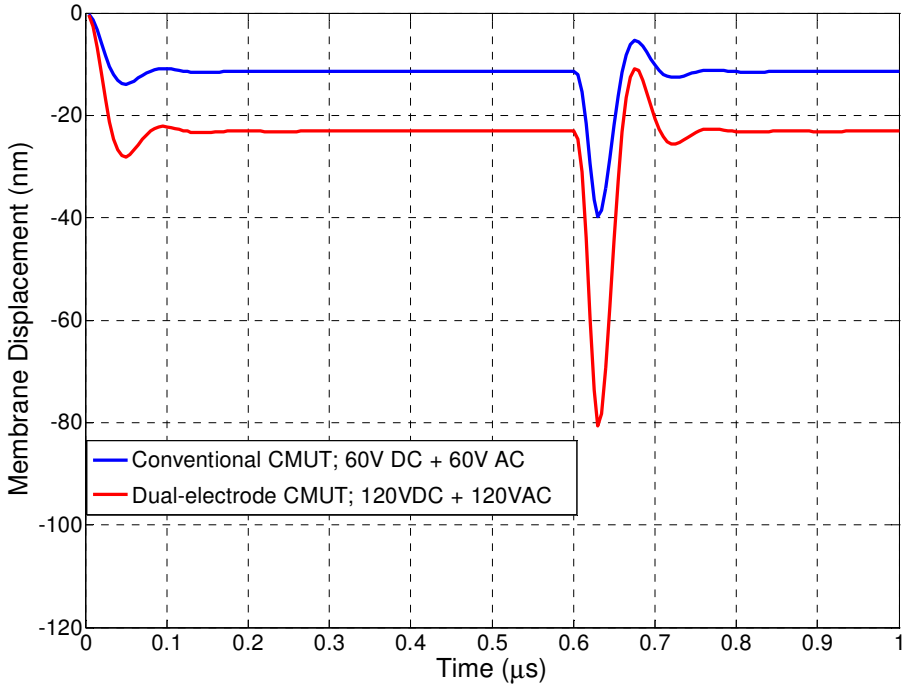

Figure 27 Simulated transient membrane displacement as a function of time with AC pulse applied when DC bias is present

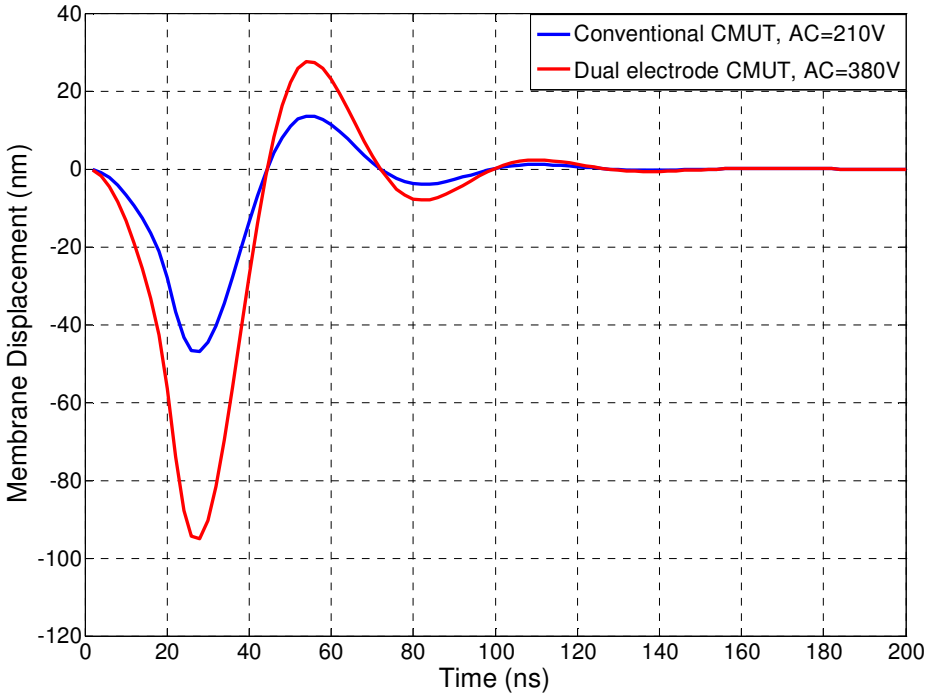

Figure 28 Simulated transient membrane displacement as a function of time with only AC pulse applied (without DC bias)

3.4 Discussion

In this chapter, finite element simulations that are used to calculate the collapse voltage, frequency response, transmit and receive mode performance evaluations are explained in detail. It also needs to be noted that there are several assumptions in the developed finite element simulations. For instance, the fluid is assumed linear and lossless. To minimize the effect of this assumption on the results, the pressure output is simulated on the membrane-fluid interface. Furthermore, the residual stress in the membrane is not included in the simulations, because the membrane material (silicon nitride) has very low intrinsic residual stress. Moreover, all of the analyses developed in this chapter are 1-Dimensional analysis. However, in reality, the rectangular membrane vibrations do not exactly follow the simulated 1-Dimensional vibration modes. Figure 29 illustrates the vibration modes obtained by 3-Dimensional simulations in air. 3-Dimensional analysis in immersion could not be handled due to the node limitations of the academic version of ANSYS. It is important to note that the 1^{st} mode operational frequency obtained from 3-Dimensional simulation is 15.4 MHz, while 1-Dimensional simulations indicate the same (15.4MHz) 1^{st} mode operational frequency. This verifies the accuracy of using 1-Dimensional analysis for the simulations developed in this chapter. Also, it is important to note that, only the first mode of the membrane is used to analyze the performance improvement and the 1-D analysis is sufficient for this purpose; thus, higher order vibration modes are not used for the dual-electrode CMUT structure.

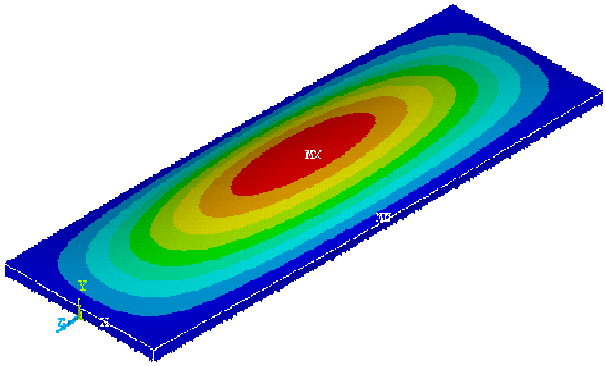

(a) f=15.4MHz

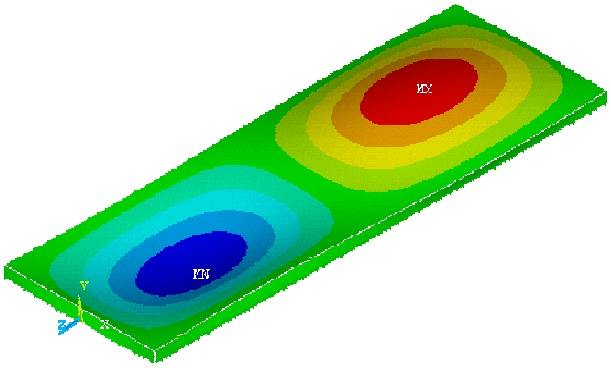

(b) f=28.1MHz

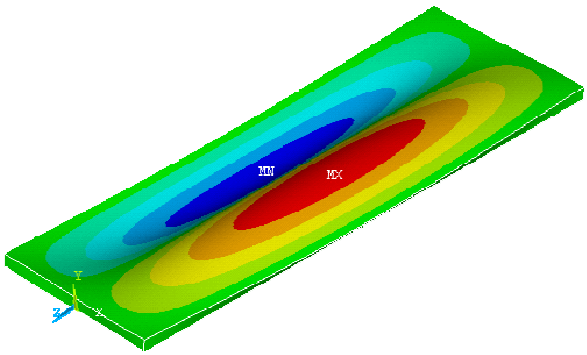

(c) f=31.2MHz

Figure 29 Three-Dimensional simulated vibration modes of a CMUT membrane with physical parameters given in Table 2

Figure 29 (Continued)

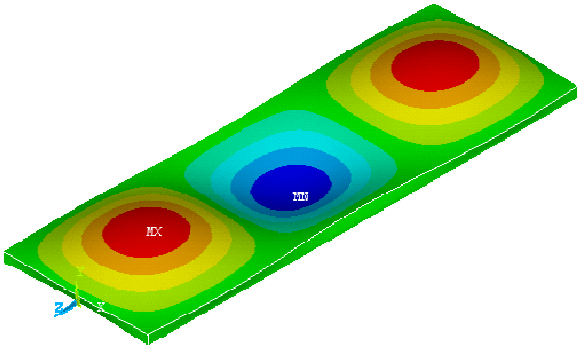

(d) f=38.6MHz

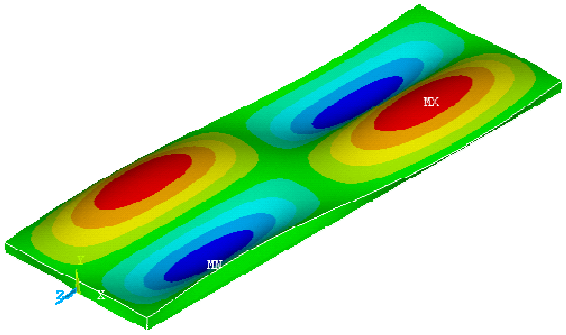

(e) f=38.9MHz

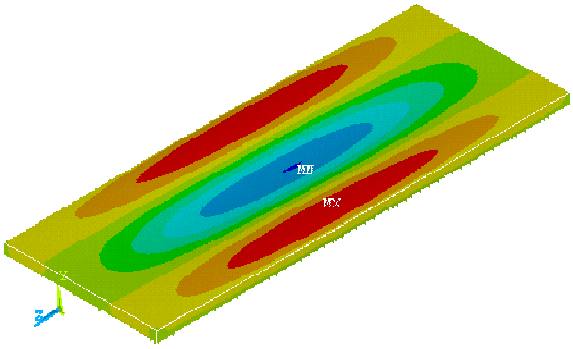

(f) f=46.7MHz

CHAPTER 4

DESIGN AND OPTIMIZATION OF DUAL-ELECTRODE CMUTS

Dual-electrode CMUT design needs more consideration as compared to conventional CMUTs due to the fact that both center *and* side electrodes exist in the membrane. Several authors have undertaken optimization studies for the top electrode (assuming that the bottom electrode covers the entire membrane) in terms of size and location in the membrane [13, 25, 32, 68]. However these optimization studies cannot be directly adapted to dual-electrode CMUTs. To quantify the effect of parameters on the CMUT performance, transformer ratio (n) and electromechanical coupling coefficient (k_c^2) is simulated for the receive mode of operation. Moreover, for the transmit mode of operation, the pressure output at the membrane and medium interface node is evaluated. Moreover, bandwidth and electrical isolation between side and center electrodes are also considered. The development of simulations for these figures of merit is explained in detail in Chapter 3.

4.1 Effect of Membrane Parameters

4.1.1 Membrane Width and Thickness

The physical dimensions of the CMUT array elements are determined by the desired center frequency and bandwidth. The element size should approximately be half the ultrasonic wavelength at the imaging frequency to avoid grating lobes in the field of view; therefore, a phased array operating at 7.5MHz in water should be made up of

elements not larger than 100μm. Note that smaller element sizes provide a larger field of view. Furthermore, adjusting the membrane thickness controls the center frequency and bandwidth of the CMUT. The effect of membrane parameters on the collapse voltage, transmit and receive figures of merit and 3dB one-way fractional bandwidth for a constant 8 MHz operation is shown in Table 3. For the simulations, the membrane gap is assumed to be 0.12μm and top electrode covering 50% of the membrane is separated from the gap by 0.25μm of silicon nitride isolation.

Table 3 Simulated membrane thickness and width pairs for 8MHz operational frequency and corresponding important transducer merits

Membrane Width (μm)	Membrane Thickness (μm)	Collapse Voltage (V)	Transformer ratio (n)	Bandwidth (%)	Output pressure (MPa)
100	5.6	110	0.21	60	0.81
48	3.5	105	0.13	80	0.66
30	2.5	95	0.11	100	0.57
20	1	75	0.08	110	0.49

One can observe from Table 3 that given the operational frequency, there is no optimum membrane width-height pair that will maximize all figures of merit. For instance, by increasing the membrane width and thickness, the output pressure and receive sensitivity increases, however, the bandwidth of the transducer is reduced and the collapse voltage is increased. On the other end of the spectrum, while high bandwidth is obtained with low collapse voltage, receive and transmit mode of operations become less efficient. Also note that due to the spacing between the center and side electrodes in the

membrane, in smaller membrane width-height designs (especially membrane width less than 20µm), the efficient area for locating electrodes is significantly limited. As a result, the optimum design depends on the application. During the course of this study, membranes with 48µm and 30µm widths are designed and used. However the analysis methods will be explained in detail for 48µm wide membrane.

4.1.2 Gap Thickness

In the previous section that summarizes the membrane width-height design optimization studies, the effect of gap thickness is ignored by assuming a constant gap thickness. However gap thickness may change some of the transducer merits and operation voltages significantly. To observe this effect, simulations are done illustrating the effect of gap thickness on the collapse voltage, receive and transmit figures of merit. The results for a 48µm wide, 3.5µm thick CMUT membrane with 50% top electrode coverage, separated from gap by 0.25µm of isolation are shown in Table 4.

Table 4 Simulated collapse voltage, transformer ratio, and output pressure as a function of gap thickness for a 48µm wide and 3.5µm thick CMUT membrane

Gap height (nm)	Collapse Voltage (V)	Transformer ratio (n)	Output pressure (MPa)
50	31	0.20	0.42
120	115	0.13	0.66
160	177	0.11	0.76
250	320	0.09	0.95

As can be observed from Table 4, decreasing the gap height reduces the collapse voltage significantly. Moreover, receive figure of merit – transformer ratio – is increased at a cost of significant reduction in transmit pressure. Hence from this analysis, one can once more observe that there is a contradiction in optimization criteria for the gap thickness. In this study, to have a transformer ratio comparable to piezoelectric transducers such as (PZT-5H) and reasonable collapse voltage, the gap thickness is chosen as 120nm to 160nm. Note that the ultimate gap thickness is limited by the roughness of the membrane which can be order of nm in PECVD nitride. Due to this reason, a 50nm gap thickness can create non-uniformity in the CMUT operation. Moreover, it is more probable to fabricate CMUTs with membranes collapsed due the atmospheric pressure on the evacuated cavity for thinner gaps. It is worthwhile to mention once more that by introducing dual-electrode structure to the membrane, receive sensitivity is increased as if having a small gap and transmit pressure is increased as if having higher gap height. Our simulations indicate that the gap height does not alter either the frequency response of the membrane nor the bandwidth.

4.1.3 Electrode Thickness

To investigate the effect of top electrode thickness on the frequency response of the membrane, collapse voltage, receive and transmit sensitivity a 48μm wide and 3.5μm thick CMUT membrane with a gap thickness of 120nm is simulated (Table 5). For the simulations, the top electrode which covers 50% of the membrane width is separated from the gap by 0.25μm of silicon nitride isolation.

Table 5 Simulated collapse voltage, operation frequency, transformer ratio, and output pressure as a function of top electrode thickness for a 48µm wide and 3.5µm thick CMUT membrane with a gap thickness of 120nm

Electrode Thickness (nm)	Collapse Voltage (V)	Frequency (MHz)	Transformer ratio (n)	Output pressure (MPa)
100	115	7.52	0.13	0.65
150	113	7.49	0.13	0.66
200	112	7.47	0.13	0.67
250	112	7.41	0.14	0.65

One can observe from Table 5 that the thickness of the top electrode does not change either the collapse voltage or the frequency response of the membrane significantly. Moreover, receive and transmit mode of operation figures of merit are also unaffected. Note that this result is only applicable for the range of top electrode thicknesses that are simulated. A top electrode thickness on the order of the membrane thickness will affect the mechanical properties of the membrane which in turn alters the frequency response and collapse voltage. Note also that the thin top electrode is advantageous in terms of reducing the thermal mismatch between metal and the dielectric membrane material, silicon nitride, during fabrication. However aluminum top electrode thickness less than 100nm should be avoided to allow sufficient electrical conductivity. In this study, top electrode thickness of 100nm to 120nm is found to be optimum for our design criteria.

4.1.4 Side Electrode Size and Location

The side electrode design in the dual-electrode configuration involves several considerations. The most important criteria are the membrane displacement just before collapse, output pressure and the collapse voltage. The membrane displacement just before the collapse is an important design consideration as it affects both transmit and receive mode performance. In transmit mode of operation, the higher the displacement before collapse, the higher the membrane swing, in return the higher the pressure output. In receive mode of operation, the higher the displacement before the collapse, the higher the active capacitance, in return the higher receive sensitivity. The effect of side electrode width on these parameters is shown in Table 6 for a 48µm wide and 3.5µm thick CMUT membrane with a gap thickness of 120nm. Side electrodes are isolated from the gap by 0.25µm of silicon nitride

Table 6 Simulated collapse voltage, maximum displacement, and output pressure as a function of the side electrode width

Side electrode width (µm)	Collapse Voltage (V)	Normalized membrane displacement just before collapse (%)	Output pressure (MPa)
2	910	85	0.73
6	375	69	0.66
10	240	64	0.63
14	201	59	0.56

We observe from Table 6 that by disregarding the collapse voltage constraint, it is possible to place a very small side electrode (limited by the lithography step resolution, typically 2μm) and to get displacement of 85% of the initial gap height. This design, however, would require 910V for operation. One more consideration is that given the membrane width, increasing the side electrode width reduces the area available for center electrode. As a result, one should place the smallest side electrode limited by the design collapse voltage. The 10μm side electrode gives 64% deflection at the center of the membrane while limiting the collapse voltage to a feasible value of 240V. Hence the achievable membrane swing of the membrane is increased from 1/3 of the gap to 2/3 of the gap, increasing both the pressure output and transformer ratio due to increased capacitance change.

Note that in the above simulations, the center of the side electrode is located laterally at a constant distance, 17μm from the center of the membrane. However the lateral location of the side electrode in the membrane can be adjusted. Table 7 illustrates the collapse voltage and the normalized center deflection of the same CMUT geometry just before collapse as a function of the distance from the edge of the membrane. Note that 10μm wide side electrodes are considered in these simulations.

Table 7 Simulated collapse voltage and normalized maximum displacement as a function of the side electrode distance from a 48 µm wide and 3.5µm thick CMUT membrane edge for 10µm wide side electrodes

Side electrode from membrane edge(µm)	Collapse Voltage (V)	Normalized membrane displacement just before collapse (%)
0	360	71
2	240	64
4	175	59
6	150	52

We observe from Table 7 that, moving the side electrodes closer to the edge of the membrane increases the membrane deflection before collapse at the expense of increased collapse voltage. This is an expected result as in the extreme case where the side electrodes are moved further from the edge, the electrostatic actuation of the membrane resembles that of a conventional CMUT which has a maximum normalized displacement of 1/3 of the initial gap height. Moreover, moving the side electrodes closer together limits the area available for center electrode. As a result, the side electrodes should be as close as possible to edges of the membrane within given design collapse voltage value. In this study, the side electrodes are chosen to be at 2µm from the edge of the membrane as moving them further, closer to the edges increases the collapse voltage beyond the 300V design limit.

4.1.5 Center Electrode Size

The center electrode is essentially reserved for receive mode operation; hence, transmit mode optimization does not need to be undertaken. In receive operation, the membrane is brought closer to the bottom electrode by side electrodes and a small bias is applied to the center electrode to increase the transformer ratio (n) or the electromechanical coupling coefficient (k_c^2). The simulated transformer ratio and collapse voltage as a function of center electrode width is represented in Table 8 for a 48 µm wide and 3.5µm thick CMUT membrane with optimized side electrode design (width: 10µm, distance from the edge: 2µm). The gap height is assumed to be 120nm.

Table 8 Simulated collapse voltage and transformer ratio as a function of center electrode width for a 48 µm wide and 3.5µm thick CMUT membrane

Center electrode width (µm)	Center-Side electrode separation (µm)	Collapse Voltage (V)	Transformer ratio (n)
5	9.5	150	0.41
10	7	130	0.41
15	4.5	110	0.42
20	2	95	0.42

As can be observed from Table 8, the transformer ratio is not dependent on the center electrode size. However, the bias needed to achieve the transformer ratio increases with decreased electrode sizes. Hence, using wider center electrode seems favorable. We note that using wider center electrode reduces the lateral spacing between side and center electrodes. This brings about the increase in the internal cross-talk between side and

center electrodes, the analysis of which is discussed in section 4.3. In addition, the distance between the side and center electrode is limited by the resolution in the lithography step-which is typically 2µm. As a result, in this study the center electrode width of 15µm is chosen. This width results in 4.5µm separation between the center and side electrodes.

4.1.6 Silicon Nitride Isolation Thickness

The CMUT designer has the freedom of choosing vertical location of both side and center electrodes in the membrane. Figure 30 illustrates the collapse voltage of the center electrode as a function of silicon nitride thickness. In the simulations, a 48µm wide and 3.5µm thick CMUT membrane with a 15 µm center electrode width and 120nm gap height is used.

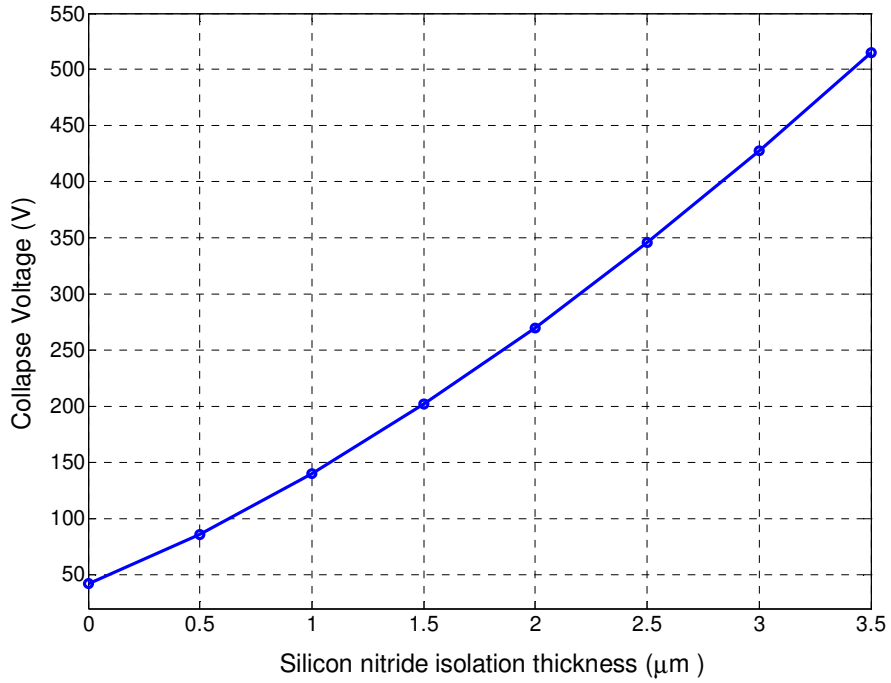

Figure 30 Simulated collapse voltage as a function of silicon nitride thickness for a 48 µm wide and 3.5µm thick CMUT membrane with gap height of 120nm.

We observe from Figure 30 that thinner isolation thickness between top electrode and sacrificial layer reduces the collapse bias significantly. Hence one should choose the isolation thickness as small as possible if not eliminate it completely. However in our current process flow, the sacrificial layer is chromium while the top electrode is aluminum. The detailed process flow is discussed in Chapter 5. If the isolation layer is completely eliminated, the aluminum top electrode is etched along with the sacrificial chromium during the sacrificial chromium layer release process. As a result, a thin nitride isolation layer is required for our fabrication process. To increase the yield, 0.25μm isolation layer is used between the top electrode and sacrificial layer. Thinner isolation layer thicknesses resulted in electrical shorting of the devices due to pin holes present in the Plasma Enhanced Chemical Vapor Deposition (PECVD) nitride. However different materials for sacrificial and/or top electrode can be employed that do not attack each other during patterning, etching, and release steps. One example is using chromium for sacrificial layer material and gold for top electrode material. However, there are inherent problems in using non-CMOS compatible metal-gold such as charge leakage over time. It is important to note that, the simulation results show that the thickness of the isolation layer for the range of interest does not affect the frequency response or the bandwidth of the membrane.

4.1.7 1-D Imaging Array Constraints

As discussed in section 4.1.1, the phased imaging array constraint limits the width of the element for viewing angle. Moreover, the total number of elements and the length of each element are determined by the physical constraints such as available space for the

transducer in the imaging probe. For the Intracardiac Echocardiography (ICE) imaging catheter, the total space for the whole transducer is around 6.8mm by 2.4mm. Hence in our design, 64 elements are used with a pitch of 105µm (total size 6.72mm). Individual cell size of 48µm by 100µm is used as a basic building block and 48 of such cell are connected to give a single element of 100µm by 2.4mm as illustrated in Figure 31. The overall design parameters are also summarized in Table 9.

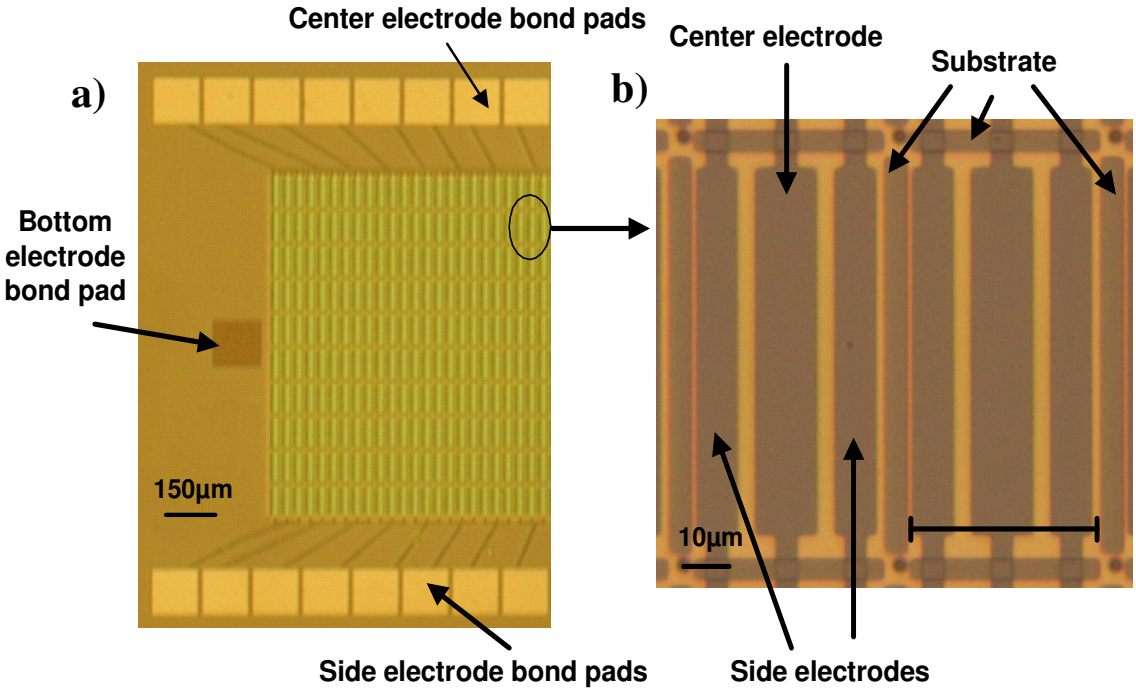

Figure 31 Micrographs of dual-electrode CMUTs. a) Overall view of 8 elements of a 64 element dual-electrode CMUT array b) Close up view of dual-electrode two 48µm CMUT membranes with 15µm side and 10µm center electrodes

Table 9 Physical array and membrane parameters used in the design and fabrication

Number of Array Elements	64
Element Size	100μm×2.4mm
Cell size	48μm×100μm
CMUT Cells per element	48
Gap/isolation thickness	0.1μm/0.25μm
Total membrane thickness	3.5μm
Center/side electrode sizes	15μm/10μm

4.2 Effect of Non-Uniform Membrane Structure

The effects of non-uniform membrane shape for conventional CMUT design was previously investigated by several research groups. One approach used notches in the membrane design [56, 57]. Improvement in transduction performance was shown. Another successful alternative was placing a center mass on the CMUT membrane [13, 54, 55]. Both bandwidth and transduction performance increase was demonstrated. The design space for dual-electrode CMUTs can also be increased by non-uniform membrane approaches. Simulation studies are conducted on dual-electrode CMUTs to investigate the effect of non-uniform membrane implementation on transducer performance, bandwidth, and collapse voltages. In the following sections, two of these approaches are summarized: membrane with notches between electrodes and membrane with center mass loading.

4.2.1 Membrane with Notches

As a possible way to improve dual-electrode CMUT performance, placing notches in the membrane structure is investigated (see Figure 32).

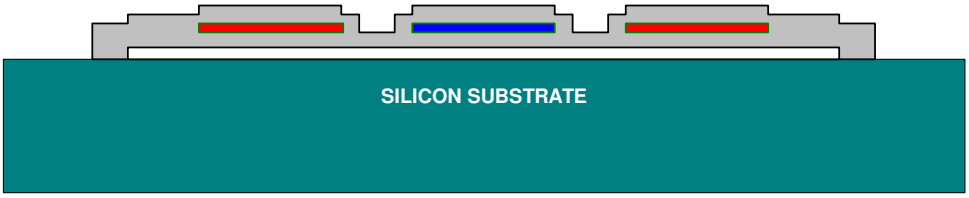

Figure 32 One-Dimensional scaled rendering of dual-electrode CMUT with notches between side and center electrodes

The width, depth, and location of the notch may affect the membrane response. Both receive and transmit mode performance improvements are investigated to obtain the optimized structure. The optimized geometry with membrane parameters summarized in Table 9 is used for further optimization studies. In order to compare two similar transducers, the frequency response of the membrane is compensated for by adjusting the overall membrane thickness. Figure 33 shows the simulated CMUT membrane deflection just before collapse when the center and side electrodes are used to apply electrostatic pressure with/without notches. The side electrode excitation increases the volumetric displacement by 6.8 dB (2.2×) as compared to center electrode excitation. Moreover, when 2µm wide, 1µm deep notches are placed between the center and side electrodes (center of the notch being at ± 13µm) in the design, the performance improvement with side electrode excitation reaches 8.9dB (2.8×). Note that with the notch introduced to the design, maximum displacement is increased and also the membrane profile approaches

that of the parallel plate capacitor (as illustrated in Figure 33). Both of these factors contribute to improved transmit and receive modes of operation.

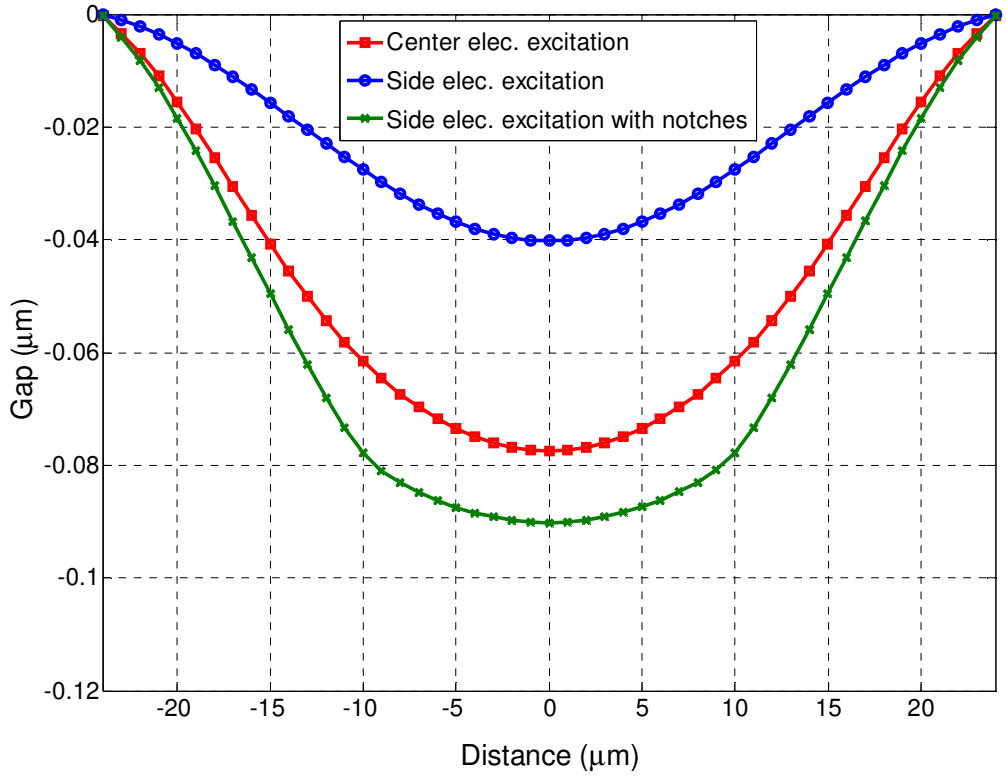

Figure 33 Deflection of the CMUT membrane just before the collapse when excited by the center electrode and side electrodes with/without notches.

Although placing notches in between electrodes increase performance, the location of the notch should be investigated for optimization. Our simulations indicate that the pressure output does not change significantly (within ±5%) as a function of lateral notch location while keeping the width and depth of the notch constant. In addition to transmit pressure, electromechanical coupling coefficient (k_c^2) and the transformer ratio (n) of the equivalent circuit improvements are also investigated. Both of these latter figures of merit are simulated. The transformer ratio and the electromechanical coupling

coefficient do not change significantly as a function of lateral position of notch, similar to the results obtained for the pressure output. Figure 34 illustrates two extreme cases, one where the notch is placed at the edge of the membrane and one where the notch is placed between the side and the center electrodes (center of notch at ±13µm). Both the pressure output values and the electromechanical coupling coefficient are similar even for these two extreme cases.

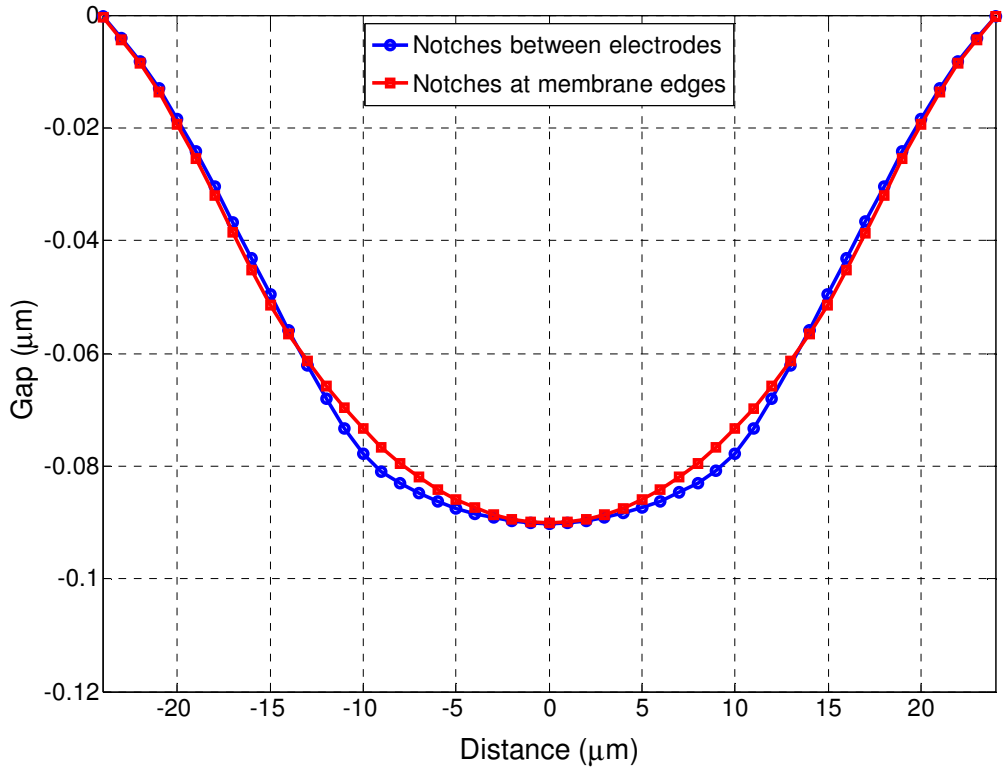

Figure 34 Deflection of the CMUT membrane just before collapse when excited by the side electrode with notches located at the two extreme cases.

Table 10 summarizes the pressure output at the medium membrane interface node and collapse voltages for varying notch thicknesses and depths. Note that the pressure output values are obtained while DC biasing the membrane at 90% of the collapse voltage for each case.

Table 10 Simulated pressure output and collapse voltage as a function of notch parameters for a notch located at ±13μm in the membrane.

Notch Width (μm)	Notch Thickness (μm)	Side Collapse Voltage (V)	Output Sensitivity (KPa/V)
0	0	240	12.3
2	2	206	15.6
2	1	210	15.4
2	0.5	213	15.4
1	0.5	215	14.9

We observe from Table 10 that placing notches in the design reduces the collapse voltage while increasing the output sensitivity. Wider and deeper notches result in increased transmit sensitivity. One important consideration is the bandwidth of the membrane with notches. When the notch is introduced, the effective membrane thickness is reduced, resulting in lower operation frequency with a higher bandwidth. However, when the membrane thickness is increased to compensate for the reduction of operational frequency, the bandwidth is decreased. Hence, the bandwidth of the membrane with/without the notch is not significantly changed as long as the effective membrane thickness (i.e. operational frequency) is kept constant. In the order to evaluate receive improvements achievable with dual electrode design with notch introduction, both the side and center electrode are used in the analysis. Simulations show that just like the uniform membrane CMUTs, for the highest achievable electromechanical coupling coefficient (k_c^2), the side electrode bias should be increased as much as possible without

moving the membrane into the contact region. With the applied side bias, the center electrode should be operated close to collapse. The result of receive mode analysis is summarized in Table 11.

Table 11 Electromechanical coupling coefficient attainable with dual-electrode CMUTs with varying notch parameters located between side and center electrodes

Notch Width (µm)	Notch Thickness (µm)	Side/Center Bias (V)	Transformer ratio (n)	Coupling coefficient (k_c^2)
0	0	160/76	0.42	0.71
2	2	148/68	0.48	0.80
2	1	150/70	0.48	0.79
2	0.5	150/72	0.48	0.79
1	0.5	155/74	0.47	0.78

We observe both from Table 10 and Table 11 that, the wider and deeper notches increase both transmit and receive performance. Having 2µm wide and 2µm deep notches between side and center electrodes improves the transduction performance of dual-electrode CMUT by 3.1dB (2.1dB in transmit mode of operation and 1dB in receive mode operation). Note that this is in addition to 16dB transduction improvement achievable with uniform membrane dual electrode structure as compared to conventional CMUTs. On the other hand, the lateral location of the notch in the membrane does affect either the pressure output or the coupling coefficient significantly. However, the notches may cause the stress distribution to change significantly in the membrane leading to fatigue or fracture formation. To evaluate this effect, the stress distribution with/without notches is plotted in Figure 35. As can be observed from Figure 35, the maximum stress

is concentrated at the edges of the membrane regardless of the presence of notches. Hence, it can be concluded that notch introduction does not decrease the reliability of CMUT membranes. Fabricated devices would not have such sharp edges which would further reduce the stress concentrations.

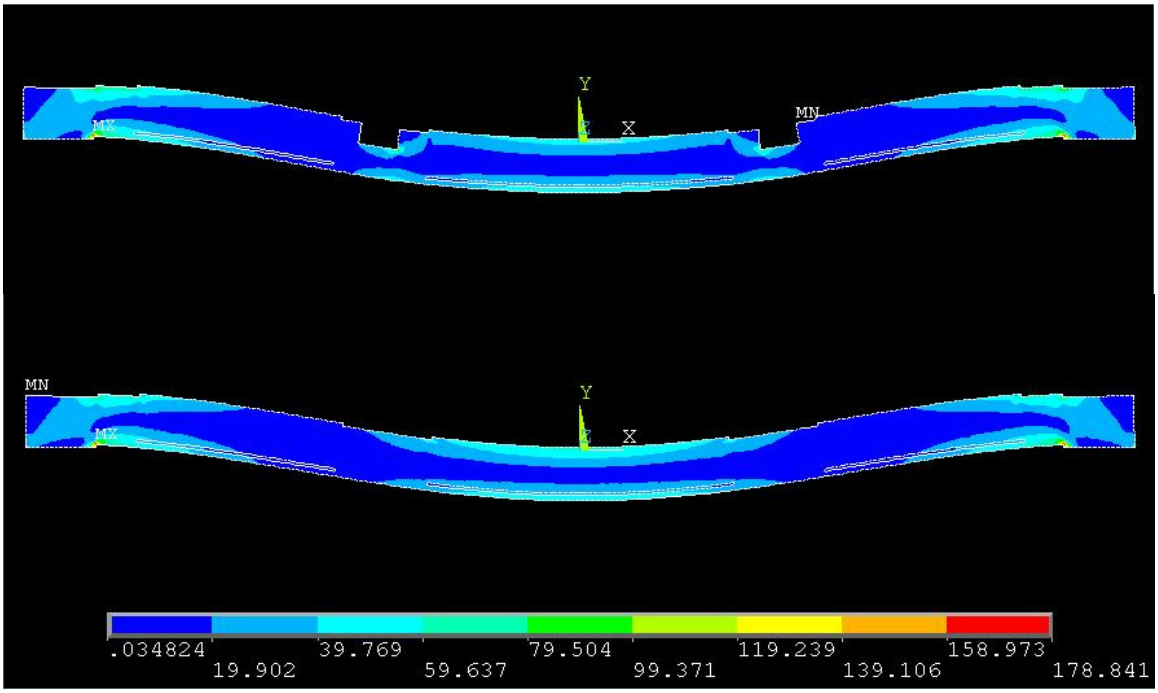

Figure 35. Stress distribution in the membrane just before collapse for the design with/without notches present in the design.

4.2.2 Membrane with Center Mass

As another alternative, a non-uniform membrane with the addition of a center mass is investigated, a sketch of which is illustrated in Figure 36 [13, 54, 55]. This membrane modification changes the membrane structure significantly. The optimization of the non-uniform membrane is involved since several parameters can be changed, namely: center mass width, center mass thickness and membrane thickness. There are several optimization criteria in the design. The operation frequency should not be changed as compared to uniform membrane and the fractional bandwidth, receive and transmit sensitivity should be maximized.

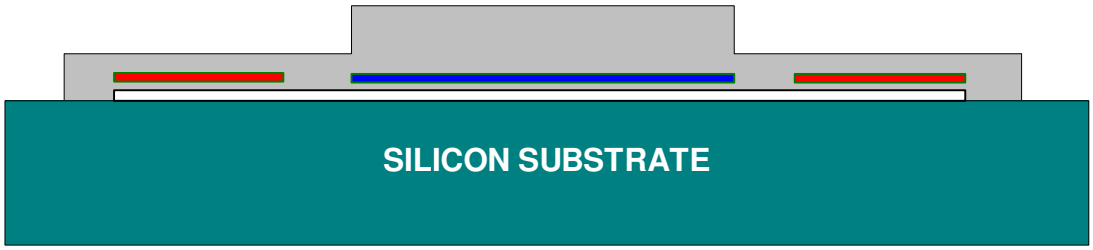

Figure 36 Scaled rendering of a non-uniform membrane dual-electrode CMUT with a center mass.

In this study, the width of the center mass is chosen to be the spacing of side electrodes from each other. As a result, for the optimized membrane parameters given in Table 9, the center mass width is 24 μm. Before optimizing the thickness of the membrane and thickness of the center mass for operation at 8MHz, the effect of center mass on the frequency response is simulated. The operation frequency and bandwidth as a function of center mass thickness is illustrated in Figure 37.

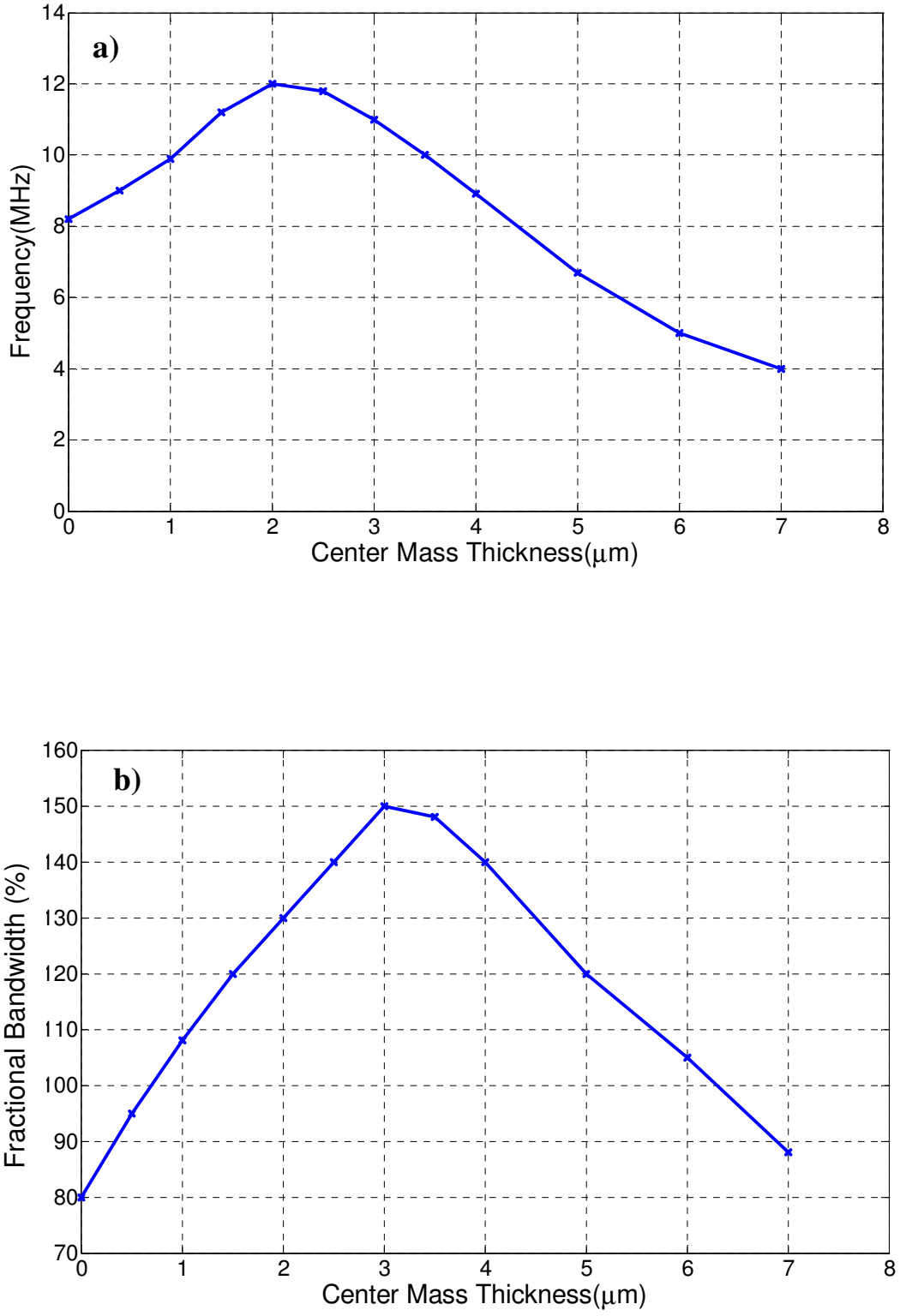

Figure 37 a) Simulated operation frequency for a non-uniform membrane with varying center mass thickness b) Fractional bandwidth as a function center mass thickness

We observe from Figure 37 that operation frequency first increases as a function of center mass thickness however after reaching a maximum value it reduces [55]. The reason for such an occurrence can be explained by investigating the analytical frequency response of a membrane:

$$w = \sqrt{\frac{k}{m}} \tag{36}$$

where k is the stiffness and m is the effective mass of the membrane. Adding a center mass to the design has two competing effects for the frequency response: increasing the effective mass of the structure (which decreases the frequency response) and increasing the stiffness (which increases the frequency response). The relative effect of these competing factors results in the trend observed in Figure 37 (a). The frequency is increased from 8 MHz to 12 MHz for a center mass thickness 2μm, while further increasing the center mass thickness reduces the frequency response of the membrane. Similar effects can be observed for fractional bandwidth of the membrane as illustrated in Figure 37 (b). However, maximum fractional bandwidth is obtained for a center thickness of 3μm. Note from Figure 37 (a) and (b) that there are two center mass thickness for a given operational frequency and fractional bandwidth. In this study, the thinner center mass thickness is chosen for a given operational thickness as the fractional bandwidth is higher. Also the maximum achievable operational frequency is limited by the membrane thickness regardless of the center mass thickness.

The membrane profile for 2μm center mass thickness for the optimized 3.5μm membrane thickness (membrane parameters given in Table 9) with 0.12μm gap thickness

is illustrated in Figure 38. We observe from Figure 38 that the addition of a center mass to the design both increase the maximum deflection (to 3/4 of the gap) and makes the deflected membrane profile more uniform which ultimately increase receive and transmit sensitivities.

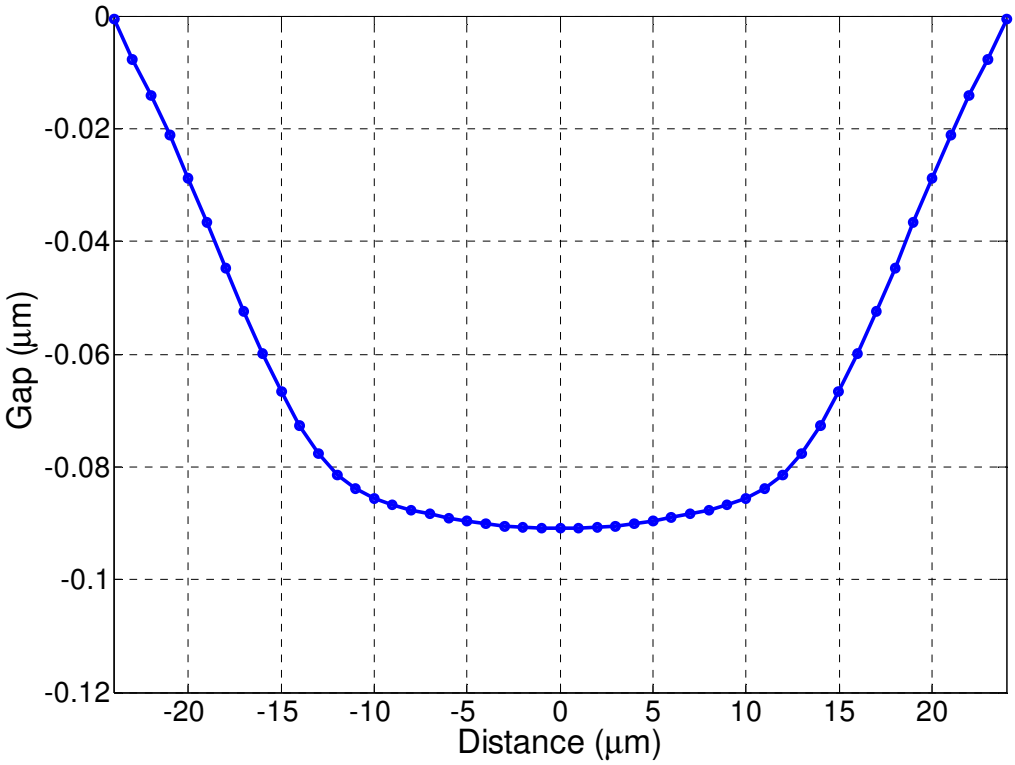

Figure 38 Deflection of the non-uniform CMUT membrane with center mass just before collapse when excited by side electrodes

To optimize the 8MHz CMUT design with center mass addition, the center mass thickness and membrane thickness are varied for a constant 24µm center mass width. Table 12 summarizes the simulation results with varied membrane-center mass thickness pairs.

Table 12 Simulated performance improvements achievable with non-uniform membranes with center mass and corresponding operational points.

Membrane Thickness (µm)	Center Mass Thickness (µm)	Bandwidth (FBW %)	Side/Center Bias (V)	Transformer ratio (n) / Coupling coefficient (k_c^2)	Side Collapse Voltage (V)	Transmit Sensitivity (KPa/V) / Pressure Output (MPa)
3.5	0	80	N/A/115	0.13/0.24	N/A	12.1/0.66
3.5	0	80	160/76	0.42/0.73	240	12.3/1.48
3	1	120	137/76	0.48/0.79	209	13.1/1.47
2.75	1.5	140	132/74	0.52/0.85	198	15.4/1.53
2.5	2	150	124/71	0.49/0.82	181	15.3/1.38

As can be observed from Table 12, decreasing the membrane thickness and increasing the center mass thickness significantly increases the bandwidth of the membrane while reducing the required bias values. Note that the first row shows simulation results for conventional CMUT with a uniform membrane while the second row in Table 12 is for the uniform membrane dual-electrode CMUT. The center mass addition to the design is so effective that decreasing the membrane thickness to 2.5µm (from 3.5µm) and adding 2µm center mass results in almost doubling the fractional bandwidth (80% to 150%). Moreover, the side electrode collapse voltage is reduced nearly by 25% (from 240V to 181V). Additionally, transmit and receive figures of merit are increased with center mass introduction to design. We observe from Table 12 that the optimum membrane thickness is 2.75µm which corresponds to a center mass thickness of 1.5µm for 8 MHz operation. When this design is compared to uniform membrane dual electrode, both receive and transmit figures of merit are increased. Moreover, the

required side bias value is reduced by 20% and the fractional bandwidth is increased by 75%. This optimized non-uniform membrane increases the transduction performance by 3.6dB (1.6dB in receive and 2dB in transmit) as compared to optimized uniform membrane dual-electrode CMUT configuration. It is worth noting that the obtained performance improvements are in addition to already demonstrated 16dB performance improvement with dual electrode structure as compared to the single electrode case. Also note that when the membrane thickness is further reduced and center mass thickness is increased, receive and transmit figures of merit start to degrade. Also from Table 12, as the side electrode bias requirement is reduced, the maximum pressure on the membrane does not scale with transmit sensitivity. However, the net pressure output on the membrane is still increased due to significant increase in transmit sensitivity. The electromechanical coupling coefficient (k_c^2) for the uniform membrane dual-electrode and conventional CMUT with physical parameters given in Table 12 is illustrated in Figure 39. Optimized non-uniform membrane dual-electrode and conventional CMUTs (membrane thickness of 2.75μm and center mass thickness of 1.5μm) is also shown in the same figure.

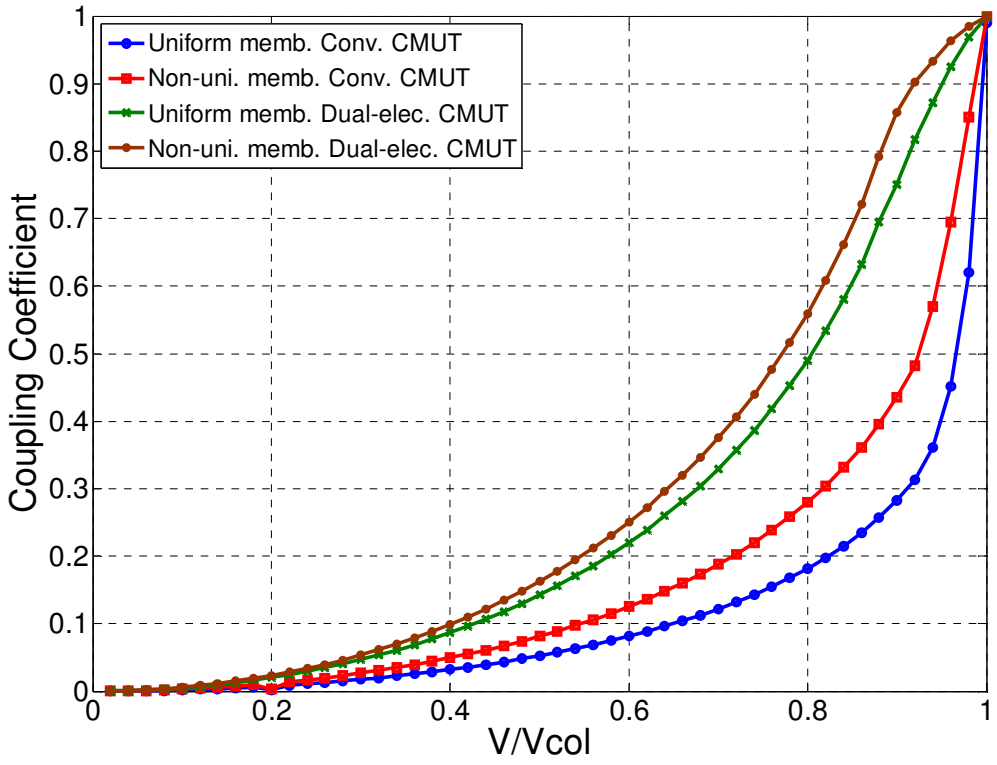

Figure 39 Simulated electromechanical coupling coefficient as a function of normalized voltage for uniform / non-uniform membrane dual-electrode and conventional CMUTs

One can observe from Figure 39 that introduction of a center mass to both dual-electrode and conventional CMUT designs increase the electromechanical coupling coefficient. For the dual-electrode CMUT, the non-uniform membrane increases the electromechanical coupling coefficient to 0.85 from 0.73 for uniform membrane dual-electrode CMUT at 90% of the collapse voltage. Similarly, the electromechanical coupling coefficient is increased to 0.43 from 0.28 with center mass introduction to the design.

Figure 40 illustrates the stress distribution in the non-uniform membrane with center mass. One can observe that the maximum stress concentration locations are at the edges of the membrane. As a result, the center mass introduction does not create stress

concentration locations along the membrane. This result is important for the operation of non-uniform dual-electrode CMUTs.

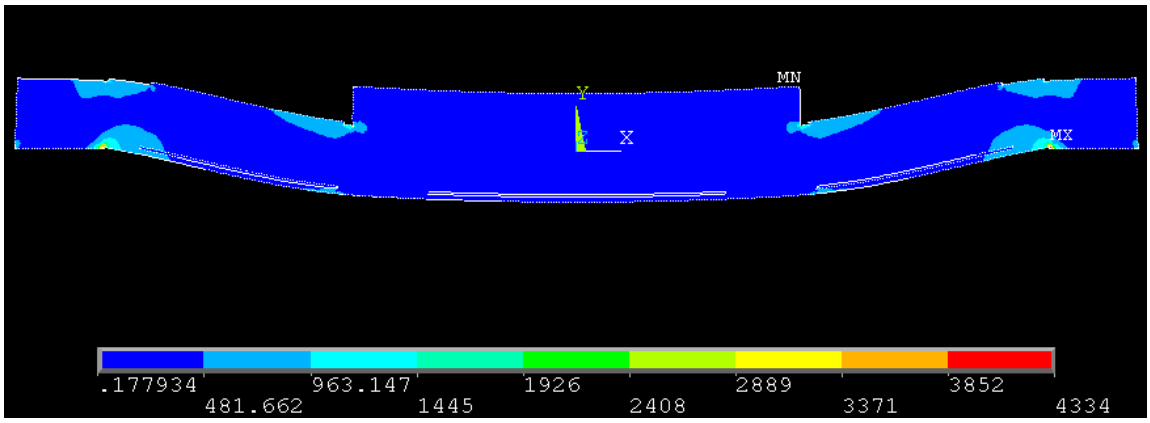

Figure 40 Stress distribution along the membrane for a non-uniform dual-electrode membrane with center mass

4.3 Electrical Isolation of Side and Center Electrodes in the Membrane

Cross talk between side and center electrodes can be problematic in dual-electrode CMUTs. The large AC pulse that is applied to the side electrodes for transmit mode should be well isolated from the center receive electrode in order to not saturate the receive amplifier. Also, the capacitance between the center receive and side transmit electrodes act as a parasitic capacitance and should be minimized. Hence electrical isolation of side and center electrodes is an important figure of merit that may affect the design parameters for achieving optimal performance. To cover all possible applications of dual-electrode CMUTs, three medium of interest are investigated: namely, air, water and oil. Oil is included as a possible medium because its electrical permittivity is low allowing for bond-wire isolation. Moreover, just like water, oil mimics the properties of tissue however the attenuation in oil is higher than water.

The simulation code developed was previously explained in chapter 3. In short, the CMATRIX macro is employed to find the active capacitance of the receive center electrode ($C_{receive}$) and the cross capacitance between the transmit and receive electrodes (C_{cross}) as illustrated in Figure 41. The medium of interest in contact with the membrane is also modeled (not shown in Figure 41 for the sake of clarity). Before solving for the capacitance values, deflection of the membrane with the given optimum side and center electrode bias values is simulated and the deflection profile is stored as an initial condition to the capacitance macro. The optimized CMUT parameters, as illustrated in Table 9, are used as the starting point for the analysis. In this section, the effect of several membrane parameters and media of interest on the internal cross-talk will be investigated and possible cross-talk reduction methods will be discussed.

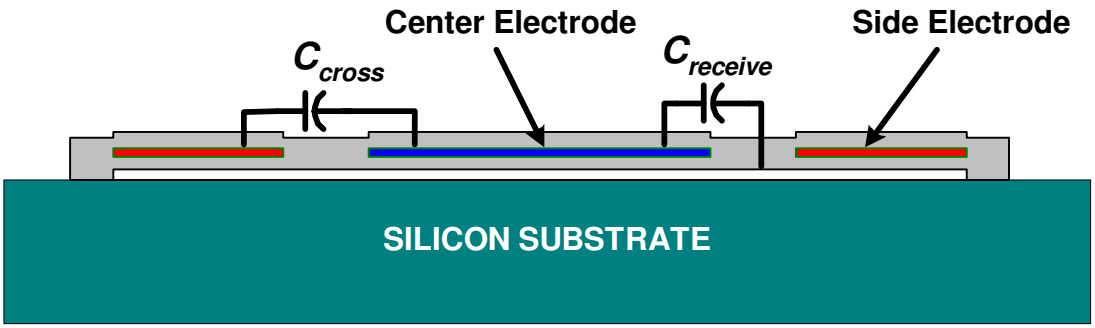

Figure 41 Scaled rendering of a dual-electrode CMUT used for FEA and the capacitances relevant to electrical isolation analysis

4.3.1 Effect of Membrane Parameters and Medium on Electrical Isolation

4.3.1.1 Operation in air

Before delving into a discussion on the effect of membrane dimensions on the element-wise cross-talk, it is important to note that the 1-Dimensional analysis in Ansys assumes the depth of the geometry to be 1m. Hence, the results are multiplied by the depth of the membrane to obtain the capacitance value for the membrane. However, the electrical isolation does not depend on the depth of the electrode as the analysis disregards the effect of parasitic capacitance. In the analysis, the relative permittivity of air is taken as 1 (unity). With the given parameters in Table 9, regardless of medium thicknesses above 10µm, the ratio of the active receive capacitance to the cross capacitance between side and center electrode is 37.2dB (a cross capacitance value of 0.12pF). The reason for such an occurrence can be explained by Figure 42 which illustrates the electrical field lines for the cross capacitance calculation. The fringing field goes as much as 7µm into the medium of interest. Hence, taking 10µm thick medium in the analysis is sufficient for the accuracy of the analysis.

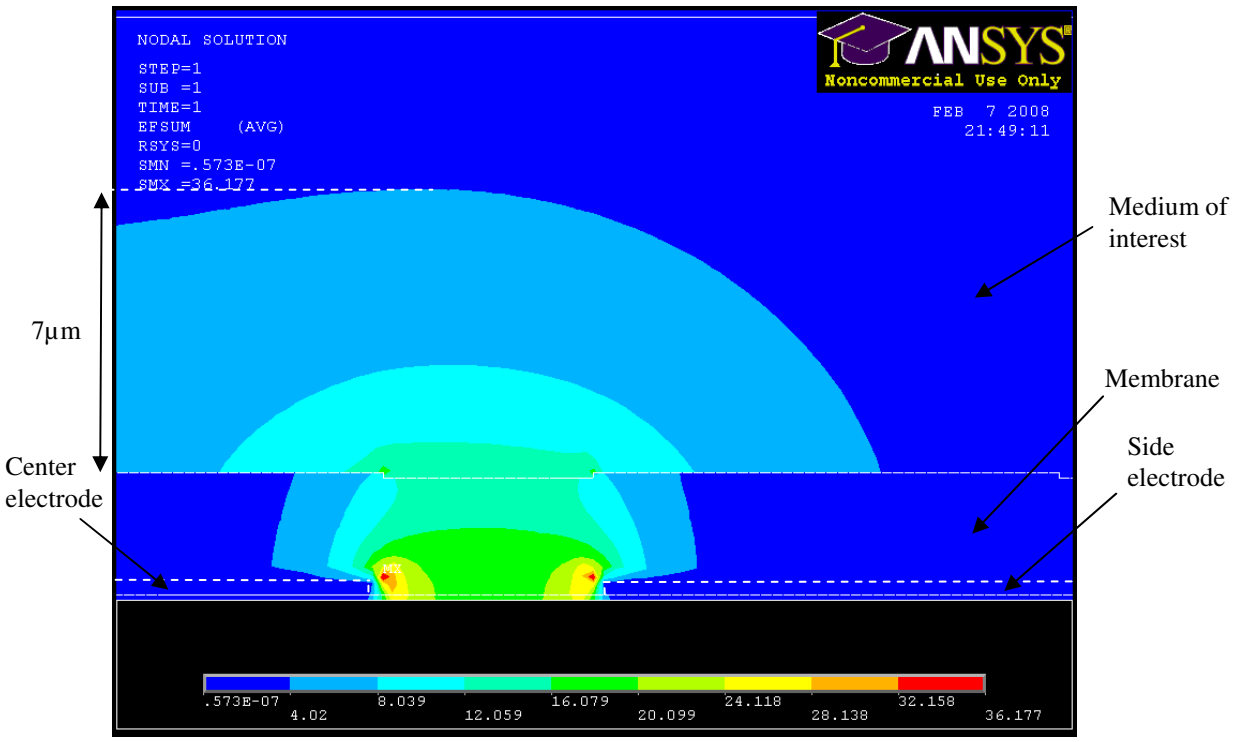

Figure 42 Simulation results showing the electrical field between side and center electrode in air (C_{cross})

After the medium thickness to be modeled is determined, the effect of several membrane parameters on the cross talk is investigated. The separation of center and side electrodes as a function of the electrical isolation (ratio of active capacitance, ($C_{receive}$) to cross talk capacitance (C_{cross})) is illustrated in Figure 43. As long as the electrode width is kept the same, the active receive capacitance is independent of the separation distance between side and center electrodes. On the other hand, the cross capacitance is decreased from 0.33pF for 2µm of separation to 0.1pF for 5.5µm separation. This is an expected result as capacitance is inversely proportional to the distance between conductors. As a result, the ratio of receive capacitance to cross capacitance is increased when the separation is increased between electrodes.

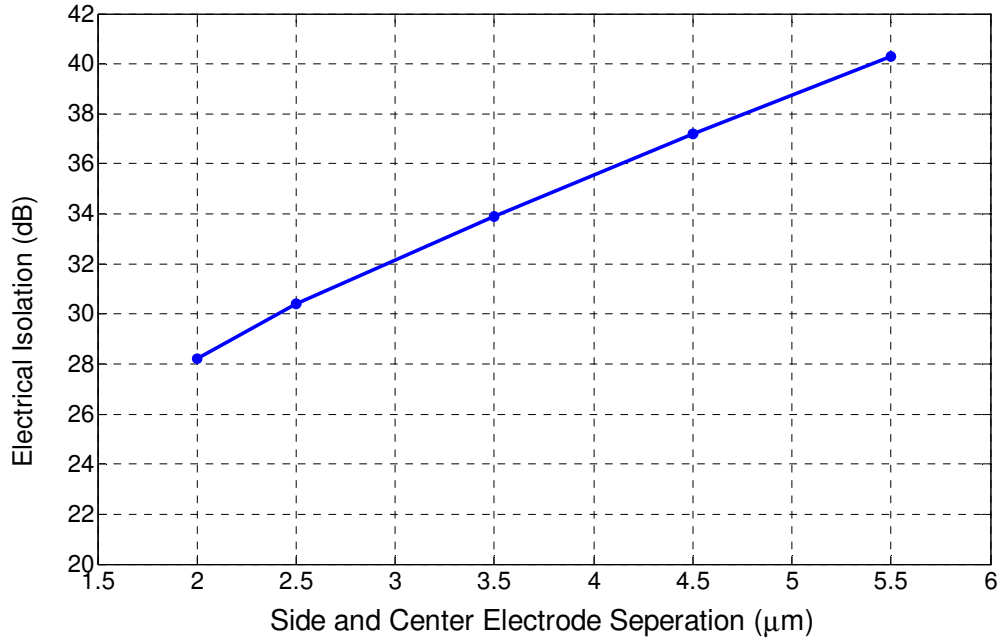

Figure 43 Simulated electrical isolation as a function of separation between side and center electrodes in the membrane

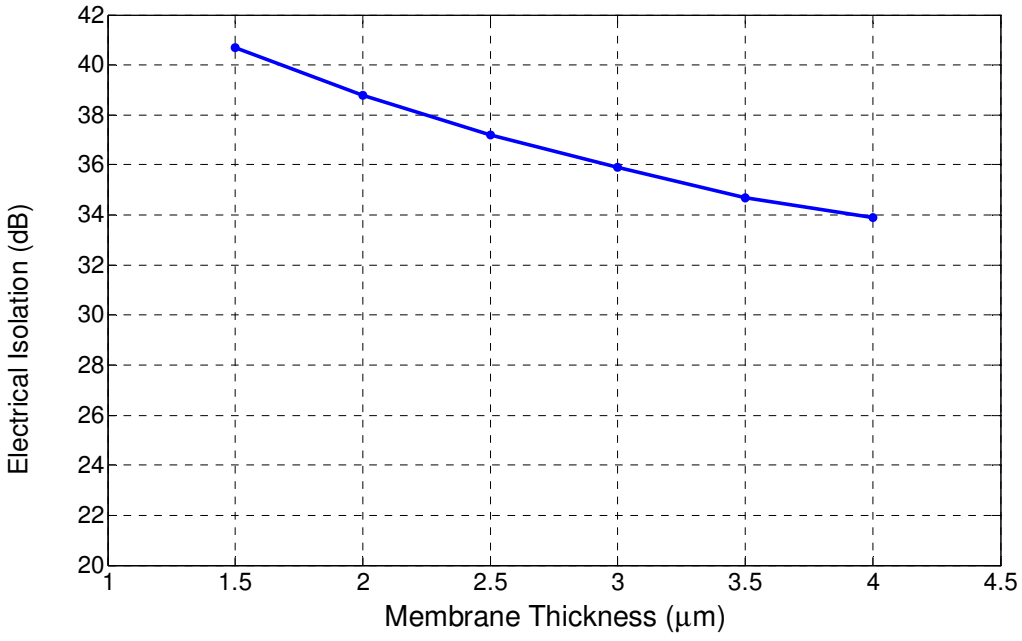

Figure 44 Simulated electrical isolation as a function of membrane thickness for operation in air

The effect of membrane thickness on the electrical isolation is also investigated. As can be observed from Figure 44, thicker membrane thicknesses increase the electrical isolation. Note from Figure 42 that the fringing field lines go as high as 7μm above the conductors; as we increase the membrane thickness, literally, a higher electrical permittivity material nitride (ε_r=6.3) than air (ε_r=1) is placed along the electrical field which increase the cross capacitance. Note that the cross capacitance is increased from 0.08pF for 1.5μm membrane thickness to 0.17pF for 4.5μm membrane thickness. Conversely, the active receive capacitance is unchanged as the distance between conductors for receive capacitance is kept constant. Hence, the electrical isolation is decreased for increased membrane thickness. However, if the medium of interest has higher permittivity than silicon nitride, increasing the membrane thickness decreases the cross-capacitance ratio.

The effect of gap thickness on the electrical isolation is illustrated in Figure 45. Decreasing the gap thickness increases the active receive capacitance while the cross-talk capacitance is not affected significantly with different gap thicknesses (0.1pF for a 50nm gap thickness and 0.13pF for a 0.2μm gap thickness). As a result, as observed from Figure 45, having a smaller gap thickness is more advantageous as far as electrical isolation is concerned.

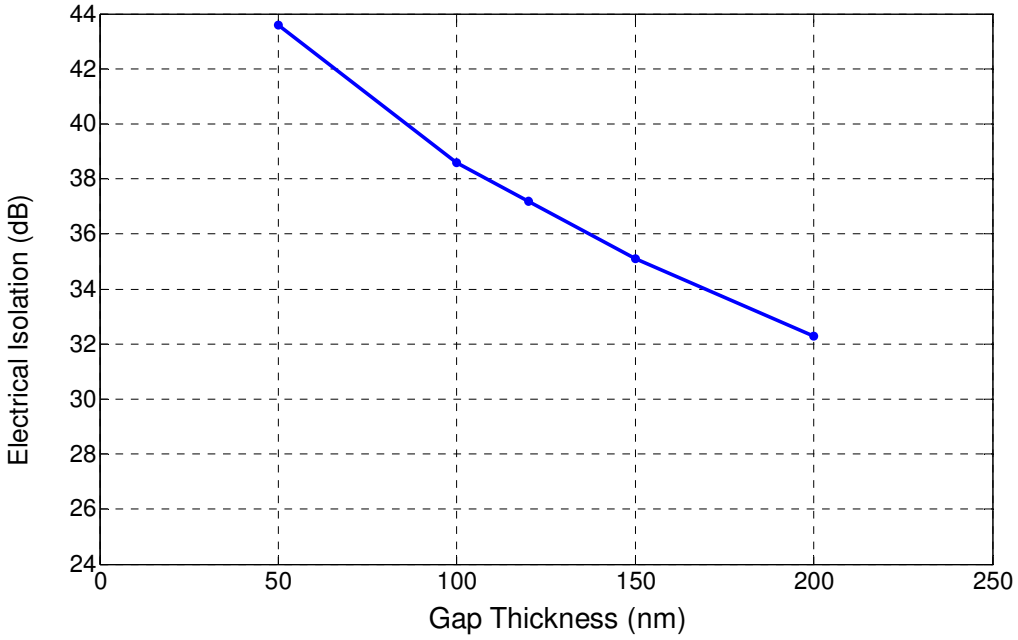

Figure 45 Simulated electrical isolation as a function of gap thickness for operation in air

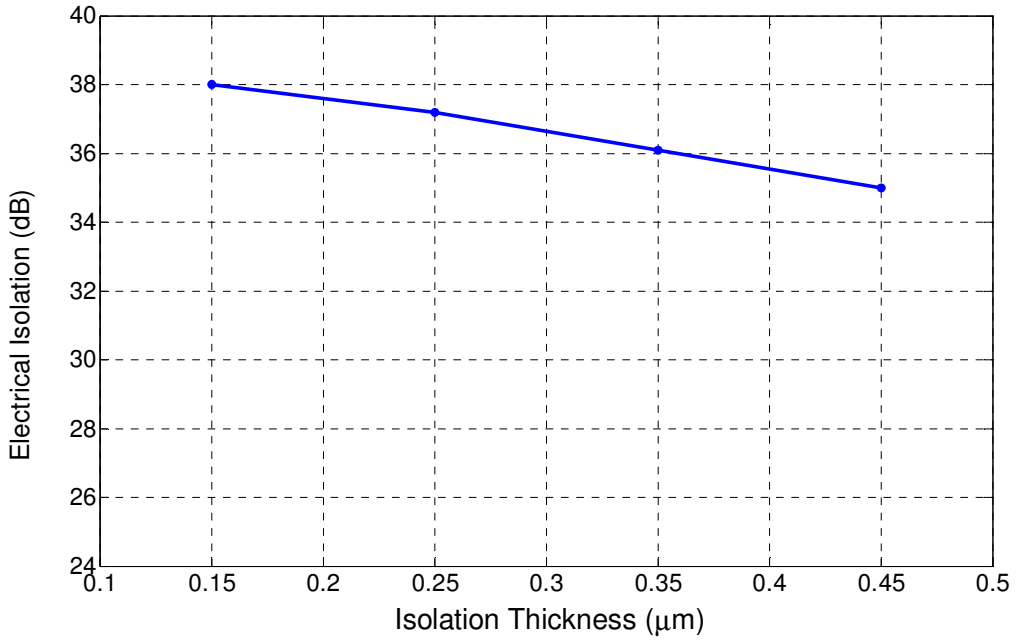

Figure 46 Simulated electrical isolation as a function of isolation thickness for operation in air

Moreover, the effect of the silicon nitride isolation thickness between top electrodes and sacrificial gap is illustrated in Figure 46. The isolation thickness has a similar effect on the electrical isolation as the effect of the gap thickness. However as the isolation thickness is normalized by the relative permittivity of nitride for equivalent gap calculation (equation (9)); its effect on electrical isolation is suppressed. Hence the isolation thickness has a similar, yet less pronounced trend as gap thickness to electrical isolation.

The effect of electrode thickness on the electrical cross-talk is shown in Figure 47. As the most of the electric field occurs as fringing field between side and center electrode, the electrode thickness does not effect either the active receive capacitance or the cross talk capacitance between transmit and receive electrodes for the investigated thickness range.

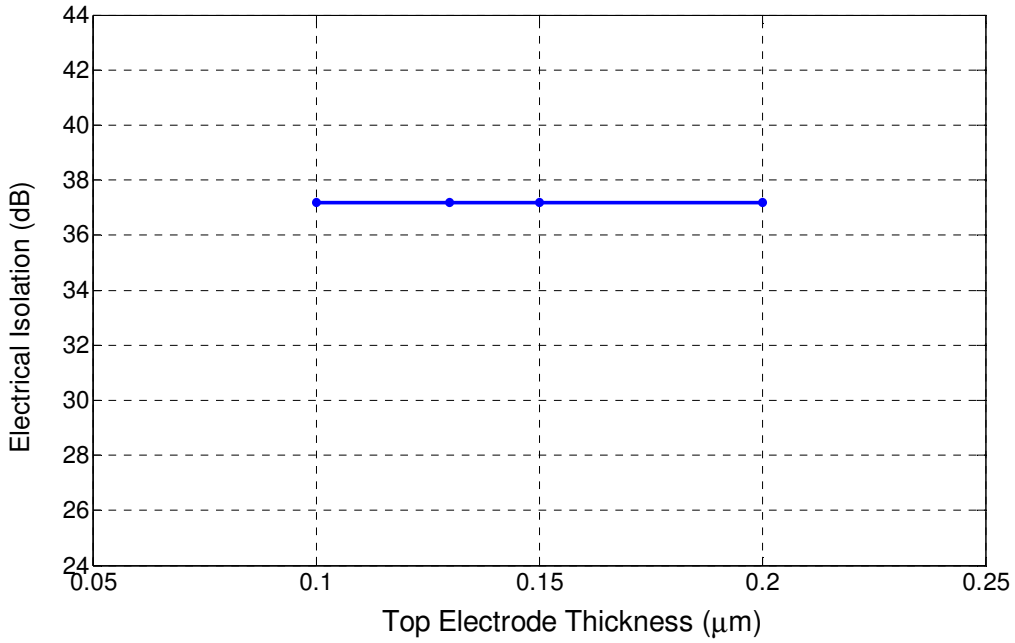

Figure 47 Simulated electrical isolation as a function of top electrode thickness for operation in air

4.3.1.2 Operation in oil

The relative permittivity of air is unity, and oil has a relative permittivity of 2. Hence when we employ oil as medium of interest, higher permittivity material is inserted into the path of electrical field lines. This causes the cross capacitance between center and side electrodes to increase (from 0.12pF for air operation to 0.16pF for oil operation) while the active receive capacitance is unaffected. The electrical field lines for the cross-capacitance are illustrated in Figure 48. Note that the electrical fringing fields go as high as 6μm into the oil medium, reduced from 7μm as compared to air. This translates into a higher cross capacitance value and eventually, electrical isolation is decreased by 2.5dB (to 34.7dB for the geometry parameters in Table 9) when oil is employed as a medium of interest as compared air.

The effect of the membrane parameters on the electrical isolation is similar to the air operation as oil has a lower permittivity (ε_r=2) than the structural silicon nitride layer (ε_r=6.3) used in the membrane. Increase in distance between the center and side electrodes decreases the electrical isolation considerably as the gap between conductors is increased. Having a thin membrane thickness is advantageous in that the lower permittivity layer (oil) is placed along the cross talk electrical field line path. Decreasing both gap thickness and nitride isolation layer between top and bottom electrodes increase the electrical isolation mainly due to increased active receive capacitance.

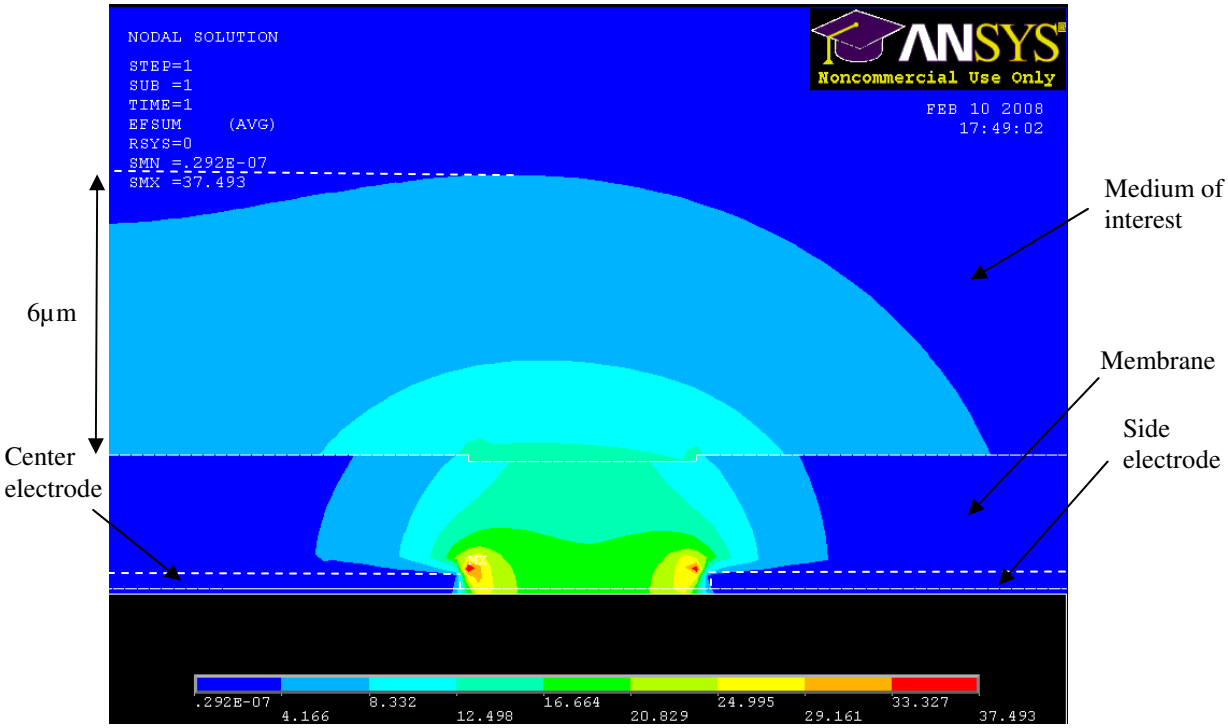

Figure 48 Simulation result showing the electrical field between side and center electrode in oil (C_{cross})

4.3.1.3 Operation in water

The relative permittivity of water (ε_r=80) is very high as compared to that of air (ε_r=1) and oil (ε_r=2). As can be observed from Figure 49, the electrical field lines do not penetrate into the water. As a result, the cross talk capacitance is significantly increased during operation in water. Note that removing the water and inserting a thin conductive metal layer gives similar cross talk capacitance. Hence, the water-membrane interface acts like a conductive plane. Moreover, as the relative permittivity of water (ε_r=80) is higher than the relative permittivity of structural silicon nitride (ε_r=6.3), the effect of some membrane parameters are different than the ones obtained in oil and air operation. With the membrane parameters given in Table 9, the electrical isolation is reduced to

21.7dB. (Cross talk capacitance increased from 0.12pF for air operation to 0.75pF for water operation).

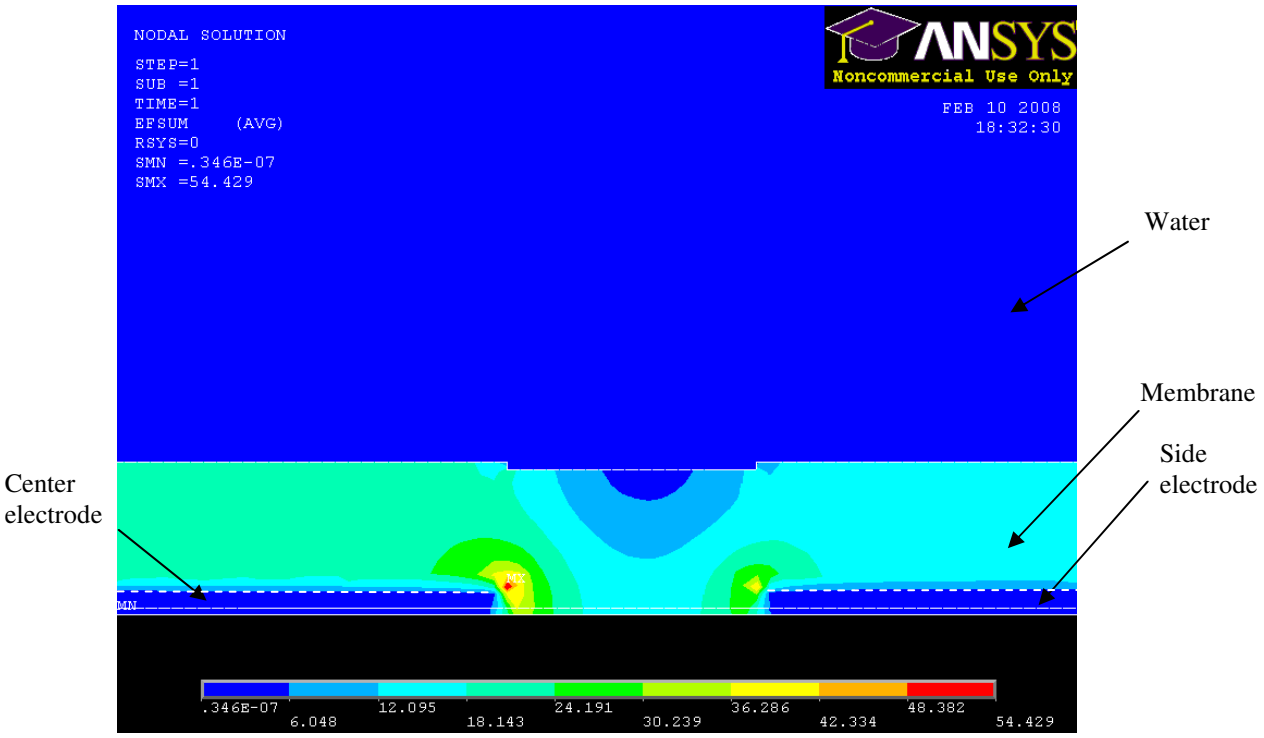

Figure 49 Simulation result showing the electrical field between side and center electrode in water (C_{cross})

As expected, the electrode thickness does not have a significant effect on the electrical isolation as most of the electrical field is due to fringing effects. Decreasing the gap thickness and isolation nitride between top and bottom electrode has a similar increasing effect on the electrical isolation. However as discussed before, the isolation nitride thickness has significantly less effect on the electrical isolation as compared to the gap thickness. Moreover, increasing the distance between side and center electrodes decrease the cross talk capacitance while the receive capacitance remains constant. As a

result, the electrical isolation is increased due to increased distance between conductors. The membrane thickness has an opposite effect on the electrical isolation similar to operating in either oil or water. The electrical isolation is increased for increasing membrane thickness due to membrane silicon nitride having a smaller electrical permittivity (ε_r=6.3) as compared to that of water (ε_r=80) as illustrated in Figure 50. However, note that increasing the membrane thickness alters several design constraints such as operation frequency, collapse voltage, and operation bandwidth.

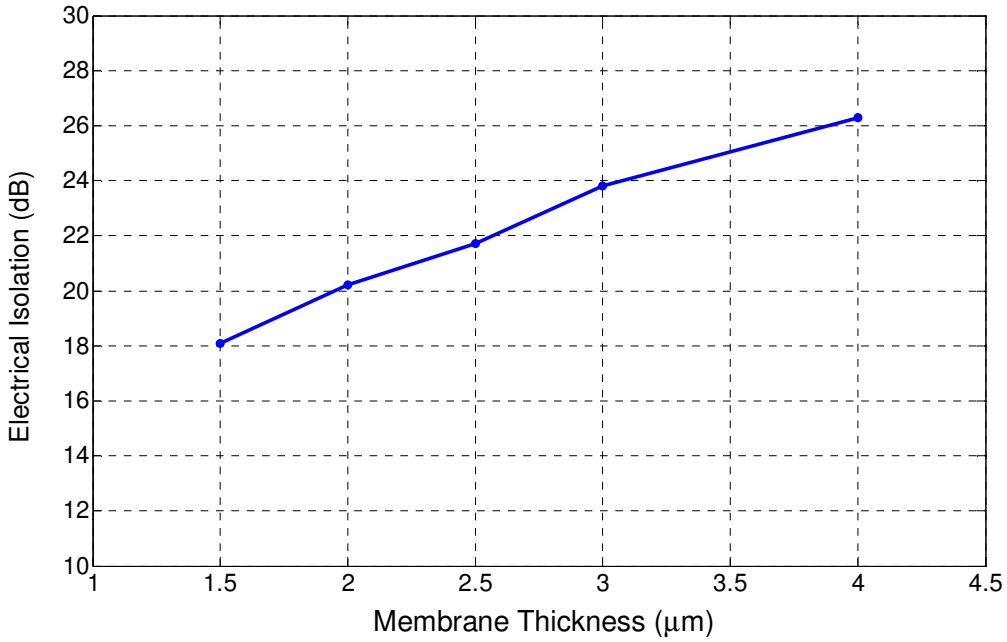

Figure 50 Simulated electrical isolation as a function of membrane thickness for operation in water

4.3.2 Electrical Isolation Improvement Methods

Here we investigate two alternative methods for increasing the electrical isolation between side and center electrodes. The first one is placing notches in between the side and center electrodes in the membrane. The thickness of the notch in the membrane should not exceed 2µm as thicker notches will create fabrication related problems for 3.5µm thick membrane. In addition as notches in the design reduce the frequency response, the membrane thickness is increased to compensate for the drop in the frequency. For the geometry given in Table 9, the membrane thickness is increased to 3.6µm from 3.5µm to match the 8MHz operation frequency. The results for air, oil and water operation is illustrated in Figure 51. In all 3 medium of interest, there are two opposing effects. The first effect is membrane thickness which increases the electrical isolation for water operation while decreasing for air and oil operation. The second effect is the notches in the design which decrease the electrical isolation for water operation while increase for air and oil operation. Overall, the notches in the design do not have a significant effect on the electrical isolation regardless of the medium due to electrical fringing field between side and center electrodes. Especially when the fabrication difficulties associated with notch implementation is considered, notch in the design is not a feasible cross-talk improvement method.

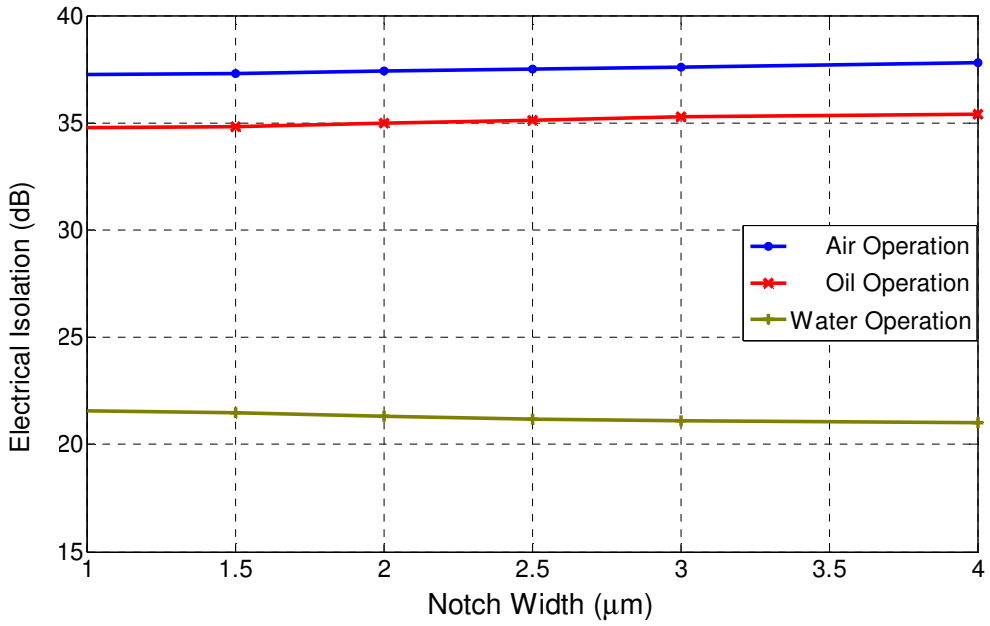

Figure 51 Simulated electrical isolation as a function of notch width for operation in air, oil and water

A second alternative to consider for improving electrical isolation is to deposit a parylene-C layer on the membrane. Parylene-C has low permittivity (ε_r=3) that may decrease the cross talk capacitance between center and side electrodes while not affecting the active receive capacitance. Adding another layer to the membrane changes the frequency response of the membrane hence the silicon nitride layer should be adjusted to compensate for the existence of parylene. With the material properties of parylene, the frequency response of the membrane increases, hence the thickness of the silicon nitride is reduced to 3.1µm from 3.5µm. The effect of parylene on the electrical isolation is illustrated in Figure 52.

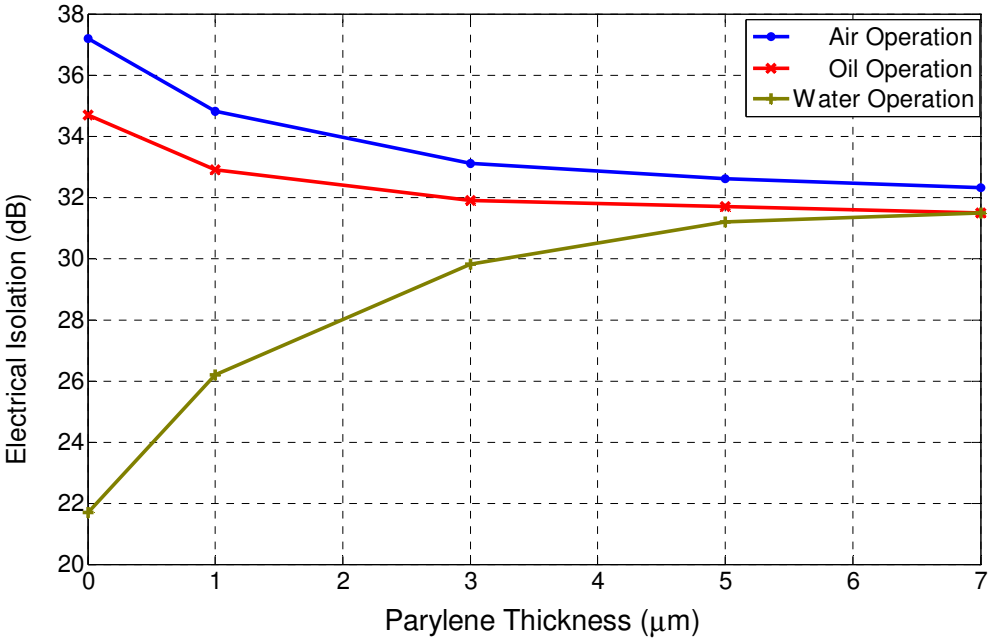

Figure 52 Simulated electrical isolation as a function of parylene thickness for operation in air, oil and water

One can observe from Figure 52 that adding a parylene layer significantly increases the electrical isolation for water operation while adding parylene decreases the electrical isolation for air and oil operation. There are two opposing effects in this case as well: the addition of parylene layer and the reduction of the membrane thickness. As the permittivity of parylene (ε_r=3) is higher than that of air (ε_r=1) and oil (ε_r=2), it actually reduces the electrical isolation. On the other hand for operation in oil and air, thinner membrane thickness yields higher electrical isolation. However, the effect of parylene is far more pronounced than the membrane thickness effect, and as a result, the overall electrical isolation is decreased. Therefore, adding parylene for air and oil operation decreases the electrical isolation and should be avoided as far as cross-talk is concerned. On the other hand, placing parylene on the membrane for water operation is very

advantageous in that it significantly increase the electrical isolation. Note that the cross capacitance is increased from 0.75pF for no parylene to 0.25pF for 6μm of parylene.

4.4 Discussion

In this chapter, membrane parameter optimization studies are explained in detail. It is important to note that, where applicable, the generic optimization studies that are also applicable to conventional CMUTs are undertaken. For instance, membrane width and thickness, electrode thickness, gap height, and silicon nitride isolation thickness optimization studies can directly be used in conventional CMUT design. In these optimization studies, instead of only focusing on transduction performance, several important aspects are investigated. A complete study that quantifies transducer bandwidth, operational frequency, transformer ratio, electromechanical coupling coefficient, output pressure, output sensitivity, and collapse voltage for each variable is presented. In most of these membrane parameter optimizations, there is a trade-off between figures of merit. One can maximize the figure of merit that is of high importance with a reduction of others. For instance, a very high power-transmitter can be designed by increasing the gap and using the side excitation, with a significant reduction in receive performance.

Moreover, membrane shape optimization is also explored. Two approaches are investigated, introducing a notch or a center mass in the membrane. It is observed that notch introduction increases the transduction performance of the dual-electrode CMUT by 3.1dB. On the other hand, when the center mass is introduced to the dual-electrode CMUT design, the transduction performance is increased by 3.6dB while the fractional

bandwidth is increased by 75% and the required maximum operation bias is reduced by 20% (to 132V from 160V). The center mass addition is superior to notch introduction in several ways. First, the bandwidth and required operation bias are unchanged for CMUT membrane with notches while significant reduction in bias and increase in bandwidth are obtained with center mass introduction. Moreover, it is challenging to fabricate CMUT membrane with notches between side and center electrodes. Although the stress analysis does not indicate additional issues with the introduction of notches, there may be reliability problems with long term use. Moreover, it is easier to align 24μm center mass than the 2μm notch.

Detailed electrical isolation of side and center electrode is also explored in this chapter. The effect of membrane parameters to electrical isolation for air-oil-water operation is documented. It is important to note that the deflected membrane when actuated at the optimized side and center bias value is inserted into the FEA as initial condition. Hence, the electrical isolation is reduced if the CMUT is operated with non-optimized side and center electrode bias values. Moreover, these analyses neglect the effect of electrical cross-talk sources other than the side and center electrode separation in the membrane such as cross-talk resulting from front-end electronics.

CHAPTER 5

FABRICATION OF DUAL-ELECTRODE CMUTS

The fabrication of dual-electrode CMUTs are based on process developed by the Degertekin group based on the available equipment at the Microelectronics Research Center (MiRC), Georgia Institute of Technology [38]. However, there are several adjustments and modifications to existing process flow that increase the performance and reliability of the fabrication. This surface micromachining process uses PECVD (Plasma Enhanced Chemical Vapor Deposition) nitride deposition at 250^{o}C for membrane formation and cavity sealing and chromium as the sacrificial layer. Fabrication of dual-electrode CMUT architecture is not more involved than conventional CMUTs. In fact, as dual-electrode CMUTs can be fabricated with only changing the top electrode mask, there is no any additional steps in the fabrication process for dual-electrode implementation. The maximum process temperature of 250^{o}C enables fabrication of CMUTs directly on top of CMOS electronics chip. This maximizes the area usage and increase the transducer performance by minimizing the parasitic capacitance. Successful CMUT-on-CMOS implementation is fabricated and demonstration studies will be summarized in this chapter.

5.1 CMUT Fabrication Process

The dual-electrode CMUT is essentially a silicon nitride compliant membrane suspended above a vacuum gap. There is a buried top electrode in the membrane that allows electrostatic actuation and sensing. The fabrication process flow is illustrated in Figure 53. The steps as marked on Figure 53 are (1) Substrate-Bottom electrode isolation deposition, (2) Bottom electrode formation, (3) Bottom electrode isolation formation (4) Sacrificial layer formation, (5) Top electrode isolation formation, (6) Top electrode formation, (7) Membrane deposition (8) Membrane release and (9) Membrane sealing. Each of these steps will be described in the following sections.

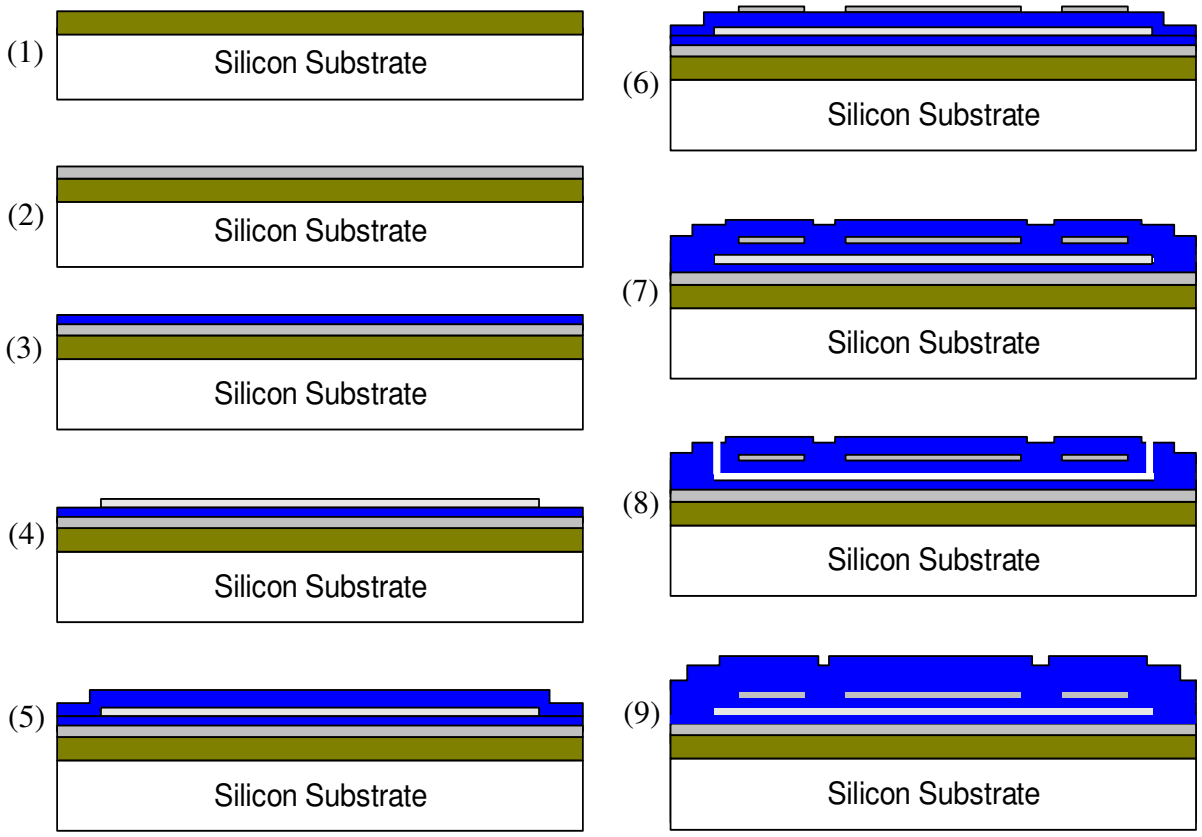

Figure 53 Illustration of fabrication process flow for low temperature, CMOS compatible dual-electrode CMUTs

5.1.1 Substrate-Bottom Electrode Isolation Deposition

As a first step in CMUT fabrication, the isolation layer between the bottom electrode and the silicon substrate is deposited. By placing a low permittivity dielectric material such as silicon oxide (ε_r=3.9) or silicon nitride (ε_r=6.7) between bottom electrode and substrate, the parasitic capacitance is reduced as the silicon substrate acts like a conductive plane. This isolation thickness should be maximized for better isolation while keeping surface roughness to a minimum. In the fabricated devices, 2μm silicon oxide isolation is used. The silicon oxide deposition is done in a PECVD station with a deposition temperature of 250^{o}C. Silicon oxide is preferred over silicon nitride as its permittivity is lower and the oxide deposition rate is 8 times faster than nitride deposition rate. Moreover, the CMOS chip that will be used in the CMUT-on-CMOS implementation should be isolated from the fabricated CMUT. This layer also isolates CMOS substrate from CMUT.

5.1.2 Bottom Electrode formation

The parasitic capacitance is significantly reduced by employing a separate bottom electrode rather than using silicon substrate as a bottom electrode in the design. The reason for parasitic capacitance reduction from a separate bottom electrode is because the overlapping signal traces are eliminated and the sole source of parasitic capacitance comes from the fringing capacitance. The bottom electrode is formed by sputtering 100nm of Aluminum in DC sputtering station. After the deposition, the electrode is patterned using a photoresist mask with wet aluminum etchants (Figure 54). The bottom

electrode covers the entire array (6.4mm by 2.4mm). Two bondpad connections to the bottom electrode are implemented in case one electrically fails.

Figure 54 Mask image of bottom electrode that covers the whole array

5.1.3 Bottom Electrode Isolation Deposition

In this step of the fabrication, silicon nitride isolation is deposited in the low temperature (250^{o}C) PECVD station to protect the bottom electrode during the release step. While the sacrificial chromium layer is etched in the release step, the aluminum bottom electrode, if not protected, is etched as well. It is important to note that this nitride thickness should be minimized as much as possible while protecting the bottom electrode as this nitride layer forms a capacitance in series with the gap capacitance. This reduces the sensitivity and increase the collapse voltage significantly. One important aspect is that this CMOS compatible PECVD process causes pinhole formation during deposition. From the pinholes the sacrificial chromium etchant can seep through and etch the bottom electrode regardless of the isolation nitride thickness. To avoid this phenomenon, wafers are rotated twice during the deposition process. This method gives a reliable isolation between sacrificial layer and bottom electrode. Devices with isolation nitride thickness as small as 250nm is successfully fabricated and tested.

5.1.4 Sacrificial Layer Formation

The sacrificial layer is used to form the gap that separates the membrane from the substrate. The sacrificial layer is formed by sputtering 120nm of chromium in the DC sputtering station. The chromium has low roughness and wet chromium etchant is highly selective to silicon nitride. After the deposition, the sacrificial layer is patterned using a photoresist mask and etched using chromium etchant (Figure 55). After the patterning of the chromium, the wafer should be cleaned 5 minutes by dipping into acetone, methanol and isoproponal alchohol (IPA) bath in a sonicator to eliminate any residue on the sacrificial layer. One can observe from Figure 55 that the sacrificial layer for each membrane is placed in such a way to increase the fill factor (ratio of active membrane area to total array area). As a result, the etch holes used to release the sacrificial layer are placed at the four corners of the membrane. As summarized in Table 9, each membrane is 48μm by 100μm; one array element is comprized of 48 membrane in series.

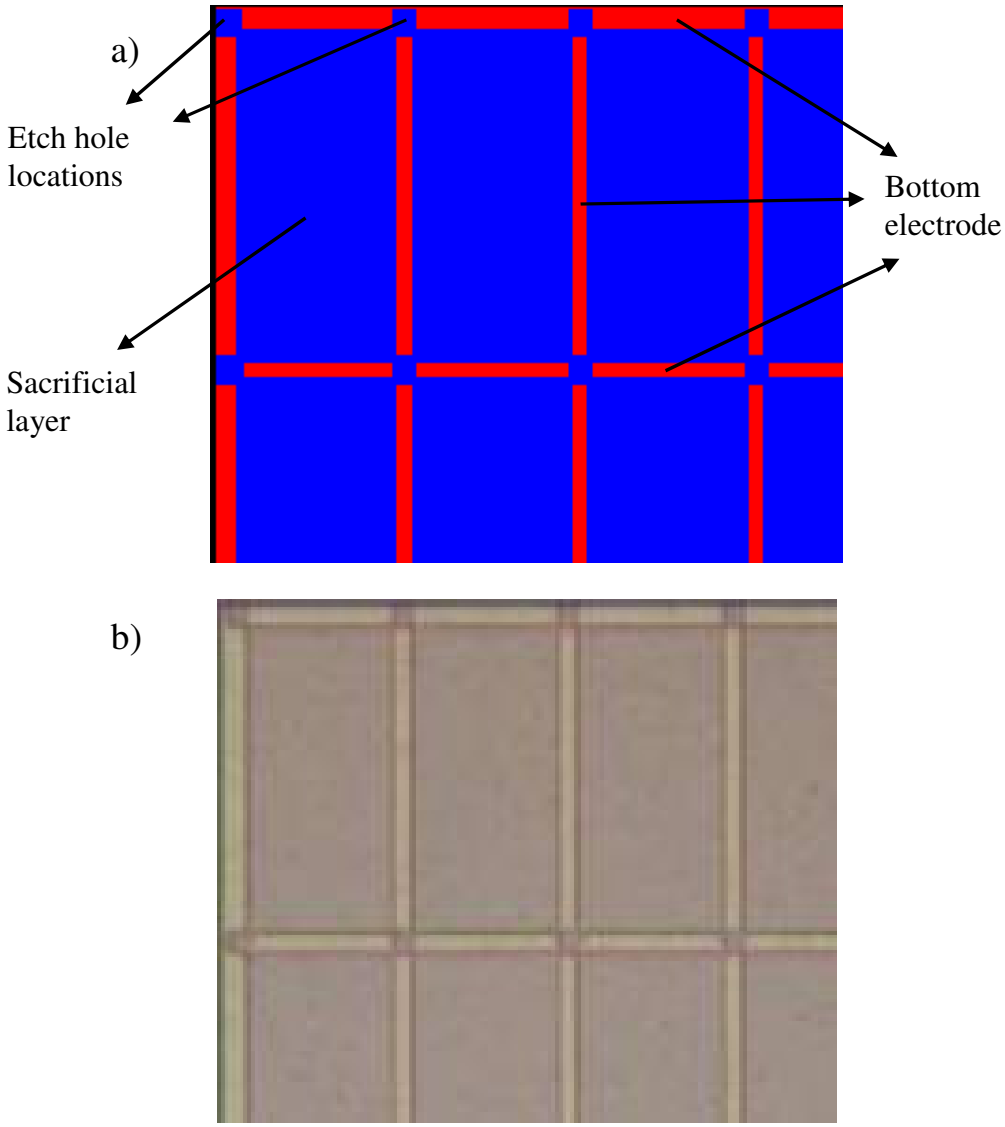

Figure 55 a) Mask image and b) picture of patterned sacrificial layer

5.1.5 Top Electrode Isolation Deposition

In this step of the fabrication, PECVD silicon nitride isolation is deposited to protect the top electrode during the release step. Just like the bottom electrode, the top electrode is also made of aluminum; it is etched by chromium etchant during the release step if not protected. This nitride thickness should also be minimized while protecting the top electrode as this nitride isolation layer forms a series capacitance with the device

capacitance. Wafers are rotated twice during the deposition process to prevent pinhole formation. Devices with top electrode isolation nitride thickness as small as 250nm is successfully fabricated and tested.

5.1.6 Top Electrode Formation

The top electrode is formed by sputtering 100nm of Aluminum in a DC sputtering station. After the deposition, the electrode is patterned using a photo-resist mask and etched by using commercially available aluminum wet etchant (Figure 56). The respective center and side electrodes are electrically connected in series for 48 membranes as shown in Figure 56. Each column has 24 membranes and 2 columns are connected to obtain a single element for the dual-electrode CMUT array.

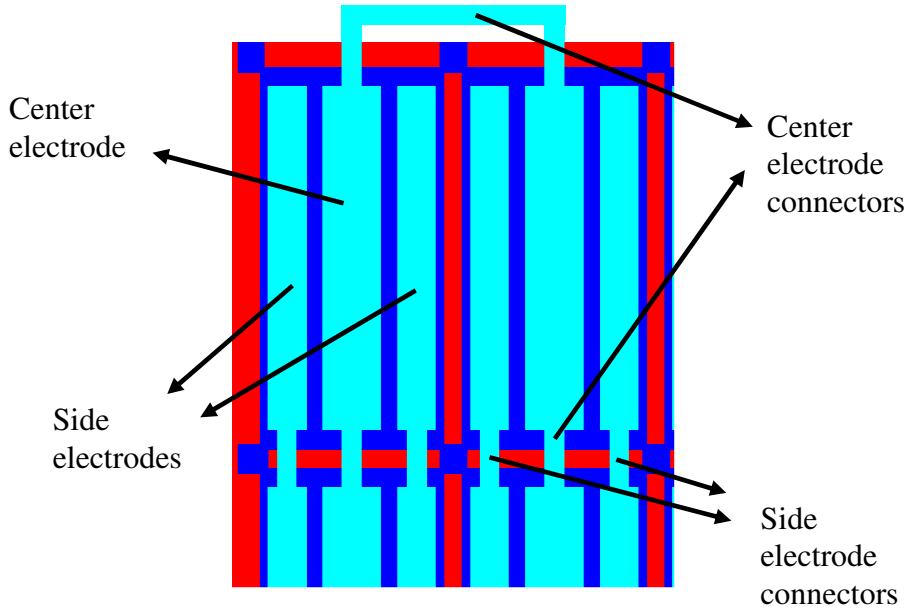

Figure 56 Mask image of patterned top electrodes

5.1.7 Membrane Deposition

In this step of the fabrication, additional PECVD silicon nitride is deposition to increase the membrane thickness and to protect the top electrode from chromium etchant during the release step. The minimum thickness of silicon nitride should be 250nm for protection of the top electrode. The wafers are rotated halfway through the deposition step to reduce the pinhole formation.

5.1.8 Membrane Release

To form the gap, four etch holes are placed along each corner of the membrane. As explained previously, the sacrificial layer has extensions where the etch holes for release are aligned to (Figure 57). As shown in Figure 57, the etch holes are aligned to these extensions. This mask alignment is the most critical step in the fabrication. First, the diameter of etch hole is 4μm. The convention is to use positive photo-resist for such a small feature size as feature definition is better with positive photo-resists. However, the mask has only 4μm clear fields and rest of the mask is dark. Hence, one needs to do alignment by only using the alignment marks as physical alignment of etch holes are not possible. After the alignment, the silicon nitride is etched with a anisotropic Reactive Ion Etch (RIE) tool. The chromium acts as a etch stop for silicon nitride etch in the RIE. Slight misalignment of the etch holes causes the RIE to etch the bottom electrode isolation nitride and the bottom electrodes are then attacked during the release step. After etch holes are formed, the wafers are kept in chromium etchant for approximately 12 hours to form the gap. Stiction between the top and bottom isolation is one problem that may arise, but can be avoided by soaking the wafer in IPA for 5 minutes immediately

followed by an oven bake at 95C. The IPA has low surface tension and helps fabricate released membranes.

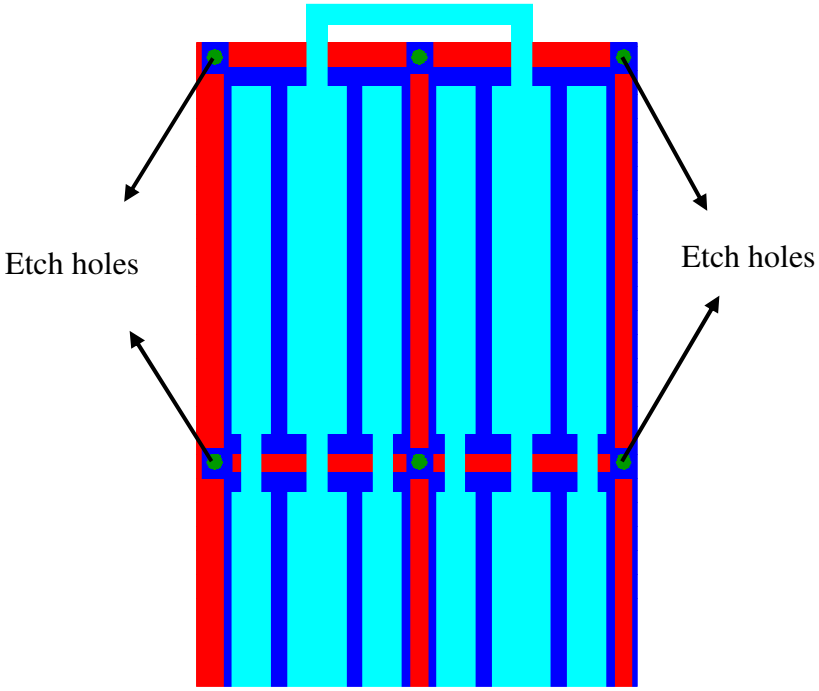

Figure 57 Mask image of etch holes used for releasing the membrane

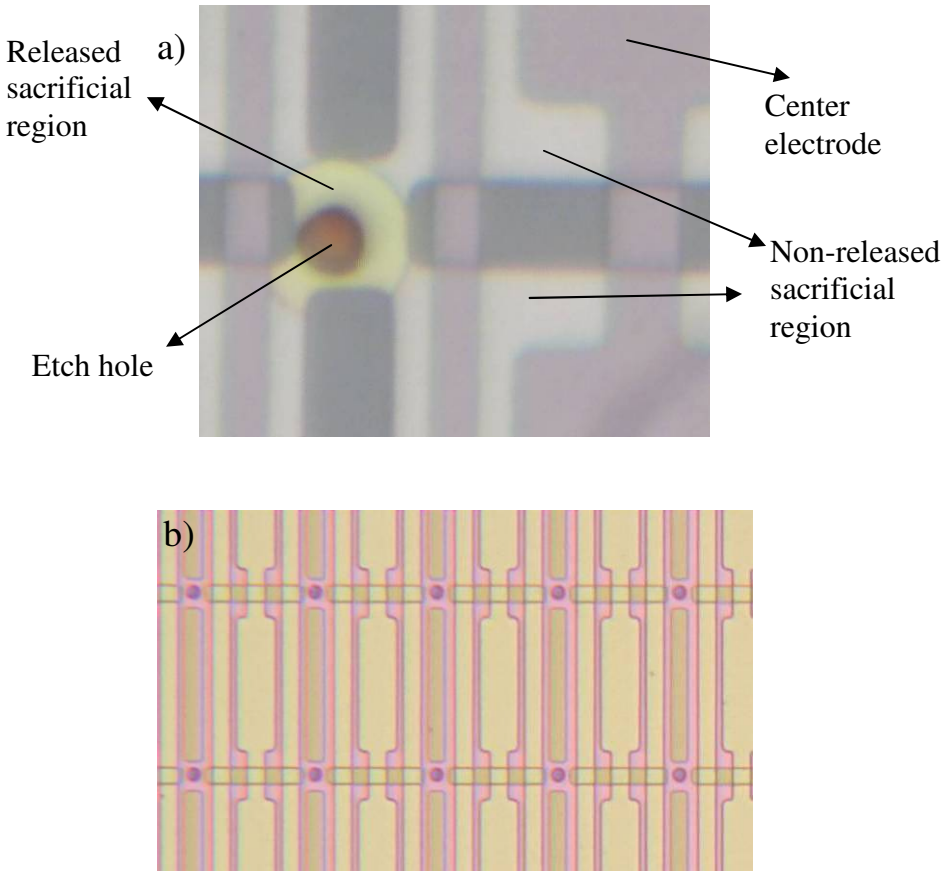

Figure 58 Illustration of etching during release step: a) after 20 minutes in the chromium etchant, b) completed membrane release

5.1.9 Membrane Sealing

The membrane is sealed for immersion applications by depositing an additional layer of silicon nitride in the PECVD station. Moreover, more nitride should be deposited to increase the membrane thickness to its design thickness, 3.5µm.

5.1.10 Bond Pad Etch

During the silicon nitride deposition for membrane formation, bondpads are also covered with silicon nitride. In the final step of the fabrication, the silicon nitride on the bondpads is etched in the RIE chamber. Over-etching creates problems such as burning of the aluminum bondpads which makes wirebonding difficult. The photo-resist mask is used to protect the membranes from being thinning down. A completed test dual-electrode CMUT array with 16 elements is illustrated in Figure 59.

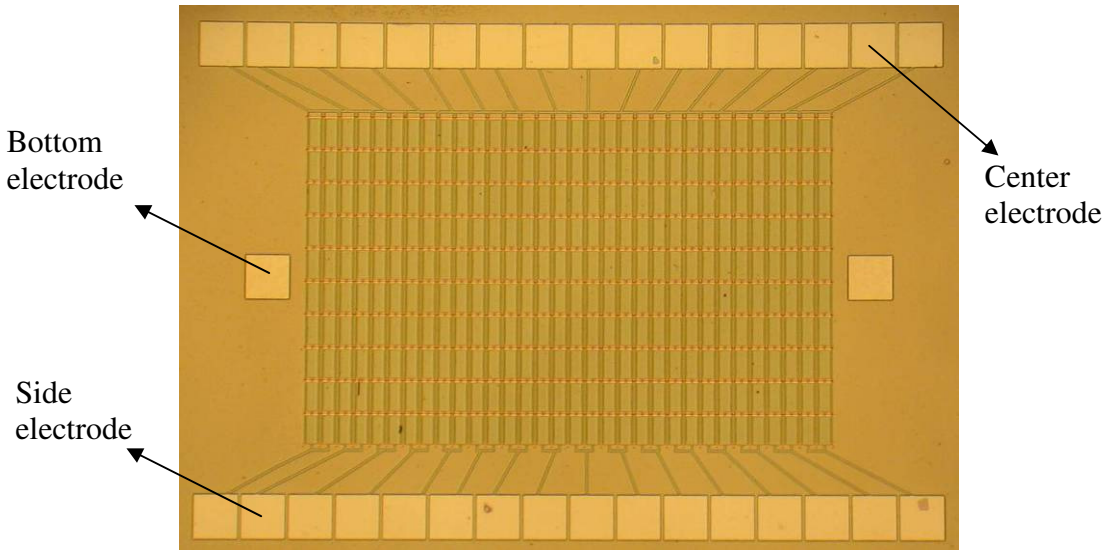

Figure 59 Picture of a fabricated dual-electrode CMUT test array with 16 elements

5.1.11 Optional Step: Non-Uniform Membrane Formation

For non-uniform membrane formation, additional silicon nitride is deposited for the thickest membrane feature. After this deposition, a mask is used to protect the center mass region of the membrane and remaining membrane region is etched down to the designed membrane thickness. It is important to note that this etching step should be done

before etching the nitride over the bondpads as unprotected bondpads will be exposed to RIE etch which roughens the surface and makes it harder to wirebond for electrical connections. Alternatively, the bondpad openings can be protected by the same mask which protects the center mass region and the non-uniform membrane formation can be done as the final step of the fabrication. A Scanning Electron Microscope (SEM) image of completed non-uniform membrane is illustrated in Figure 60.

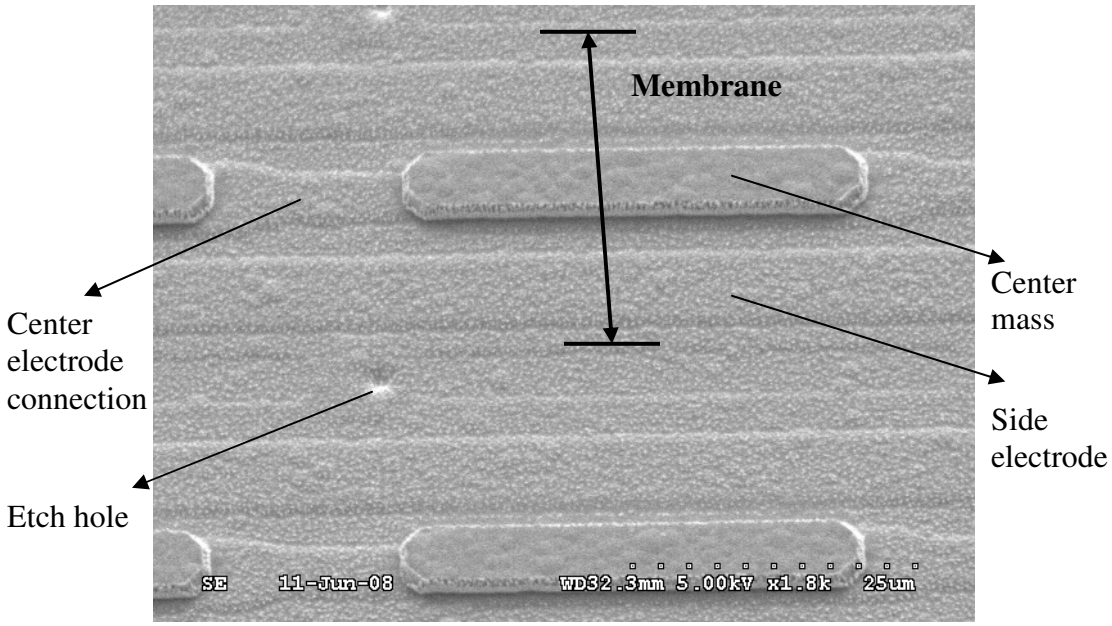

Figure 60 SEM image of a completed non-uniform membrane dual-electrode CMUT

5.1.12 Parylene Deposition

After the fabrication and wirebonding to PCB, the samples are coated with parylene-C layer for electrical isolation. The parylene deposition is carried out in PDS 2010 Lab-coater 2 (Specialty Coating Systems, Indianapolis, IN). Parylene isolation is necessary for experiments conducted in conductive media such as water. The exposed bond wires and bond pads can cause electrical shorting. Typical parylene-C layer

thickness of 3µm is chosen for sufficient electrical isolation. Note that deposited parylene layer on the membrane affects the membrane dynamics and this effect can be included in the simulation studies

5.1.13 Process Recipes

The silicon nitride and silicon nitride is deposited in the Unaxis 790 (Plasma Therm Inc., St. Petersburg, FL) – PECVD system and the deposition process parameters are summarized in Table 13. In the silicon nitride deposition, the original recipe from Unaxis uses 1100mTorr and 60W power; however, to increase the quality of nitride (decrease the porosity), both pressure and power is reduced while keeping the residual stress in the membrane to a minimum. The wafer bow technique is used to measure the residual stress in the membrane using a Veeco Dektak 3030 profilometer. Low tensile residual stress of 25MPa is measured in the nitride layer with the parameters given in Table 13.

Table 13 Recipes for silicon nitride and oxide deposition in the Unaxis PECVD

Parameter	Silicon Nitride	Silicon Oxide
5% SiH_4	200 sccm	400 sccm
NH_3	8 sccm	-
He	560 sccm	-
N_2	150 sccm	-
N_2O	-	900 sccm
Pressure	900 mTorr	900 mTorr
Power	45 W	25 W
Temperature	250^oC	250^oC
Deposition Rate	7.5 nm/min	60 nm/min

The etching of the silicon nitride in various stages of fabrication is done by the Vision Oxide RIE (Advanced Vacuum, Lomma, Sweden). The process parameters are listed in Table 14. The RIE etch process for silicon nitride has a selectivity of approximately 1:1.

Table 14 Recipes for reactive ion etch of silicon nitride

Parameter	Silicon Nitride
Ar	20 sccm
CHF3	40 sccm
O2	6 sccm
Pressure	12 mTorr
Power	350 W
Etch Rate	65 nm/min

5.2 CMUT-on-CMOS Implementation

One of the most important promises of capacitive micromachined ultrasonic transducer (CMUT) is integration with electronics (Figure 61). This monolithic integration approach maximizes transducer sensitivity by minimizing parasitic capacitances and ultimately improves the signal to noise ratio [69]. Additionally, due to physical size limitations required for catheter based imaging devices, optimization of area occurs when the CMUTs are fabricated directly above the associated electronics.

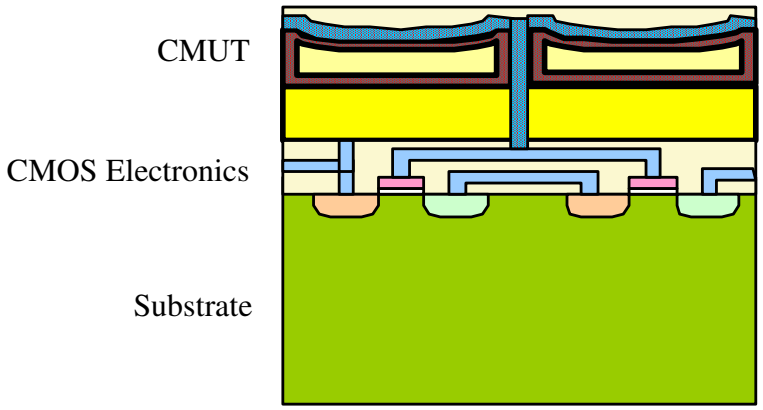

Figure 61 Schematic of CMUT-on-CMOS implementation

Our fabrication process that uses maximum process temperature of 250^{o}C can be used to fabricate CMUTs directly on top of custom designed CMOS electronics. To fabricate CMUTs on CMOS, we modified our low temperature process developed to implement functional interconnects between CMUT array elements and receive electronics on the same chip while introducing few additional steps. We designed linear test arrays to evaluate the integration possibility. Prefabricated and diced CMOS wafer pieces are first coated with 2μm of insulating silicon oxide via plasma enhanced chemical vapor deposition (PECVD). Etch holes are then defined via a clear field mask and negative photo-resist, 2.7μm NR7-1500P, for ease and verification of alignment. The

substrate is then processed with a reactive ion etch optimized to yield sloped sidewalls. With this configuration, the same metal layer that forms the bottom electrode of the CMUT, 120nm aluminum, establishes reliable electrical contact through the insulation as illustrated in Figure 62.

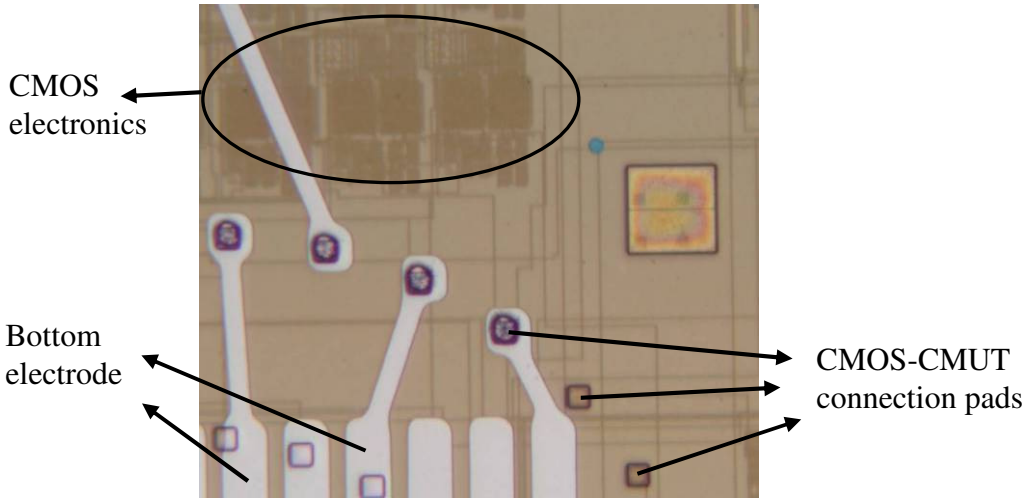

Figure 62 Close-up picture of fabricated test arrays on CMOS electronics

The front-end CMOS electronics (Transimpedance type amplifier) are tested before and after CMUT fabrication to investigate post fabrication effects and interconnect quality. The results show that the gain and frequency response of the amplifiers are not altered by the post-fabrication process. We wirebonded and placed test arrays which have both receive and transmit elements in an oil bath (Figure 63). Pulse-echo experiments are successfully conducted by transmitting with the on chip transmit element and receiving the echo from aluminum block with the receive CMUT element connected to the CMOS electronics. This test array is operating in the 2-6MHz range and the amplifiers, multiplexer and buffers on the same chip are used for pulse-echo operation [70]. The received pulse-echo signal is illustrated in Figure 64. The signal to noise ratio (SNR) of

received signal is 28dB which is suitable for real time IVUS and ICE applications. In the tests, 20V DC bias is applied to both transmit and receive elements and 10V pulse is applied to each transmit element.

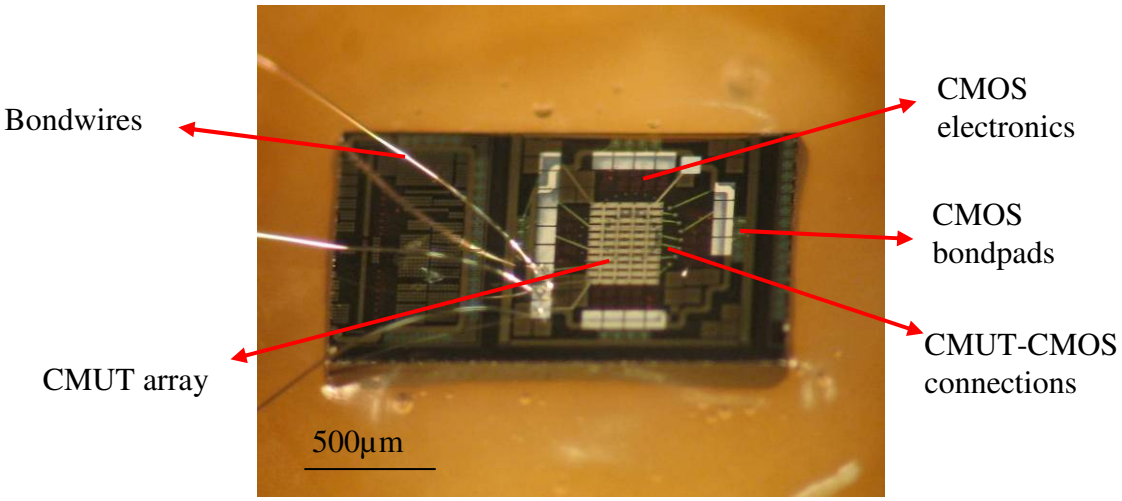

Figure 63 Picture of a wirebonded CMUT on CMOS test array used in pulse-echo experiments

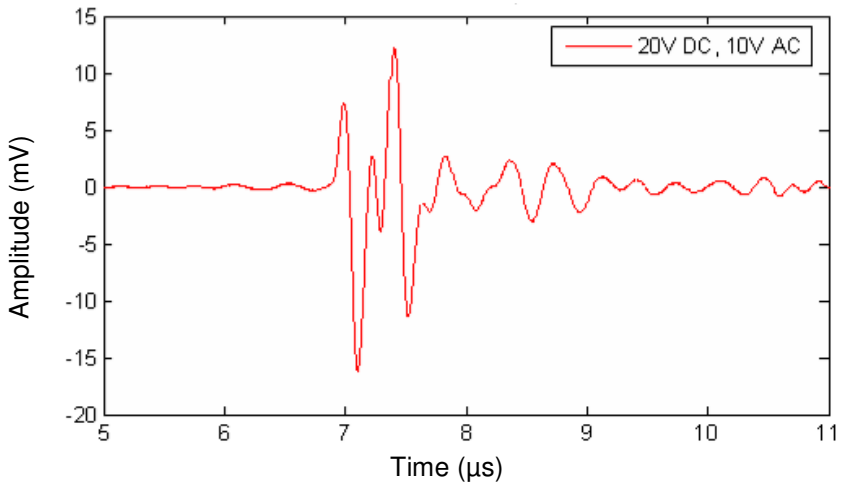

Figure 64 Experimental pulse-echo response from a fabricated CMUT on CMOS test array

5.3 Discussion

In this chapter, first we discussed each fabrication process step in detail. This CMOS compatible low temperature fabrication process uses only three microelectronic processing tools which are commonly available in most microfabrication facilities; namely: a PECVD station for membrane deposition, a RIE system for directional silicon nitride etch and a DC metal sputtering station for the electrodes. During fabrication, it is observed that using separate containers for each etchant, purging the DI water line before rinsing the wafer, rotating the wafer halfway through PECVD nitride deposition increase the reliability of the fabrication. For the CMUTs fabricated on a substrate, 4 inch circular silicon wafer is used as a substrate. On a single 4 inch wafer, more than 100 imaging arrays can fit. This brings the cost of each imaging array down significantly. The CMUT-on-CMOS implementation is successfully fabricated and tested. This initial demonstration is made possible by designing an entire set of masks for linear test arrays.

CHAPTER 6

EXPERIMENTAL RESULTS AND MODEL VERIFICATION

In this chapter, the performance improvements predicted by finite element simulations are verified by experimental results. First, both uniform and non uniform membrane dual-electrode characterization results are summarized. Receive only experiments are performed to measure receiver performance improvement and to determine the optimal operating points for both non-uniform and uniform membrane dual-electrode CMUTs. Moreover, the electromechanical coupling coefficient (k_c^2) for both uniform and non-uniform membrane CMUTs are obtained via capacitance measurement. In addition, absolute net output pressure generated by the dual-electrode CMUTs is measured using a calibrated hydrophone as a receiver, and relative transmit performance increase estimates are verified [71]. Simulations indicated significant bandwidth increase with center mass addition. This result is verified by obtaining the frequency response of a transmitted pulse by a non-uniform membrane dual CMUT via calibrated hydrophone. Moreover, dual-electrode and conventional CMUT comparison is done on tissue-mimicking phantoms. Finally, the pulse-echo experiments with dynamic biasing applied to side electrodes are conducted to illustrate the possibility of real-time imaging with dual-electrode CMUTs.

6.1 Characterization of Dual-Electrode CMUTs

6.1.1 Receive Sensitivity Measurements

For receive mode characterization of the uniform membrane dual-electrode CMUT, the setup shown in Figure 65 is used. The CMUT array is placed 3mm away from a piezoelectric transmitter (IS2002HR, Valpey Fischer Corp., Hopkinton, MA) which is excited with a 10 cycle tone burst at 10 MHz, which is in the design bandwidth of the ICE array element. The center electrode of the CMUT is the receive terminal and it is connected to the input of a low noise trans-impedance amplifier (TIA) (AD8015, Analog Devices, MA, USA), which electrically terminates the device with a virtual short circuit, removing the effects of termination impedance from the measured characteristics [32]. TIA configuration is commonly used for CMUT receiver electronics [46, 70].

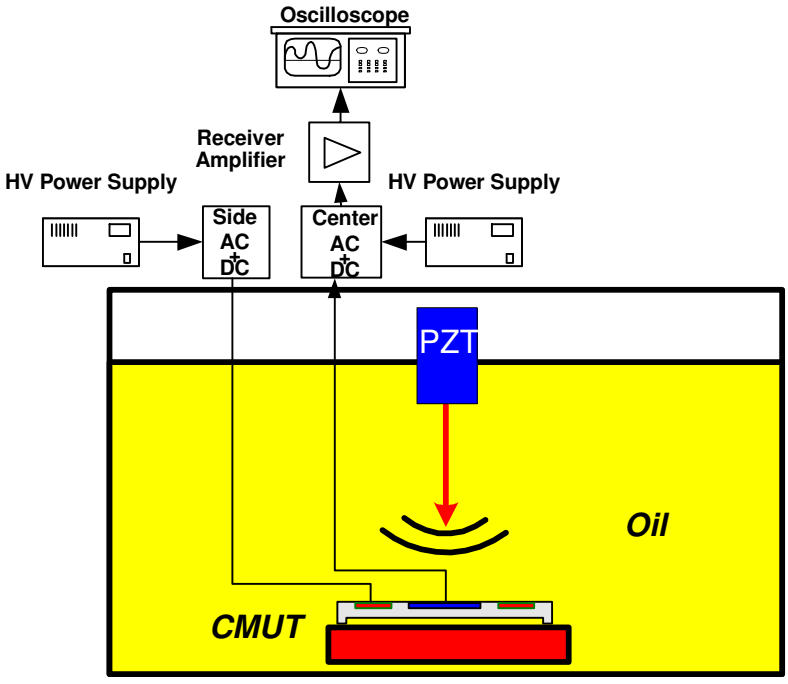

Figure 65 Experimental setup used for dual-electrode CMUT receive mode experiments

Received signal amplitude is then measured while varying center and side DC bias levels. The results are plotted in Figure 66 (a). Conventionally, CMUTs with no side electrodes are operated close to the collapse voltage to maximize receive signal, indicated by point A (V_{center} = 115V, V_{side} = 0V) in Figure 66 (a). On the other hand, the dual-electrode CMUT is biased to point B (V_{center} = 80V, V_{side} = 160V), to achieve maximum sensitivity during receive. One can see that the received signal amplitude is increased from 1.7V (point A) to 5.3V (point B). As a result, membrane shaping by using the side electrodes increase the receive sensitivity by 10dB (3.2×) at 10MHz for this particular dual-electrode CMUT device. The important operational points that will be used throughout this chapter are summarized in Table 15.

As shown in Figure 66 (b), the finite element simulation of the transformer ratio agrees well with the measured results, confirming that this ratio is a valid figure of merit for evaluating the performance of CMUTs in receive mode of operation. It can be observed from Figure 66 (a) and that the data is divided into two distinct regimes, namely, the collapse and contact regions. In the collapse region (side electrode voltage: $V_{side} \leq 160V$) there is a certain center electrode voltage (V_{center}) which causes pull-in instability and collapse, whereas in the contact region ($V_{side} \geq 160V$) there is no such V_{center} value, the membrane simply touches the bottom dielectric layer without going through an unstable collapse. Even though spurious effects such as charging and fabrication non uniformities are not simulated, occurrence of collapse-contact region, the relative variation of transformer ratio with conventional and dual-electrode CMUTs are very well captured by the FEA results of Figure 66 (b).

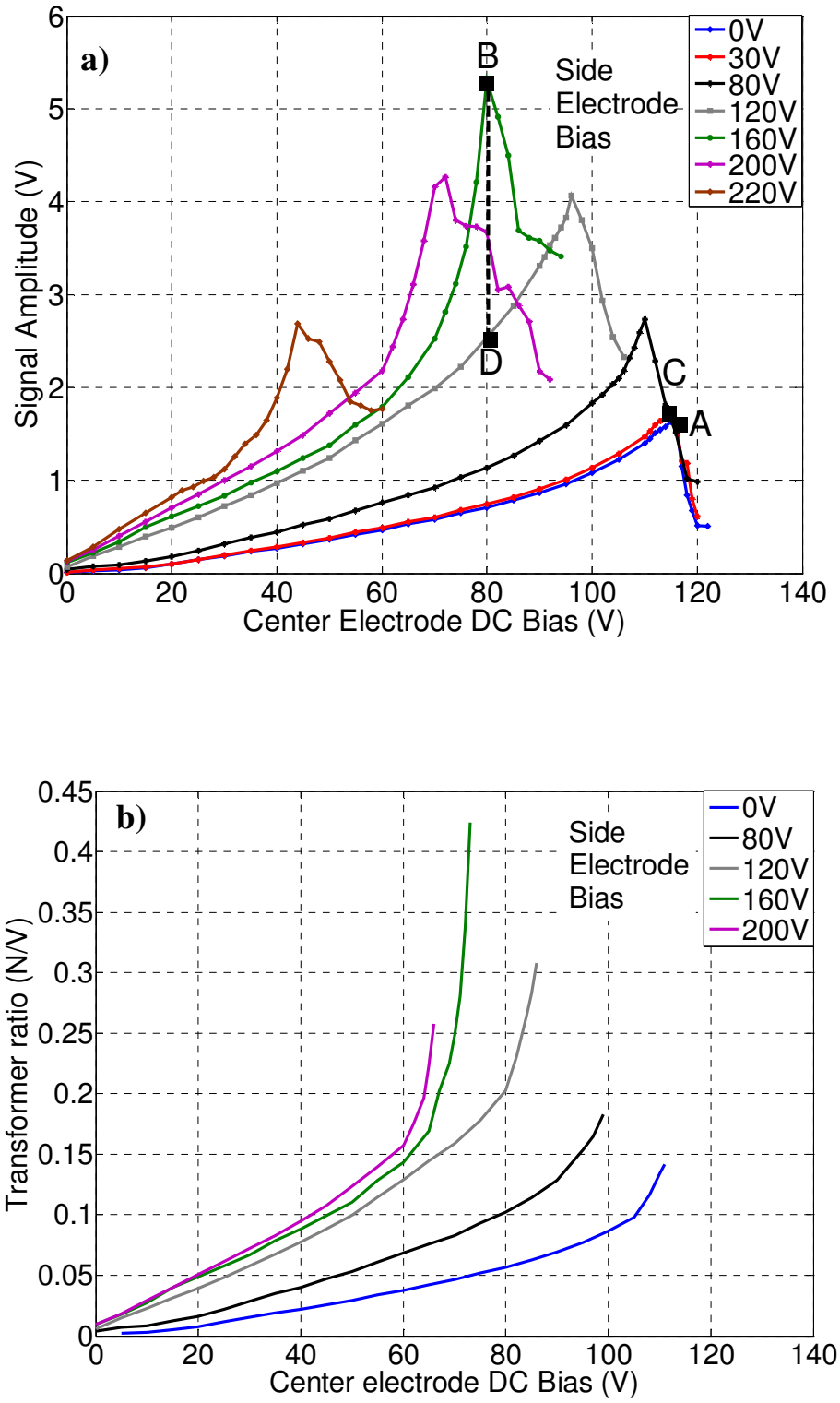

Figure 66 a) Experimental received signal amplitude versus center electrode bias voltage for different side bias voltages. b) Simulated transformer ratio as a function of center and side electrode DC bias values.

Table 15 Summary of important operational points for conventional and dual-electrode CMUTs (obtained from Figure 66 (a))

	Center Electrode Bias (V)	Side Electrode Bias (V)	Signal Amplitude (V)
Point A	116	0	1.66
Point B	80	160	5.3
Point C	115	30	1.72
Point D	80	120	2.4

6.1.2 Electromechanical Coupling Coefficient Measurement

The electromechanical coupling coefficient (k_c^2) can be experimentally measured by recording the capacitance as a function of applied bias. To obtain the capacitance information, electrical impedance of the CMUT is measured by using the set-up illustrated in Figure 67.

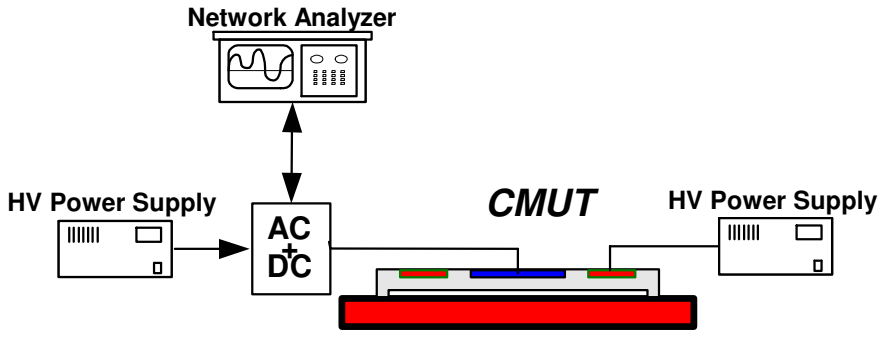

Figure 67 Schematic of setup used for capacitance measurement by network analyzer

The network analyzer (Agilent 8753 ES) measures the electrical reflection coefficient and converts it to complex electrical impedance. The network analyzer performs a frequency sweep over a specified interval. In this experiment, the measurement is taken between 2MHz and 25MHz. The first resonant frequency of the dual-electrode CMUT is found to be 15MHz in air and the off-resonance imaginary impedance value at 25MHz is used to obtain capacitance of the CMUT for a given bias. This experiment is repeated while sweeping the bias voltage. To demonstrate the independent effect of non-uniform membrane and dual-electrode implementation, the data is recorded for both uniform and non-uniform membrane dual-electrode CMUTs. (uniform membrane dual-electrode CMUT with membrane parameters given in Table 9 and non-uniform dual-electrode CMUT with optimized center mass parameters obtained in chapter 4 (Table 16)). For both uniform and non-uniform membrane dual-electrode CMUTs, the capacitance as a function of applied bias curves are obtained for side and center electrodes. The experiments done with center electrode only are essentially conventional CMUT experiments as the advantage of side electrode presence is not employed.

Table 16 Optimized membrane parameters used in the non-uniform membrane dual-electrode CMUT experiments

Membrane Width/Thickness	48µm/2.75µm
Center Mass Width /Thickness	24µm/1.5µm
Gap/isolation thickness	0.12µm/0.25µm
Center/side electrode sizes	15µm/10µm

Measured capacitance as a function of the applied bias for uniform/non-uniform membrane conventional and dual-electrode CMUTs are illustrated in Figure 68. The optimum side electrode bias values during the uniform and non-uniform membrane dual-electrode CMUT experiments are found to be 160V and 132V respectively. These experimental optimum side electrode bias values matches very well with simulation results summarized in Table 12.

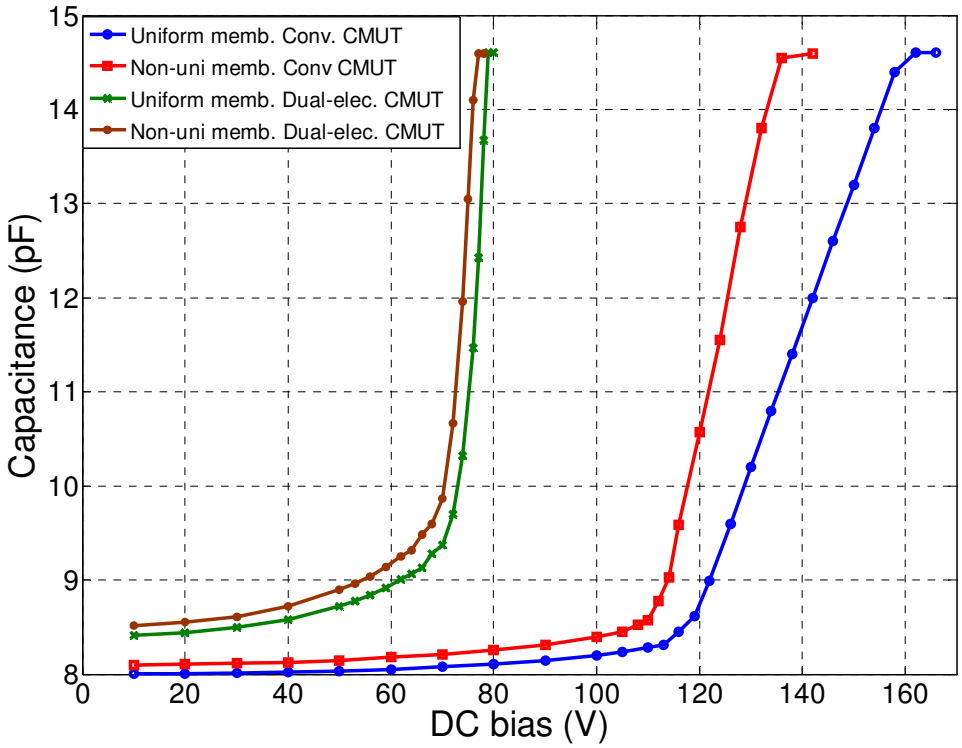

Figure 68 Experimentally measured capacitance as a function of applied DC bias for uniform/non-uniform membrane conventional and dual-electrode CMUTs

We observe from Figure 68 that the slope of the capacitance-bias curve (rate of change of capacitance with applied bias) increases with center mass introduction to the both conventional and dual-electrode CMUT designs. Moreover, the slope of the capacitance-bias curve is increased significantly with dual-electrode CMUT as compared to its conventional counterpart. The dual-electrode CMUT experiments with bias applied

to side electrodes start with higher initial capacitance values than with no center electrode bias as the membrane is initially deflected by the presence of side electrode bias. Moreover, the non-uniform membrane implementation for both dual-electrode and conventional CMUT has a higher initial capacitance. This reason for such a behavior can be explained by simulating the effect of atmospheric pressure on the uniform and non-uniform membrane. Simulations indicate that the initial deflection of the non-uniform membrane is higher than its uniform counterpart. This explains the higher initial capacitance value with the non-uniform membrane. One important consideration is how to define the onset of collapse phenomenon. For instance, the uniform membrane conventional CMUT transitions from non-contact to collapse regime from 120V to 160V. To define the collapse voltage, two conventions are used. First method is obtaining the collapse voltage via finite element analysis. The capacitance value as a function of bias in the non-contact region is used to verify and calibrate the accuracy of finite element analysis. Second method is obtaining the electromechanical coupling coefficient (k_c^2) as a function of applied bias. The electromechanical coupling coefficient (k_c^2) reaches a maximum finite value at the onset of the collapse region [17]. The electromechanical coupling coefficient (k_c^2) is calculated by using the experimentally measured capacitance as a function of voltage. To obtain the electromechanical coupling coefficient, the fixed and free capacitances are calculated by using equations (34) and (35) respectively. The fixed capacitance can be obtained directly from the experimental capacitance-voltage curve. To obtain the free capacitance value, a 6th degree polynomial is fitted to the experimental data. The polynomial is fitted in several voltage intervals to increase the accuracy of derivative calculation for free capacitance. By using the fixed and free

capacitance, the electromechanical coupling coefficient (k_c^2) is obtained by using equation (33). The resulting electromechanical coupling coefficient (k_c^2) as a function of applied bias is illustrated in Figure 69. One can observe from Figure 69 that for all uniform/non-uniform dual-electrode and conventional CMUT cases, a finite maximum electromechanical coupling is obtained. The bias value that results in the highest electromechanical coupling coefficient is the collapse voltage. Figure 69 indicates that the collapse voltages are 112V and 122V for non-uniform and uniform conventional CMUTs respectively while it is 74V and 76V for non-uniform and uniform membrane dual-electrode CMUTs. These results match very well with the results obtained with finite element modeling. This illustrates the accuracy of our developed finite element modeling.

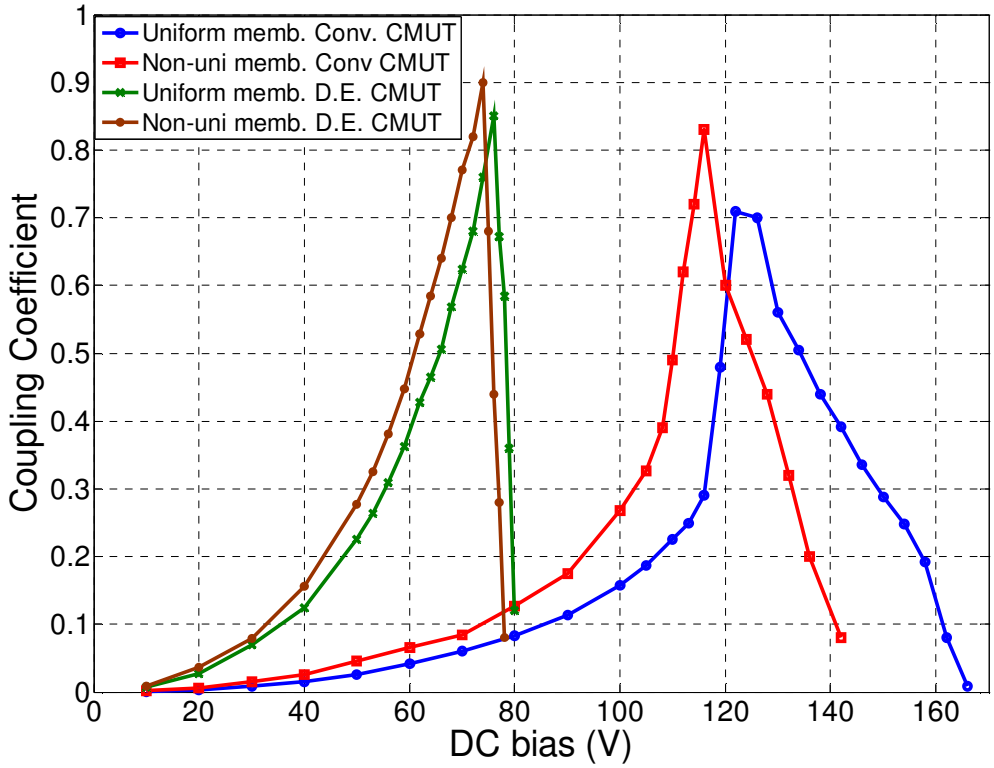

Figure 69 Calculated electromechanical coupling coefficient from experimentally measured capacitance as a function of applied DC bias

We observe from Figure 69 that at any given bias value, the dual-electrode structure achieves a much higher electromechanical coupling coefficient as compared to conventional CMUTs. Although less pronounced, the non-uniform membrane increase the electromechanical coupling coefficient for both dual-electrode and conventional CMUT configurations. However, for a fair comparison, both electromechanical coupling coefficient and capacitance values should be evaluated as a function of applied DC bias normalized to their respective collapse voltages. The experimentally obtained capacitances and calculated electromechanical coupling coefficients as a function of normalized bias voltage are illustrated in Figure 70 and Figure 71 respectively.

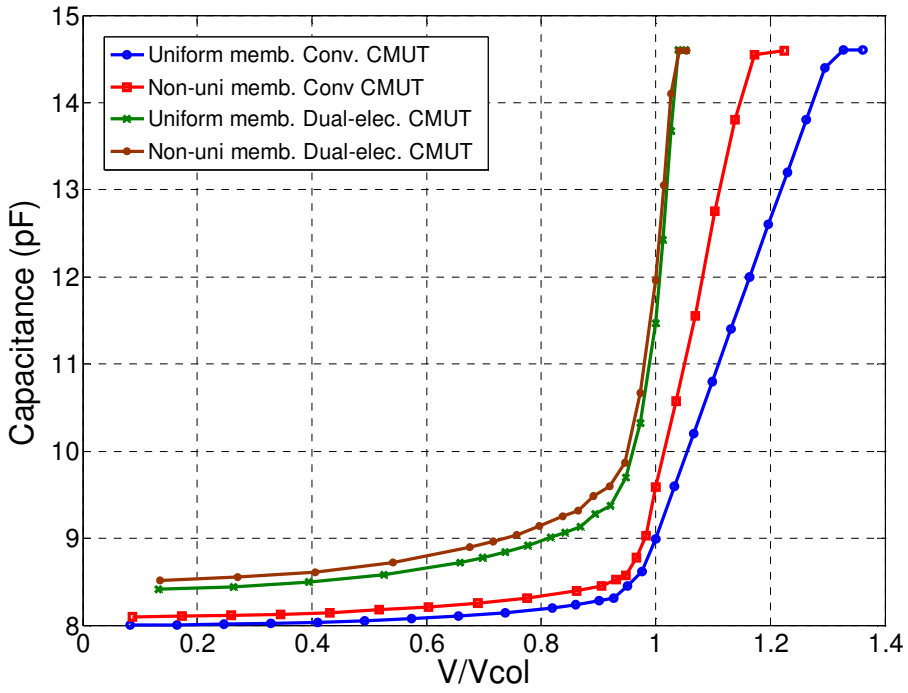

Figure 70 Experimentally measured capacitance as a function of normalized applied DC bias to respective collapse voltages

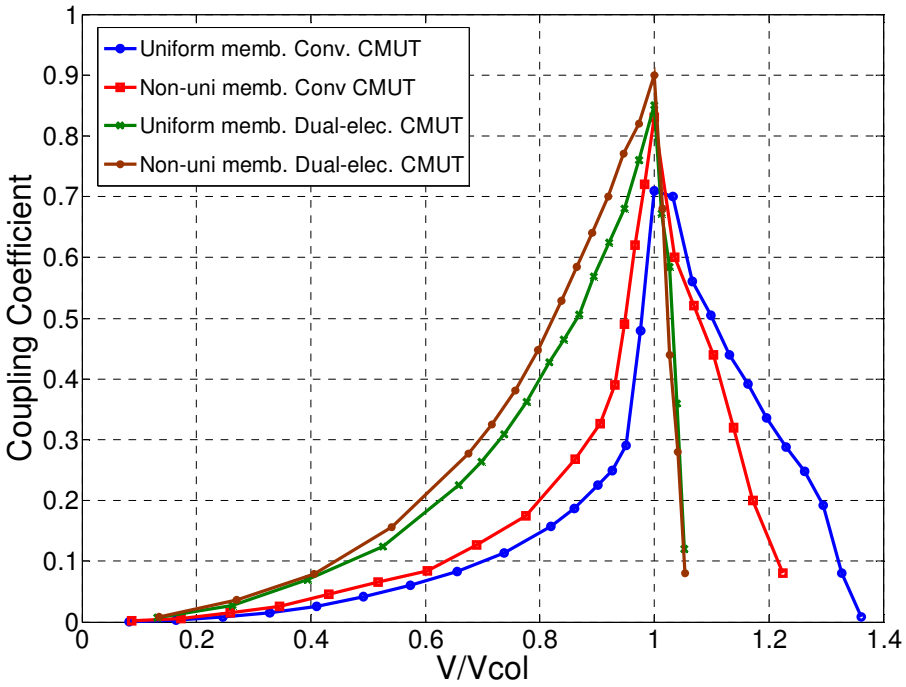

Figure 71 Calculated electromechanical coupling coefficient from experimentally measured capacitance as a function of normalized bias to respective collapse voltages

We observe from Figure 71 that the electromechanical coupling coefficient is significantly increased with dual electrode structure and adding center mass to the design. For instance, at 90% of the collapse, the uniform conventional CMUT achieves an electromechanical coupling coefficient of 0.28. When the non-uniform membrane structure is employed in the conventional CMUT design, the electromechanical coupling coefficient is increased at 90% of the collapse to 0.40. This corresponds to a significant increase in the transducer performance considering that with center mass introduction, the collapse voltage is reduced from 122V to 116V. On the same graph, one can compare conventional and dual-electrode CMUT with uniform membrane. At 90% of the collapse, the dual-electrode structure attain electromechanical coupling coefficient of 0.72. Note that the side and center electrode bias for the dual-electrode CMUT is 160V and 76V respectively. Moreover, one can observe the effect of non-uniform membrane on the

dual-electrode CMUT performance from Figure 71 as well. Non-uniform membrane dual-electrode CMUT design increases the electromechanical coupling coefficient to 0.82. Note that this performance improvement is obtained with reduction of side electrode bias to 132V from 160V, while center electrode bias is changed to 74V from 76V. The coupling coefficient at 90% of collapse and corresponding operation bias values obtained from Figure 71 are summarized in Table 17.

Table 17 Summary of coupling coefficient and applied bias values for uniform/non-uniform membrane conventional and dual-electrode CMUTs

	Center electrode bias (V)	Side electrode bias (V)	Coupling coefficient (90% of collapse)
Uniform membrane conventional CMUT	122	0	0.28
Non-uniform membrane conventional CMUT	116	0	0.40
Uniform membrane dual-electrode CMUT	76	160	0.72
Non-uniform membrane dual-electrode CMUT	74	132	0.82

We observe both from Figure 68 and Figure 71 that the capacitance of the uniform membrane conventional CMUT with no bias applied is 8pF. Analytical capacitance formulation (equation (8) and (9)) with the membrane parameters listed in Table 9 results in the active device capacitance of 5pF. Hence the experimental set-up, SMA connections, wires and overlapping top and bottom electrode regions accounts for the remaining 3pF. To validate this hypothesis, a dual-electrode CMUT array is diced in a way to remove all active membrane region but not the electrical connections to bondpads.

Then the wirebonded top and bottom electrode is tested in the same network analyzer setup (Figure 67). The test reveals a 3.1 pF capacitance value. Hence the parasitic capacitance value is validated. Moreover, in the experiments, the capacitance for the collapsed membrane is measured as 14.6pF. When analytical formulation given in equation (8) and (9) is used with "0" gap height, the capacitance is obtained as 14.65pF with 3.1pF of parasitic capacitance. This also verifies the accuracy of our measurement and "parallel-plate like" motion of the CMUT membrane. The experiments illustrate that the parasitic capacitance (3.1pF) does not change as a function of applied bias. Hence, the parasitic capacitance value can be subtracted from experimental data of Figure 70 to obtain the experimental active capacitance measurement as illustrated in Figure 72. The calculated electromechanical coupling coefficients without parasitic capacitance are illustrated in Figure 73. Simulated coupling coefficients are illustrated in Figure 74 for comparison purposes.

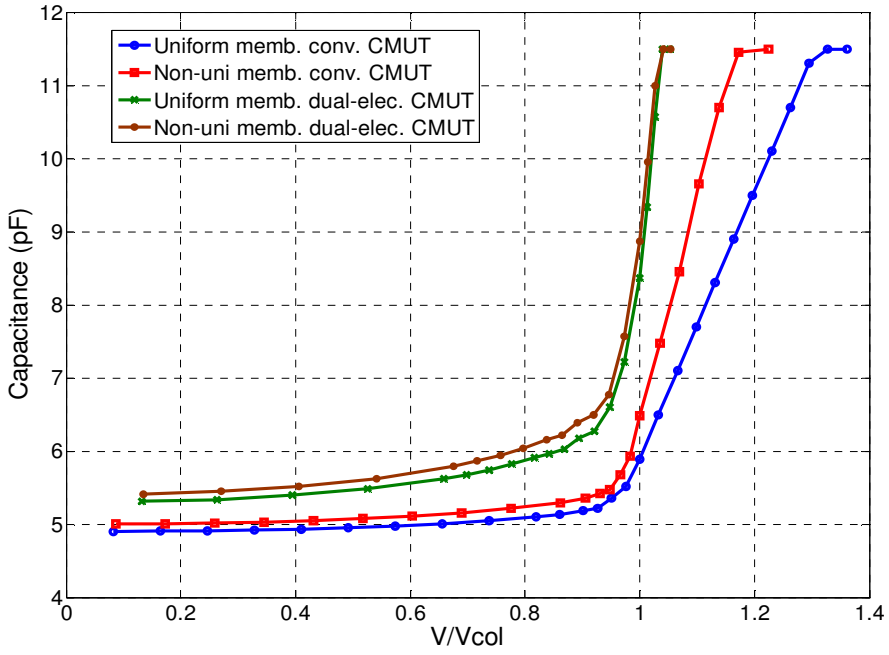

Figure 72 Experimentally measured capacitance with no parasitic capacitance as a function of normalized applied DC bias to respective collapse voltages

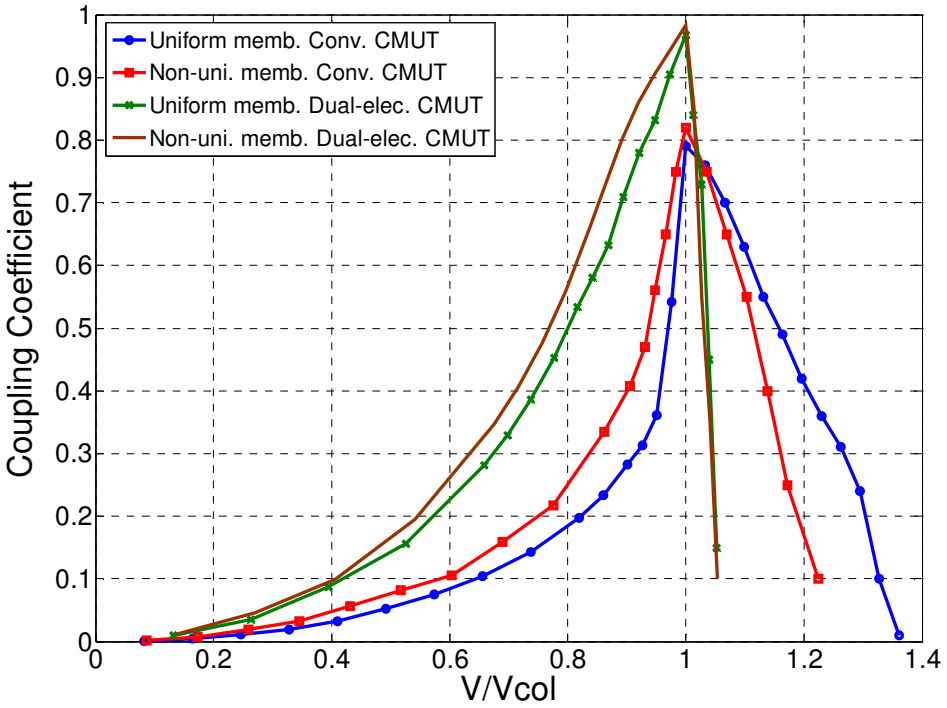

Figure 73 Calculated electromechanical coupling coefficient with no parasitic capacitance from experimentally measured capacitance data

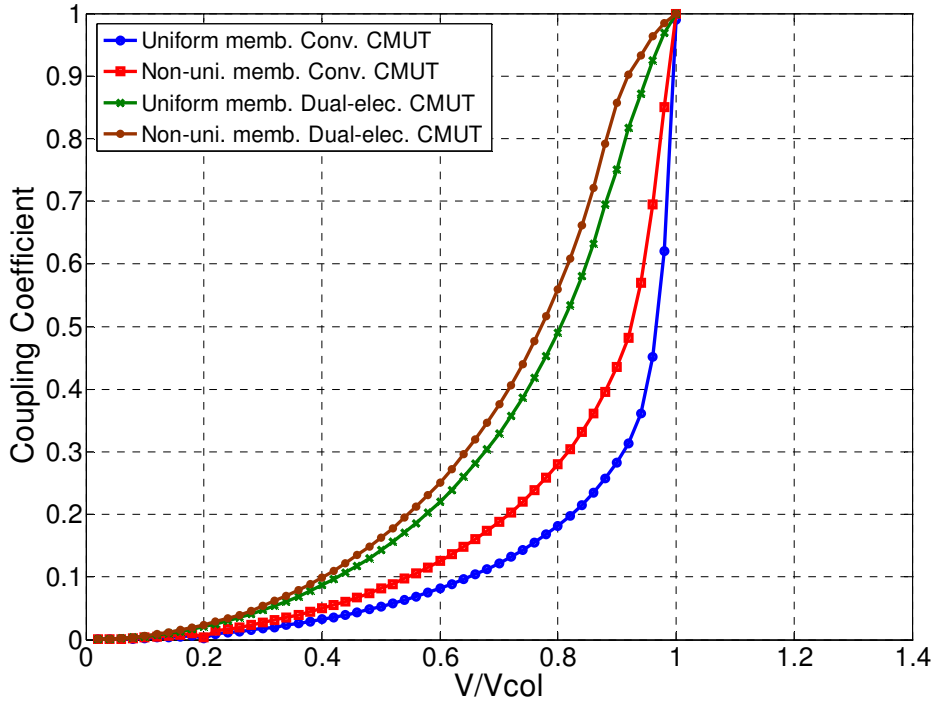

Figure 74 Simulated electromechanical coupling coefficient as a function of normalized voltage (no parasitic capacitance in simulations)

We observe that the experimental results (Figure 73) and simulation results (Figure 74) agree very well up to 95% of the collapse. The fabricated array has 48 membranes connected in series; slight non-uniformity in the fabrication may cause some membranes to collapse with less bias than others. As a result, there is a slight discrepancy between experimental and simulation data near collapse. Note that the simulations developed are not capable of handling contact analysis.

6.1.3 Transmission Measurements

6.1.3.1 Uniform Membrane Results

To compare the effect of membrane shaping by the side electrodes on the frequency response of the uniform membrane dual-electrode CMUT, pulsed excitation experiments are performed. The setup used in the pulsed excitation measurements is illustrated in Figure 75. In this experiment, two neighboring elements of a dual-electrode CMUT array are used. One dual-electrode CMUT array element is used for the transmission operation. This element is excited with a short transmit pulse using the side electrodes. The neighboring array element is used for receive mode of operation. The center electrode receives the echo (transmitted by the side electrodes of the neighboring array element) from a flat aluminum reflector in oil at a distance of 7 mm away. The received echo waveforms and corresponding frequency spectra are shown in Figure 76 (a) and (b), respectively.

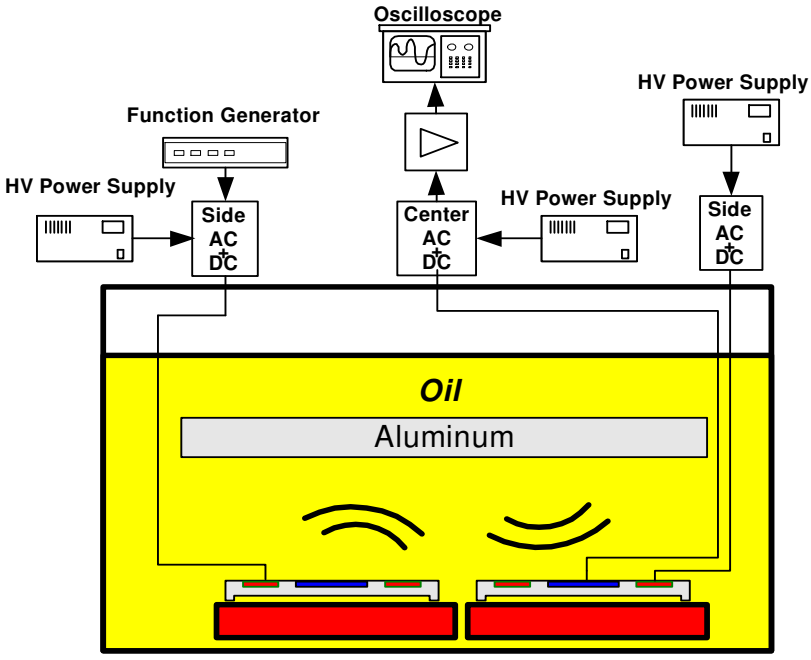

Figure 75 Experimental setup used for dual-electrode CMUT pulsed excitation experiments

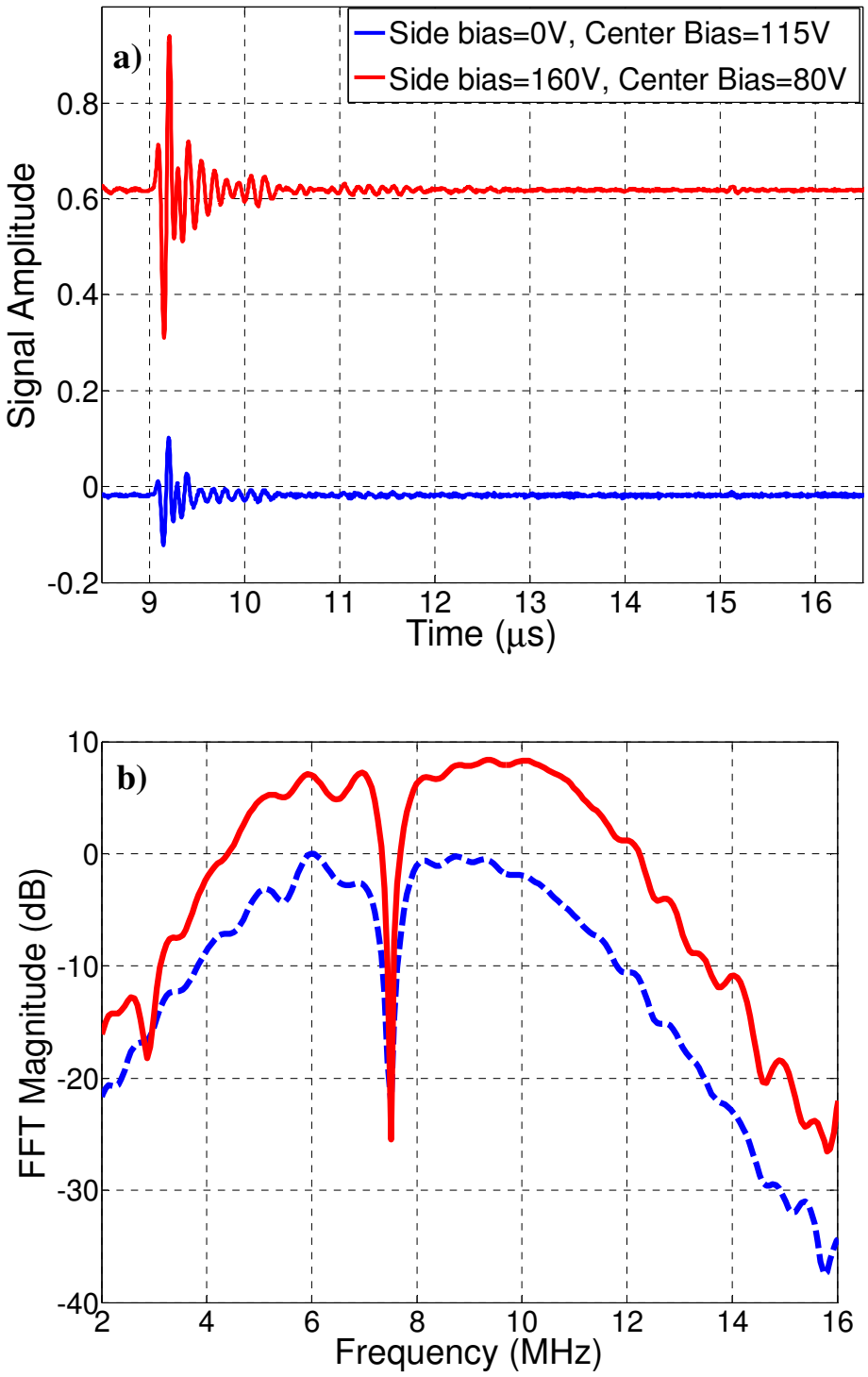

Figure 76 (a) Experimental received waveforms with the center electrode of the dual-electrode CMUT for different bias voltages. (b) Frequency response of the signals in (a).

The bottom blue traces (dashed in Figure 76 (b)) correspond to the time and frequency response at operational point A in Figure 66 (a), while the top red traces correspond to the response at point B. Received echo signal amplitude is increased by 9dB (2.8×) with membrane shaping by the side electrodes showing the effect of having a smaller gap. Both time signals in Figure 76 (a) show similar characteristics including the long tail due to ringing in the un-backed silicon substrate which can be eliminated by placing a matched and lossy backing material in contact with the silicon substrate [72]. This resonance causes a dip around 7.5MHz in the frequency response, which is centered around 8MHz as designed. Since the dual electrode structure is obtained by simply changing the top electrode pattern, the dynamics of the device are not changed significantly. In the pulse excitation experiment results (Figure 76 (b)) the frequency response comparison shows that side electrode biasing shifts the center frequency to a higher value, by about 15%, as predicted well by the finite element model. Consequently, improvement with dual-electrode CMUTs as compared to conventional CMUTs are not constant as a function of frequency; the average 6dB bandwidth improvement is 9dB, while the performance improvement at 10MHz is 10dB which matches the results shown in Figure 66.

Furthermore, output pressure generated by the uniform membrane dual-electrode CMUT array element is measured in a water tank using both the center and side electrodes as transmitters. A broadband calibrated hydrophone (GL series hydrophone, ONDA Corp., Sunnyvale, CA 94089) is used as a receiver. The same dual-electrode CMUT used in receive mode experiments is coated with 3μm thick parylene-C layer for electrical isolation and used as transmitter. Figure 77 illustrates the setup used in transmit

mode characterization experiment. The operation frequency of the CMUT is shifted to 12 MHz from 9MHz due to the parylene layer, as predicted by FEA simulations. The DC bias is set to half of the collapse voltage for either the center or the side electrode so that the maximum AC voltage can be applied without collapse. Therefore, the bias is set to 60V for the center electrode (side electrode 0V) and 120V for the side electrodes (center electrode 0V). A 10 cycle tone burst signal at 12MHz is applied to each set of electrodes with varying voltage levels. The output pressure is measured by the hydrophone located 7mm from the dual-electrode CMUT. The signal is then compensated for diffraction in water and pressure output on the membrane is obtained. For a fair comparison, the output pressure values are equated by normalizing to the width of the electrodes, i.e. the center electrode actuation values are scaled by a factor 20/15. The pressure output on the membrane surface as a function of AC amplitude is illustrated in the Figure 78 as discrete points (circle for center electrode, rectangle for side electrodes). Conventional CMUT operation generates a maximum of 0.66MPa of peak pressure on the membrane while the dual-electrode can generate 1.6MPa of peak pressure. The simulated output pressure on the membrane is illustrated in the same figure by the solid line for the side electrodes and by the dashed line for the center electrode. The output pressure on the fluid structure interface (FSI) node is directly obtained from the FEA simulation.

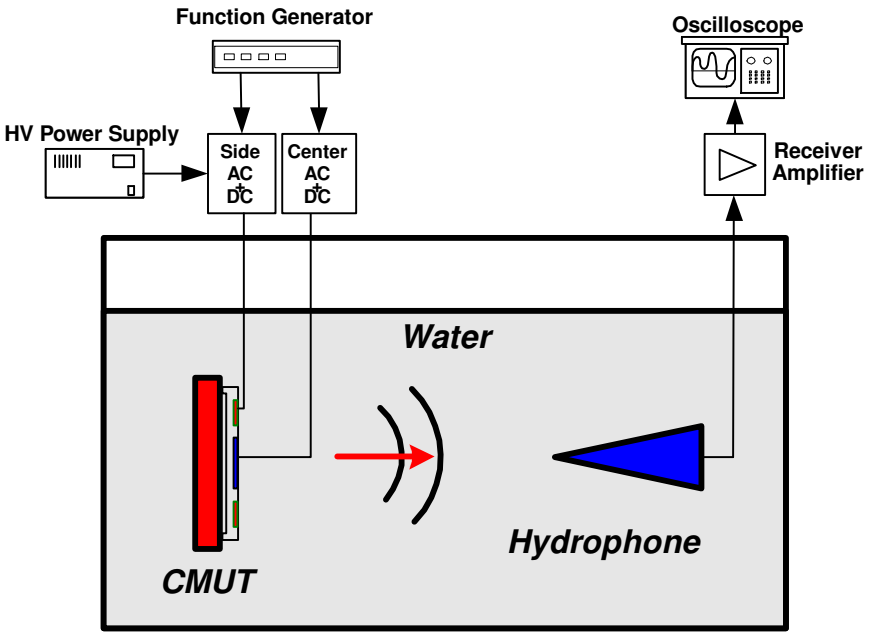

Figure 77 Experimental setup used for dual-electrode CMUT pressure output experiments

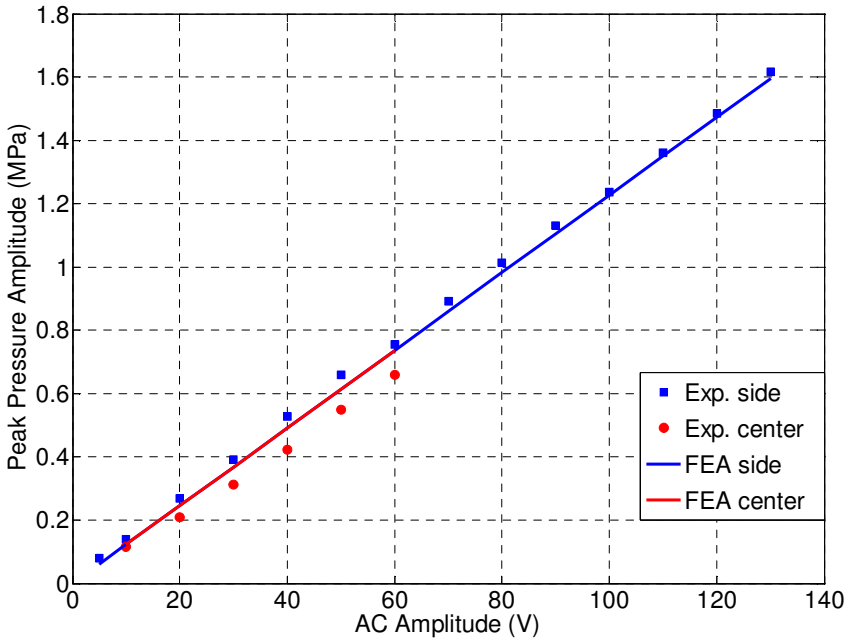

Figure 78 Experimental and simulated output pressure on the surface of the CMUT membrane as a function of AC input swing voltage for center and side excitation of the dual-electrode CMUT.

Dual-electrode CMUTs improve the maximum pressure output without going into the collapse region or applying large pulses which reduces one's control on the frequency spectrum of the generated pressure signals. As can be observed from Figure 78, the Pa/V efficiency is not increased with the dual-electrode CMUT. However the dual-electrode configuration enables higher net output pressure values (in Pa) by allowing increased transmit swing via higher AC voltages applied without collapse. Transmission performance increase comes at a cost of increased voltage values both for AC and DC values. The results show that the dual-electrode CMUT increases the maximum transmit pressure by 7.4dB. These results are also predicted well by finite element simulations (Figure 66). Therefore, the use of these analysis techniques for further design and optimization studies is well justified. These results indicate an overall transduction improvement of 16.4dB over a conventional CMUT with the same geometry, a significant advance in CMUT performance.

6.1.3.2 Non-Uniform Membrane Results

To obtain the bandwidth and transmit mode performance improvements with non-uniform membrane structure, two experiments that use the CMUT as transmitter and calibrated hydrophone (GL series hydrophone, ONDA Corp., Sunnyvale, CA 94089) as the receiver are conducted (Figure 77). In the first experiment, side electrodes of the uniform membrane dual-electrode CMUT with parameters given in Table 9 are used as a transmitter and this data serves as a reference. In the second experiment, the side electrodes of the optimized non-uniform membrane dual-electrode CMUT with physical membrane parameters summarized in Table 16 are used as transmitter. A 20ns, 10V

amplitude (peak) AC pulse, along with 230V and 190V DC bias is applied to the uniform and non-uniform membrane dual-electrode CMUTs respectively. These collapse voltages agree well with simulation results summarized in Table 12. The transmission frequency response of uniform and non-uniform membrane dual-electrode CMUTs is illustrated in Figure 79. There are several important results that can be observed from Figure 79. First, both uniform and non-uniform membrane dual-electrode CMUTs operate around 9MHz. This shows the accuracy of developed frequency response simulations and that experimental results can be used to compare two similar transducers. From the same figure, one can obtain the 3-dB one way fractional bandwidth of uniform and non-uniform dual-electrode CMUTs to be 82% and 136% respectively. The increase in fractional bandwidth is a very significant result as the axial resolution of the image depends on the bandwidth. Figure 80 illustrates the simulated maximum velocity for both uniform and non-uniform membrane dual-electrode CMUTs. We observe from this figure that uniform and non-uniform membrane dual-electrode CMUTs have 3dB fractional bandwidth of 80% and 140% respectively. The simulation and experimental results agree very well. Moreover, from Figure 79, when the experimental peak amplitude of the frequency response for non-uniform and uniform membrane dual-electrode CMUTs are compared, non-uniform membrane achieves 2.1dB higher transmission performance as compared to the uniform membrane. Simulation results also indicate a 2dB higher maximum velocity with the non-uniform membrane dual-electrode CMUT. The simulation and experimental transmission performance is in excellent agreement as well.

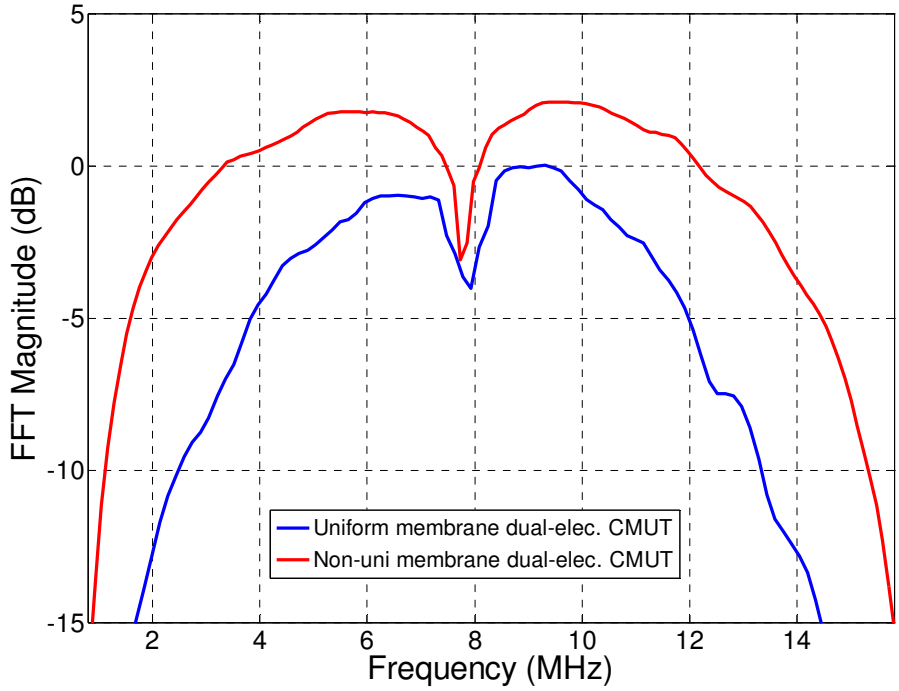

Figure 79 Experimental frequency response of received waveforms transmitted by the side electrodes of uniform/non-uniform membrane dual-electrode CMUTs

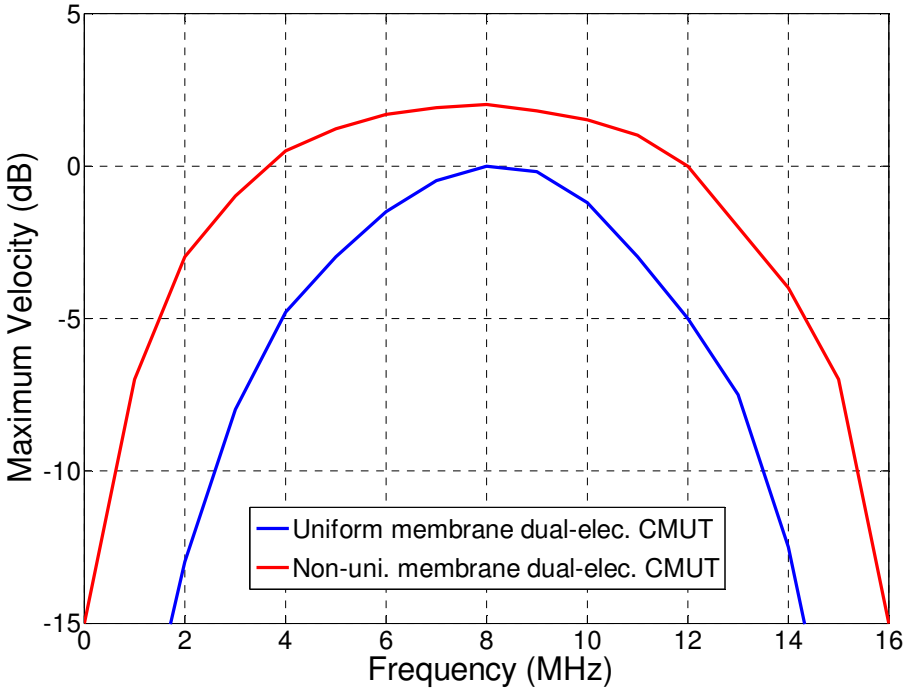

Figure 80 Simulated maximum velocity amplitude as a function of frequency for both uniform and non-uniform membrane dual-electrode CMUT

6.1.3 Electrical Isolation Measurements

To verify the simulated electrical isolation results for various medium of interest, a series of experiments are conducted by measuring active and cross-capacitance values. A network analyzer (Agilent 8753 ES) is used to obtain capacitance values. The active receive center electrode is connected to 1st port of the network analyzer and the side electrodes are connected to the 2nd port of the network analyzer. During the experiments, the active receive capacitance is obtained by measuring reflection coefficient (S11 parameter) and cross-talk capacitance is obtained by measuring the transmission coefficient (S12 parameter). Then electrical isolation value ($C_{receive}/C_{cross}$) is obtained by off-line post-processing. Both experimental and simulated results for air-oil-water operation are summarized in Table 18. The effect of parylene on the electrical isolation is summarized in the same table.

Table 18 Measured and simulated electrical isolation for air-oil-water operation and the effect of parylene

Medium	Parylene Thickness(μm)	Predicted isolation (dB)	Measured isolation (dB)
Air	0	37.2	38.6
Oil	0	34.7	35.2
Water	0	21.7	23.1
	2	28.0	27.9
	6	31.8	32.0

One can observe from Table 18 that for all air-oil-water medium of interests, the experimental and simulations results are within 2dB. Moreover, the electrical isolation improvement method – addition of parylene – is also experimentally verified. Overall, the simulation and experiments agree very well considering the fact that the parasitic capacitances and other electrical cross-talk sources other than the membrane are not accounted for in the simulations. For all medium of interest, electrical isolation of 32dB or more is experimentally shown. This is a reasonable isolation that does not significantly affect the image quality.

6.2 Pulse-echo Experiments

6.2.1 Dual-Electrode and Conventional CMUT Comparison on a Tissue Mimicking Phantom

To compare realistic imaging results achievable with conventional and dual-electrode CMUTs, pulse-echo experiments from tissue mimicking phantom is performed. The picture of the tissue mimicking phantom and setup that is used for the experiments are illustrated in Figure 81 (a) and (b) respectively. The tissue mimicking phantom has a tube at the center with properties to a blood vessel. In this experiment, two neighboring elements of a dual-electrode CMUT array are used. One dual-electrode CMUT array element is used for the transmission operation. The neighboring array element is essentially used for the receive mode of operation. The experiment is repeated for two cases. In the first experiment, the center electrodes of both transmitter and receiver are used (no bias on side electrodes). This case simulates the conventional CMUT. For the second experiment, side electrodes of transmitter are used for transmit mode of operation. The echo is detected by the center electrode of receiver while the side electrodes are used

for membrane shaping. As explained before, this is optimal operation for the dual-electrode CMUT configuration. The dual-electrode CMUT that is used in these experiments has 25µm center and 6µm side electrodes. The geometrical parameters, except electrode size, are as summarized in Table 9. Previous studies indicated that 50 to 75% top electrode coverage is optimal for conventional CMUTs [13, 68]. The center electrode size of 25µm (52% coverage) for the dual-electrode CMUT geometry maximizes the performance for conventional CMUTs. The tissue mimicking phantom is 6 mm away from the CMUT array. Received echo waveforms are shown in Figure 82.

a)

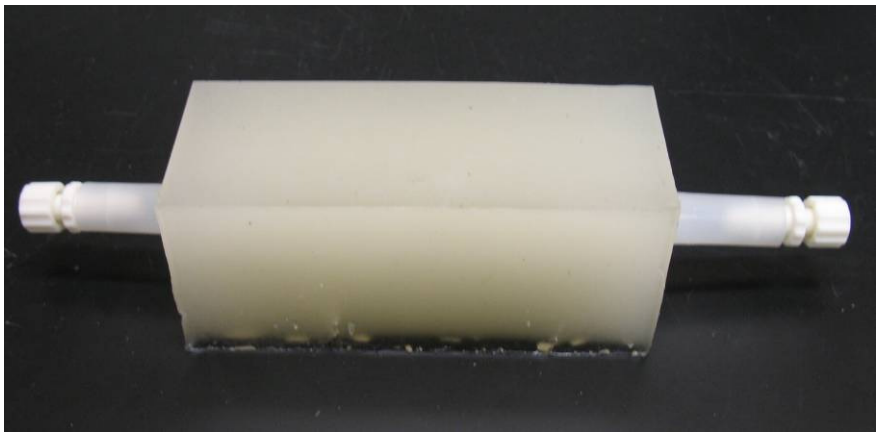

b)

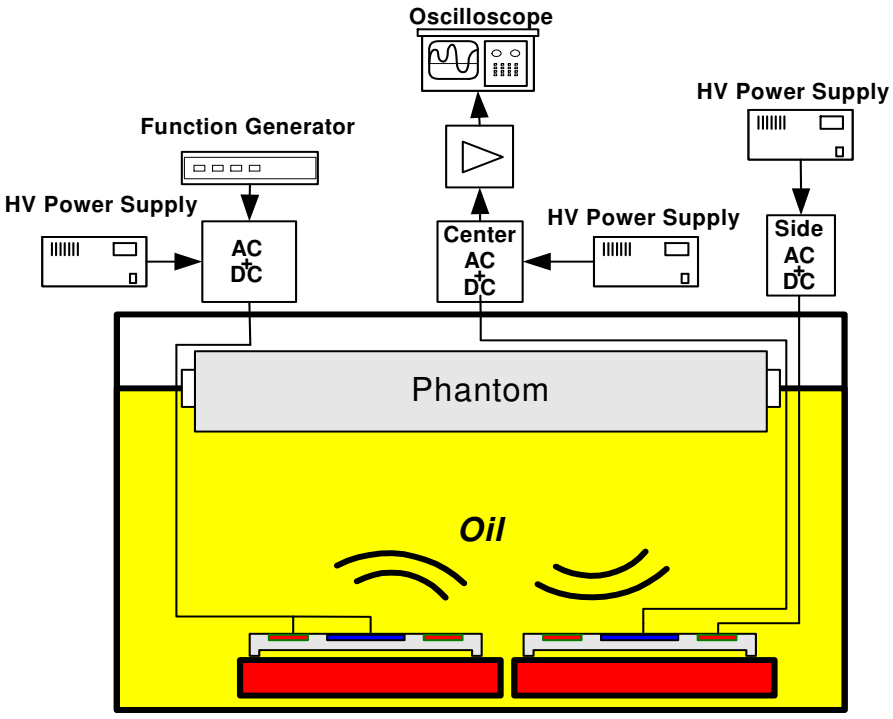

Figure 81 a) Picture of the tissue mimicking phantom b) Experimental setup used in the conventional and dual-electrode comparison experiments

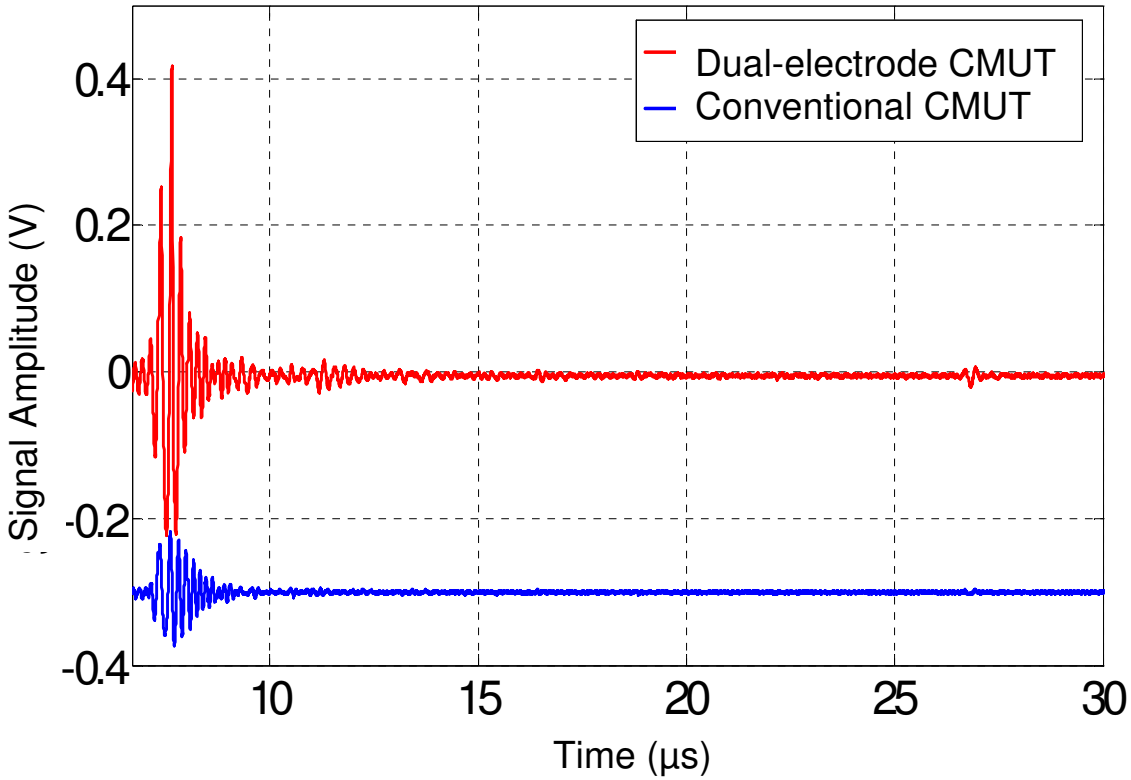

Figure 82 Experimental received waveforms for conventional and dual-electrode comparison experiments

The bottom blue curve in Figure 82 is the waveform obtained by the conventional CMUT and the top red curve is obtained by using dual-electrode CMUT configuration. One can observe from Figure 82 that the oil-phantom boundary is observed around 8µs by both conventional and dual-electrode CMUT. However, received pulse-echo amplitude is 13.4dB (4.4×) more with the dual electrode configuration as compared to the conventional CMUT. Note that the center electrode size for the dual-electrode CMUT used in this experiment is optimized for the conventional CMUT; as a result, the dual-electrode operation is not optimized. When the static simulations are repeated with the electrode sizes used in the experiments, the transduction performance increase with dual-electrode structure is obtained as 13.2dB. As a result, there is an excellent match between

simulation and experimental result. One can also observe from Figure 82 that both dual-electrode and conventional CMUTs detect the scatterings coming from tissue inside of the phantom. More importantly, at 27μs, the dual-electrode CMUT detects the tube inside of the phantom (as shown in Figure 81 (a)), while the amplitude of the signal detected by the conventional CMUT is smaller than the noise floor. Note that the vessel mimicking tube is located about 2cm (27 μs) from the CMUT array. As a result, this experiment illustrates the increased penetration depth by the dual electrode structure.

6.2.2 Pulse-Echo Experiments with Dynamic Biasing

To demonstrate the potential of dual-electrode CMUTs for real-time imaging applications where the array elements are mostly mono-statically operated, experiments are performed by dynamically biasing the side electrodes between transmit and receive cycles of a single pulse-echo event. A moderate bias voltage is needed during the transmit mode for a large transmit swing which increases the output pressure such as point C in Figure 66 (a). After the transmit pulse is emitted, the operating point is shifted so that during the receive mode of the same cycle the gap is reduced which in turn increases the sensitivity while keeping the center electrode bias constant (point B in Figure 66 (a)). As illustrated by the experimental schematic of Figure 83, the output of two signal generators are added to obtain the desired dynamic bias waveform as well as the tone burst transmit signal. The output of the adder is connected to a high-voltage, high-speed amplifier (TDA9535, ST Microelectronic, Geneva, Switzerland) which drive the side electrodes. The center electrode is connected to the TIA. A DC voltage is applied to the bottom electrode to provide the required bias levels avoiding the bias voltage

limitation of the specific high-voltage amplifier used. The oil-air interface 9.5mm away from the transducer is used as the reflection surface.

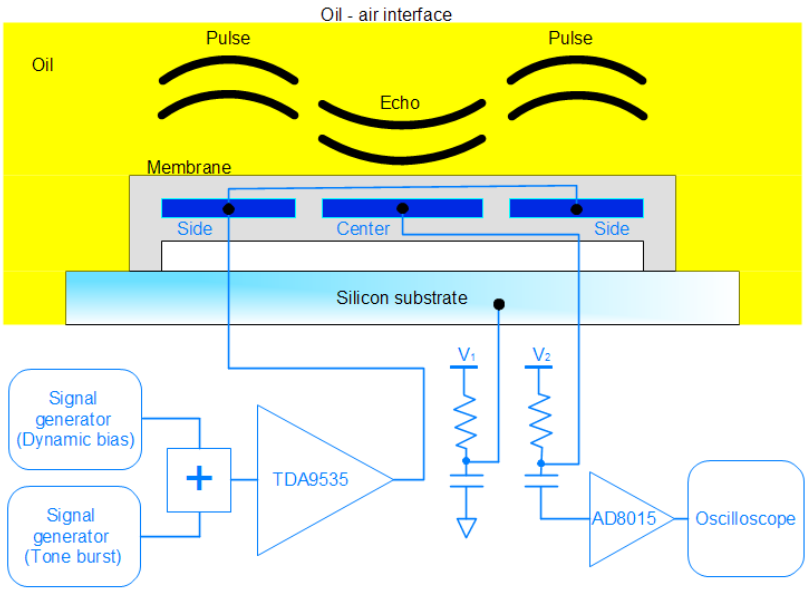

Figure 83 Experimental setup used in the pulse-echo experiments.

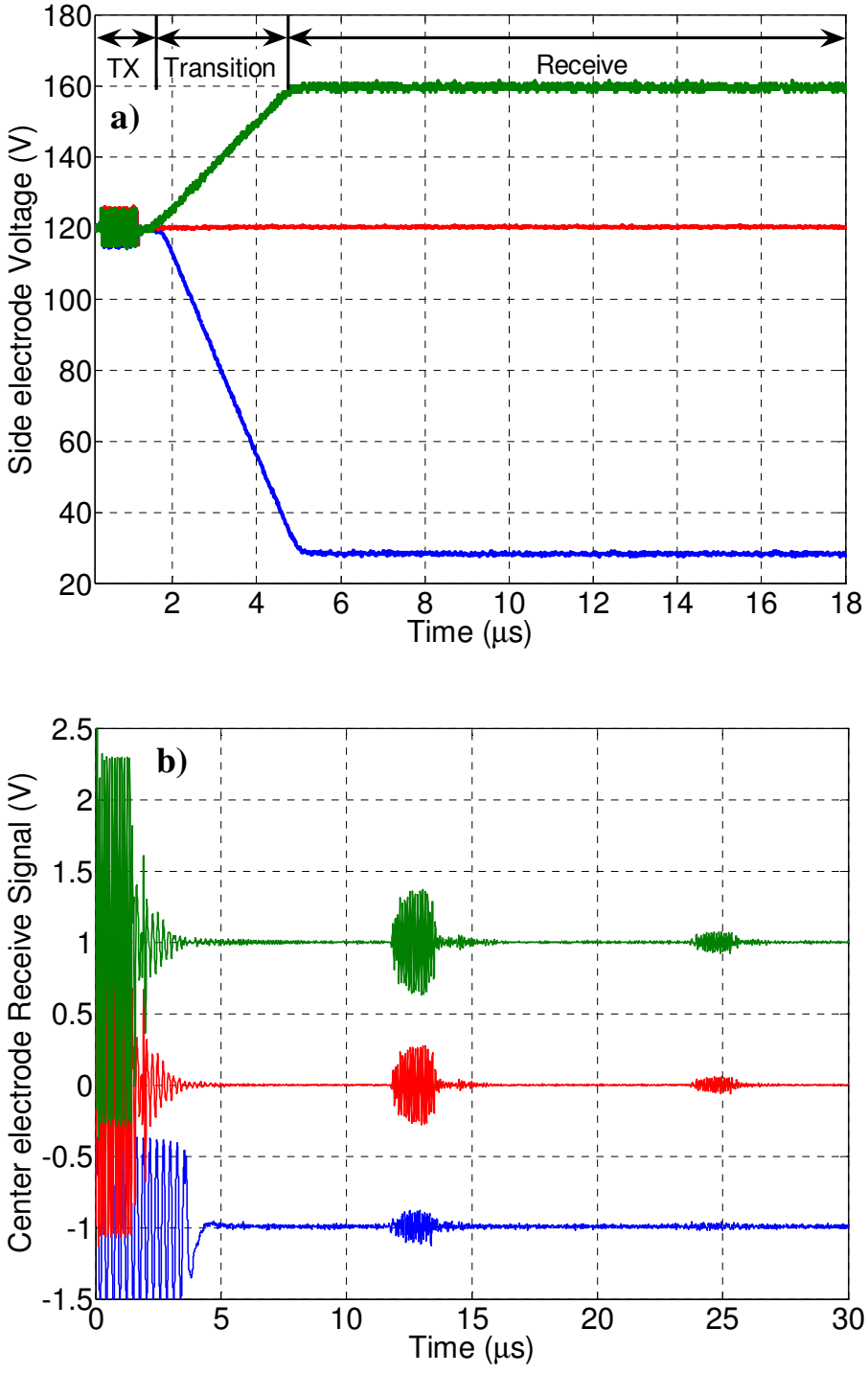

Figure 84 The dynamic bias plus the tone burst signal applied to the side electrodes during pulse-echo experiment. (b) Echo signals received by the center electrode corresponding to the side electrode voltages in (a)

Figure 84 (a) shows the three different voltage waveforms applied to the side electrodes to demonstrate the effect of dynamic membrane shaping during a single pulse-echo cycle. During the transmit phase, a 120V bias and a 15 cycle, 10V peak-to-peak tone burst at 10 MHz is applied to the side electrodes during the transmit cycle. Then receive biases are set after a 3μs long transition phase. For the bottom trace, the center electrode bias is set to 115V while the side electrode bias is reduced from 120V to 30V [point D in Figure 66. (a)] during the receive phase. For the middle trace, the center electrode bias is set to 80V and the side electrode bias is kept at 120V [point C in Figure 66 (a)]. For the top trace, the center electrode bias is kept constant at 80V while the side electrode bias is dynamically increased to 160V [point B in Figure 66 (a)]. Note that identical transmit DC bias of 120V and tone burst amplitude of 10V is applied to the side electrodes for all three cases. The first case, marked by point D in Figure 66 (a), approximately simulates the conventional operation (no side electrode bias) during the receive phase. Due to the limitation in the electronics, a 30V bias is applied to the side electrodes during the receive phase. The maximum receive signal obtained with a 30V side bias is only 1.5 percent more as compared to the one obtained with no side electrode bias showing that this case is indeed close to the no bias case as predicted by the simulations [point A in Figure 66. (a)]. The corresponding echo waveforms received by the center electrode are shown in Figure 84 (b). These waveforms are filtered by a high pass filter with 4 MHz cutoff frequency to remove the effects of the slowly varying bias transition region. From Figure 84 (b) one can observe that the received signal amplitude is increased by 6.5dB (2.1×) with 120V side electrode bias and 80V center electrode bias (middle trace) as compared to the bottom trace, which corresponds to the conventional

CMUT operation with bias level close to the collapse voltage. With the optimal receive phase parameters for this particular device (160V side electrode and 80V center electrode bias) results in the top trace showing a 10dB (3.2 ×) increase in the center electrode receive sensitivity. The pulse-echo results with dynamic biasing are summarized in Table 19. This performance improvement is in agreement with the receive sensitivity measurements (Figure 66) and pulsed excitation measurements (Figure 76). It can be observed from Figure 84 that the direct coupling from the transmit burst dies out in less then 2μs for this particular case. Also note that the initial coupling with a 30V side electrode bias case is longer because of the 5MHz ringing in the electronics. This transition region can be further reduced with electronics specifically designed for this application. In these experiments the transition region is set to be linear in shape with 3μs in duration. This section can be shaped differently to achieve time gain compensation and can be reduced in duration to minimize the dead zone. Finally, it needs to be noted that the pulse-echo experiments are performed without a T/R switch or protection circuitry.

Table 19 Summary of pulse-echo operational points for conventional and dual electrode CMUTs with dynamic biasing

	Transmit Side Electrode Bias (V)	Side Electrode Bias (V)	Center Electrode Bias (V)	Pulse-echo Amplitude (V)
Top Curve	120	160	80	0.815
Middle Curve	120	120	80	0.55
Bottom Curve	120	30	115	0.258

6.3 Charging Measurements

Before discussing the experimental results and its matching accuracy with simulations, one important concept should be investigated: charging. It is important to obtain the same results from the transducer over the period of experiment. The main source of charging in CMUTs is the trapped charges in the dielectric layer between the top and bottom electrodes. However, the elimination of the dielectric layer is not possible as when the membrane collapses there will be short circuit between the top and bottom electrodes. Charging may alter the signal amplitudes during experiments. In some extreme case, charging may put the close to collapse operating CMUT into collapse mode over a period of time. To investigate this charging phenomenon, an experiment is conducted using the side electrodes of the dual-electrode CMUT as transmitter and piezoelectric transducer as a receiver. A short transmit pulse, along with close to collapse DC bias of 235V (collapse voltage: 240V) is applied to transmitter CMUT. During the experiment, every 10 minutes, the signal amplitude is recorded and the bias is reduced to 0 V from 235V and the zero bias signal amplitude is recorded, then; the bias is increased to 235V in 10V/s ramp. The experiment is repeated for 10 hours (600 minutes). The results are illustrated in Figure 85.

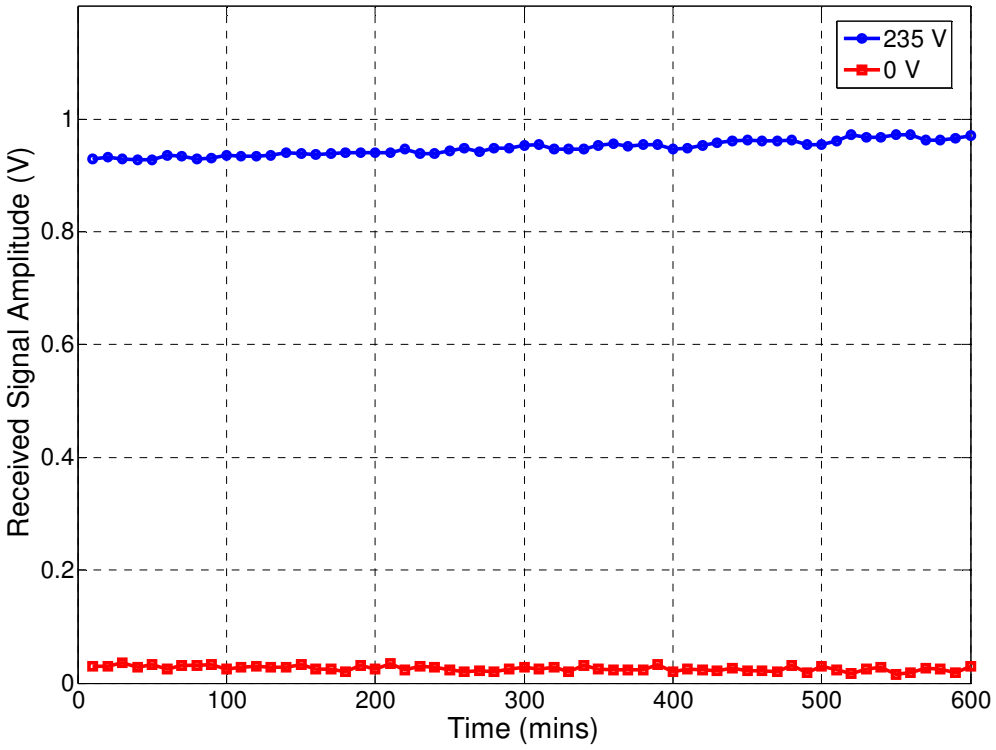

Figure 85 Experimentally recorded signal amplitude transmitted by using the side electrodes of the dual-electrode CMUT for charging experiments

One can observe from Figure 85 that over the period of 10 hours, the charging has little to no effect on received signal amplitude. Received signal amplitude with 235V DC bias is 0.9501±0.0225. This corresponds to maximum change of 2.3% (0.17dB) over 10 hour interval. This results show that the fabricated CMUTs do not have significant charging issues to affect the experimental results used to verify the simulation improvements.

6.4 Discussion

The predicted improvements over the conventional CMUT design are verified by experimental studies. First, a complete characterization study of uniform and non-uniform membrane dual-electrode CMUT is performed, then the experimental electromechanical coupling coefficient (k_c^2) is measured and the performance improvements are verified both for uniform/non-uniform membrane dual-electrode CMUTs. The results indicate that with non-uniform membrane dual-electrode CMUT, electromechanical coupling coefficient (k_c^2) increases from 0.24 to 0.85 (at 90% of the collapse) while reducing the DC bias from 160V to 132V. It is important to note that with non-uniform membrane dual-electrode CMUTs, the high coupling coefficient is obtained for a larger absolute and normalized voltage range as compared to conventional CMUT. This capability allows reliable and high performance operation by compensating for the non-uniformity among CMUT array elements. Moreover, a substantial increase in the transducers fractional bandwidth (136% vs. 82%) is also demonstrated by the non-uniform membrane dual-electrode CMUT structure. With this membrane shape adjustment, significant performance improvement (nearly 20dB) is achieved with dual-electrode CMUT structure that enables the CMUT performance to exceed that of piezoelectric transducers.

CHAPTER 7

CONCLUSION

Capacitive Micromachined Ultrasonic Transducers (CMUTs) are introduced as a viable alternative to piezoelectric transducers in medical ultrasound imaging in the last decade. CMUTs are especially suitable for applications requiring small size such as catheter based cardiovascular applications. Moreover, CMUTs offer advantages such as ease of manufacture, electronics integration, CMOS compatibility, low cost and reliability due to microfabrication implementation. Despite these advantages and their broad bandwidth, earlier studies indicated that the overall sensitivity of CMUTs needs to be improved to match piezoelectric transducers. Throughout the course of this research, dual-electrode capacitive micromachined ultrasonic transducer (CMUT) implementation is developed to address this design issue. Dual-electrode CMUTs have three electrodes in the membrane, the center electrode is only used for receive mode operation. The electrically connected side electrodes, on the other hand, are used both in transmit and receive operation. In receive mode, membrane shaping by side electrodes result in increased active capacitance (receive sensitivity); in transmit mode, increased membrane displacement by the side electrode actuation increases the net output pressure for a given gap thickness. Judicious usage of side electrodes enables increased displacement of the membrane exceeding 1/3 of the gap which is the limit for conventional CMUTs.

In the conventional CMUT design with a single top electrode in the membrane, the design space is limited as there is a trade-off between gain and bandwidth of the transducer [32]. For a constant frequency operation, the membrane thickness-width pair

can be adjusted to increase either the gain (efficiency) or the bandwidth. The dual electrode CMUT concept introduced in this thesis increases the gain significantly (~16dB) as compared to conventional CMUTs while not altering the bandwidth of the transducer. This performance increase is achieved by better use of the gap thickness. Moreover, non-uniform membrane designs increase the bandwidth significantly while simultaneously increasing the gain of the transducer by ~3dB. Hence as illustrated in this study, by using non-uniform membrane implementation to dual-electrode CMUTs, very high gain (efficiency) transducers with very high bandwidth as compared to conventional CMUTs are obtained. Both experimental and simulation studies indicated ~20dB gain in transducer performance and 140% fractional bandwidth with non-uniform membrane dual-electrode CMUTs. This significant increase in transducer performance *and* bandwidth obtained by non-uniform membrane dual-electrode CMUTs are expected to have broad impact in medical ultrasonic imaging.

7.1 Summary

To predict the performance improvements achievable with dual-electrode CMUT designs, coupled field finite element models are developed. The models are capable of predicting the collapse voltage, frequency response, transformer ratio, electromechanical coupling coefficient, and maximum transmitted output pressure. These simulations propose advanced transducers by increasing the transduction performance, bandwidth, penetration depth; ultimately increasing the medical ultrasonic image quality. The simulations show that unlike the parallel plate actuator case, the improvement in receive and transmit mode sensitivity is limited by the presence of the contact regime. In this regime, the bottom of the silicon nitride membrane underneath the center electrode makes

contact with the bottom surface which limits the performance improvements. However, the optimization studies indicated that reducing the isolation thickness between top and bottom electrodes increase the onset of the contact regime. The isolation thickness can be reduced significantly as long as the electrical isolation between top and bottom electrodes is preserved. It is also shown that the optimized uniform membrane dual-electrode CMUT increases receive sensitivity and output pressure by 9dB and 6.4dB respectively over its frequency spectrum. This results in total transduction improvement of 16.4dB. Note that the transduction performance of the CMUT is inferior by about 10dB as compared to piezoelectric transducers, especially due to lower output pressure [48, 49]. Hence, the performance improvement achieved by the dual-electrode CMUT is very significant. Note that this performance improvement comes at the cost of increased voltage requirement (160V versus 120V). However, the bias requirement reduces to 132V by employing a non-uniform membrane structure to the dual-electrode CMUT design. Moreover the non-uniform membrane dual-electrode CMUT increase the 3dB one-way fractional bandwidth to 140% from 80% and further increases the transduction performance to 19.9dB from 16.4dB. As an alternative to the non-uniform membrane implementation, placing notches between side and center electrode in the membrane is also investigated. Results indicated that the transduction performance is increased to 19.5dB with no significant change in either the collapse voltage or the fractional bandwidth. As a result, in terms of both performance and fabrication complexity, the non-uniform membrane implementation is superior to membrane with notches between side and center electrodes. Detailed electrical isolation of side and center electrode is also explored. The effect of membrane parameters to electrical isolation for air-oil-water

operation is documented. The electrical isolation improvement methods for air-oil-water operation are investigated. A reasonable electrical isolation (37.4dB, 36.6dB, 32.2dB for air-oil-water operation respectively) is obtained for uniform membrane dual-electrode CMUTs.

After designing the uniform and non-uniform membrane dual-electrode CMUTs using developed simulation codes, they are fabricated using surface micromachining process. This process requires only three commonly used micromachining equipments: Plasma Enhanced Chemical Vapor Deposition (PECVD), Reactive Ion Etch (RIE) and metal sputtering station. The PECVD based process uses a maximum process temperature of 250^{o}C which enables fabrication of the transducers directly on top of front-end electronics (CMUT-on-CMOS). To demonstrate the feasibility of this approach, a linear test array is fabricated on top of active electronics. The experimental results indicated both functioning electronic chips and transducers, post-CMUT fabrication. This proof of ceoncept demonstration is a key development in enabling commercialization of the CMUT technology for small size implementation such as forward-looking IVUS and ICE.

Finally, experimental studies are conducted to verify the performance improvements predicted by simulations both for uniform and non-uniform membrane dual-electrode CMUTs. For uniform membrane dual-electrode CMUT, a total performance improvement exceeding 16dB has been shown as compared to conventional CMUT which agree very well with simulations. In addition, 1.6MPa peak pressure levels on the CMUT membrane have been obtained with tone burst excitation in agreement with simulations. Moreover, the effect of a non-uniform membrane on conventional and dual-

electrode CMUT performance is quantified by obtaining the electromechanical coupling coefficient. Increased receive performance and reduced bias requirement by non-uniform membrane design as predicted by simulations is shown and electromechanical coupling coefficient of up to 0.95 is experimentally measured. In addition, the non-altered transmit frequency response; one way fractional bandwidth increase from 82% to 136% and transmit improvement of 2dB with the non-uniform membrane structure for dual-electrode CMUTs is illustrated. Pulse-echo operation of dual-electrode CMUTs with improved transducer performance is also shown. Experiments are done to illustrate the feasibility of dual-electrode CMUT implementation in real time ultrasonic imaging systems. This is achieved by dynamically adjusting the CMUT membrane geometry during transmit and receive phases of a single pulse-echo cycle by varying the side electrode bias voltage. Increased penetration depth and signal to noise ratio with dual-electrode CMUTs are also illustrated on a realistic imaging sample – a tissue mimicking phantom.

7.2 Recommendations

Along the course of this research, the foundation for dual-electrode CMUT concept is established. Intracardiac echocardiography (ICE) is selected as a suitable application, and array design is carried out for this specific imaging application. The next step for ICE imaging should be to fabricate non-uniform membrane dual-electrode CMUTs on CMOS electronics. With high transducer performance and bandwidth, real time imaging should be carried to reveal clearer images with this transducer technology. Comparison of non-uniform membrane dual-electrode CMUTs with piezoelectric transducers can be carried out, similar to the previous study [48] Moreover, the efficient

dual-electrode CMUT concept is expected to have broad impact in medical ultrasound imaging. Different medical imaging applications should be targeted that can benefit from the presence of higher performance and higher bandwidth transducers than the current state of the art piezoelectric transducers. With an application in mind, one can design very efficient transducers to achieve desired performance and operation frequencies.

The presence of side electrodes in the membrane can benefit harmonic imaging as well. Harmonic imaging is an ultrasound method in which the higher harmonic echoes of the fundamental frequency are selectively detected and used for imaging [73]. One can take advantage of higher order modes of CMUT membrane for harmonic imaging. Especially in dual-electrode CMUT design, the side electrodes can be placed at the peak locations of the third mode of the membrane. Non-uniform membrane approaches can be used to adjust the higher order mode frequencies to be multiples of the fundamental frequency [74]. This allows unique frequency control advantages at the transducer level for designing efficient harmonic imaging dual-electrode CMUTs.

Finally, the advantage offered by the dual electrode CMUT concept can be extended beyond the performance increase of the transducer. As shown in this thesis, the CMUT needs to be operated very close to collapse for increased coupling coefficient and performance, however slight non-uniformity within array elements may cause some membranes to collapse, which results in each array element responding differently. This non-uniformity can be controlled and compensated for by employing extra electrodes in the membrane. This compensation can be used for element non-uniformity within array or even between arrays. This capability is important for reliable operation CMUT arrays with a high number of elements.

REFERENCES

[1] J. L. Prince and J. M. Links, *Medical Imaging Signals and Systems*: Pearson Prentice Hall, 2006.

[2] T. L. Szabo, *Diagnostic Ultrasound Imaging*. Oxford, UK: Elsevier Academic Press, 2004.

[3] Y. Saijo and A. F. van der Steen, *Vascular Ultrasound*: Springer, 2003.

[4] http://www.medical.toshiba.com, (Data Accessed: November 2007).

[5] A. H. Association, "Heart Disease and Stroke Statistics-2008 Update," in *AHA, Dallas, Texas*, 2008.

[6] P. G. Yock and P. J. Fitzgerald, "Intravascular ultrasound: state of the art and future directions," *American Journal Cardiology,* vol. 81(7A), pp. 27E-32E, 1998.

[7] http://www.gehealthcare.com/usen/cardiology/index.html, (Data Accessed: November 2007).

[8] G. S. Kino, *Acoustic Waves: Devices, Imaging and Analog Signal Processing.* . Englewood Cliffs, NJ: Prentice-Hall, 1987.

[9] J. M. Cannata, J. A. Williams, Q. F. Zhou, T. A. Ritter, and K. K. Shung, "Development of a 35-MHz piezo-composite ultrasound array for medical imaging," *Ieee Transactions on Ultrasonics Ferroelectrics and Frequency Control,* vol. 53, pp. 224-236, Jan 2006.

[10] http://www.medical.philips.com/us, (Data Accessed: November 2007).

[11] http://www.bostonscientific.com/home.bsci, (Data Accessed: November 2007).

[12] B. Hadimioglu and B. T. Khuri-Yakub, "Polymer Films as Acoustic Matching Layers," in *IEEE Ultrasonics Symposium*, 1990, pp. 1337-1340.

[13] J. Knight and F. L. Degertekin, "Capacitive Micromachined Ultrasonic Transducers for Forward Looking Intravascular Imaging," in *IEEE Ultrasonics Symposium*, 2002, pp. 1052-5.

[14] D. W. Schindel, D. A. Hutchins, L. C. Zou, and M. Sayer, "The Design and Characterization of Micromachined Air-Coupled Capacitance Transducers," *IEEE Transactions on Ultrasonics Ferroelectrics and Frequency Control,* vol. 42, pp. 42-50, Jan 1995.

[15] P. Eccardt, K. Niderer, T. Scheiter, and C. Hierold, "Surface micromachined ultrasound transducers in CMOS technology," in *IEEE Ultrasonics Symposium*, 1996, pp. 959-62.

[16] G. T. A. Kovacs, *Micromachined Transducers Sourcebook*. New York, NY: McGraw-Hill, 1998.

[17] F. V. Hunt, *Electroacoustics: The analysis of transduction, and its historical background.* New York, NY: Acoustical Society of America, 1982.

[18] W. Kuhl, G. R. Schodder, and F. K. Schroder, "Condenser Transmitters and Microphones with Solid Dielectric for Airborne Ultrasonics," *Acustica,* vol. 4, pp. 519-532, 1954.

[19] J. H. Cantrell, J. S. Heyman, W. T. Yost, M. A. Torbett, and M. A. Breazeale, "Broad-Band Electrostatic Acoustic Transducer for Ultrasonic Measurements in Liquids," *Review of Scientific Instruments,* vol. 50, pp. 31-33, 1979.

[20] M. I. Haller and B. T. Khuri-Yakub, "A Surface Micromachined Electrostatic Ultrasonic Air Transducer," *IEEE Transactions on Ultrasonics Ferroelectrics and Frequency Control,* vol. 43, pp. 1-6, Nov 1996.

[21] R. C. Gonzalez and R. E. Woods, *Digital Image Processing*: Prentice-Hall, 2002.

[22] A. S. Ergun, S. Barnes, and E. Gardner, "An Assessment of the Thermal Efficiency of Capacitive Micromachined Ultrasonic Transducers," in *IEEE Ultrasonics Symposium*, 2007, pp. 420-423.

[23] H. T. Soh, I. Ladabaum, A. Atalar, C. F. Quate, and B. T. Khuri-Yakub, "Silicon Micromachined Ultrasonic Immersion Transducers," *Appl. Phys. Lett.,* vol. 69, pp. 3674-3676, 1996.

[24] I. Ladabaum, X. C. Jin, H. T. Soh, A. Atalar, and B. T. Khuri-Yakub, "Surface micromachined capacitive ultrasonic transducers," *IEEE Transactions on Ultrasonics Ferroelectrics and Frequency Control,* vol. 45, pp. 678-690, May 1998.

[25] A. Bozkurt, I. Ladabaum, A. Atalar, and B. T. Khuri-Yakub, "Theory and analysis of electrode size optimization for capacitive microfabricated ultrasonic transducers," *IEEE Transactions on Ultrasonics Ferroelectrics and Frequency Control,* vol. 46, pp. 1364-1374, Nov 1999.

[26] O. Oralkan, X. C. Jin, F. L. Degertekin, and B. T. Khuri-Yakub, "Simulation and experimental characterization of a 2-D capacitive micromachined ultrasonic transducer array element," *IEEE Transactions on Ultrasonics Ferroelectrics and Frequency Control,* vol. 46, pp. 1337-1340, Nov 1999.

[27] A. Caronti, G. Caliano, A. Iula, and M. Pappalardo, "An accurate model for capacitive micromachined ultrasonic transducers," *Ieee Transactions on Ultrasonics Ferroelectrics and Frequency Control,* vol. 49, pp. 159-168, Feb 2002.

[28] G. G. Yaralioglu, A. S. Ergun, B. Bayram, E. Haeggstrom, and B. T. Khuri-Yakub, "Calculation and Measurement of Electromechanical Coupling Coefficient of Capacitive Micromachined Ultrasonic Transducers," *IEEE Transactions on Ultrasonics Ferroelectrics and Frequency Control,* vol. 50, pp. 449-456, Apr 2003.

[29] C. G. Yaralioglu, A. S. Ergun, and B. T. Khuri-Yakub, "Finite-element analysis of capacitive micromachined ultrasonic transducers," *IEEE Transactions on Ultrasonics Ferroelectrics and Frequency Control,* vol. 52, pp. 2185-2198, Dec 2005.

[30] A. Ronnekleiv, "CMUT Array Modelling Through Free Acoustic CMUT Modes and Analysis of the Fluid CMUT Interface Through Fourier Transform Methods," *IEEE Transactions on Ultrasonics Ferroelectrics and Frequency Control,* vol. 52, pp. 2173-2184, Dec 2005.

[31] A. Lohfink and P. C. Eccardt, "Linear and nonlinear equivalent circuit modeling of CMUTs," *IEEE Transactions on Ultrasonics Ferroelectrics and Frequency Control,* vol. 52, pp. 2163-2172, Dec 2005.

[32] S. Olcum, M. N. Senlik, and A. Atalar, "Optimization of the Gain-Bandwidth Product of Capactive Micromachined Ultrasonic Transducers," *IEEE Transactions on Ultrasonics Ferroelectrics and Frequency Control,* vol. 52, pp. 2211-2219, Dec 2005.

[33] D. Certon, F. Teston, and F. Patat, "A finite Difference Model for CMUT Devices," *IEEE Transactions on Ultrasonics Ferroelectrics and Frequency Control,* vol. 52, pp. 2199-2210, Nov 2005.

[34] X. C. Jin, I. Ladabaum, F. L. Degertekin, S. Calmes, and B. T. Khuri-Yakub, "Fabrication and characterization of surface micromachined capacitive ultrasonic immersion transducers," *IEEE Journal of Microelectromechanical Systems,* vol. 8, pp. 100-14, 1999.

[35] O. Ahrens, A. Buhrdorf, D. Hohlfeld, L. Tebje, and J. Binder, "Fabrication of gap-optimized cMUT," *Ieee Transactions on Ultrasonics Ferroelectrics and Frequency Control,* vol. 49, pp. 1321-1329, Sep 2002.

[36] E. Cianci, L. Visigalli, V. Foglietti, G. Caliano, and M. Pappalardo, "Improvements toward a reliable fabrication process for CMUT," *Microelectronic Engineering,* vol. 67-68, pp. 602-608, 2003.

[37] Y. L. Huang, A. S. Ergun, E. Haeggstrom, M. H. Badi, and B. T. Khuri-Yakub, "Fabricating capacitive micromachined ultrasonic transducers with wafer-bonding technology," *Journal of Microelectromechanical Systems,* vol. 12, pp. 128-137, Apr 2003.

[38] J. Knight, J. McLean, and F. L. Degertekin, "Low Temperature Fabrication of Immersion Capacitive Micromachined Ultrasonic Transducers on Silicon and Dielectric Substrates," *IEEE Transactions on Ultrasonics Ferroelectrics and Frequency Control,* vol. 51, pp. 1324-1333, Oct 2004.

[39] A. Caronti, A. Savoia, G. Caliano, and M. Pappalardo, "Design, fabrication and characterization of a capacitive micromachined ultrasonic probe for medical imaging," *IEEE Transactions on Ultrasonics Ferroelectrics and Frequency Control,* vol. 52, pp. 2039-2046, Nov 2005.

[40] X. C. Jin, O. Oralkan, F. L. Degertekin, and B. T. Khuri-Yakub, "Characterization of one-dimensional capacitive micromachined ultrasonic immersion transducer arrays," *IEEE Transactions on Ultrasonics Ferroelectrics and Frequency Control,* vol. 48, pp. 750-760, May 2001.

[41] O. Oralkan, A. S. Ergun, J. A. Johnson, M. Karaman, U. Demirci, K. Kaviani, T. H. Lee, and B. T. Khuri-Yakub, "Capacitive Micromachined Ultrasonic Transducers: Next-generation arrays for acoustic imaging?," *IEEE Transactions on Ultrasonics Ferroelectrics and Frequency Control,* vol. 49, pp. 1596-1610, Nov 2002.

[42] O. Oralkan, A. S. Ergun, C. H. Cheng, J. A. Johnson, M. Karaman, T. H. Lee, and B. T. Khuri-Yakub, "Volumetric ultrasound Imaging using 2-D CMUT arrays," *IEEE Transactions on Ultrasonics Ferroelectrics and Frequency Control,* vol. 50, pp. 1581-1594, Nov 2003.

[43] U. Demirci, A. S. Ergun, O. Oralkan, M. Karaman, and B. T. Khuri-Yakub, "Forward-viewing CMUT arrays for medical Imaging," *IEEE Transactions on Ultrasonics Ferroelectrics and Frequency Control,* vol. 51, pp. 887-895, Jul 2004.

[44] F. L. Degertekin, R. O. Guldiken, and M. Karaman, "Micromachined capacitive transducer arrays for intravascular ultrasound," in *Proc. SPIE MOEMS Display and Imaging Systems III, San Jose, Ca*, 2005, pp. 104–114.

[45] F. L. Degertekin, R. O. Guldiken, and M. Karaman, "Annular-ring CMUT arrays for forward-looking IVUS: Transducer characterization and imaging," *IEEE Transactions on Ultrasonics Ferroelectrics and Frequency Control,* vol. 53, pp. 474-482, Feb 2006.

[46] D. T. Yeh, O. Oralkan, I. O. Wygant, M. O'Donnell, and B. T. Khuri-Yakub, "3-D ultrasound imaging using a forward-looking CMUT ring array for intravascular/intracardiac applications," *IEEE Transactions on Ultrasonics Ferroelectrics and Frequency Control,* vol. 53, pp. 1202-1211, Jun 2006.

[47] R. O. Guldiken, J. Zahorian, G. Gurun, M. S. Qureshi, M. Balantekin, C. Tekes, M. Karaman, S. G. Carlier, and F. L. Degertekin, "Forward-Looking IVUS Imaging Using a Dual-Annular Ring CMUT Array: Experimental Results," in *IEEE Ultrasonics Symposium*, 2007, pp. 1247-1250.

[48] D. M. Mills and L. S. Smith, "Real-time in-vivo imaging with capacitive micromachined ultrasound transducer (cMUT) linear arrays," in *IEEE Ultrasonics Symposium*, 2003, pp. 568 - 571.

[49] D. M. Mills, "Medical imaging with capacitive micromachined ultrasonic transducer arrays," in *IEEE Ultrasonics Symposium*, 2004, pp. 384-390.

[50] S. D. Senturia, *Microsystem Design*. Boston: Kluwer Academic Publishers Group, 2000.

[51] B. Bayram, E. Haeggstrom, G. G. Yaralioglu, and B. T. Khuri-Yakub, "A new regime for operating capacitive micromachined ultrasonic transducers," *IEEE Transactions on Ultrasonics Ferroelectrics and Frequency Control,* vol. 50, pp. 1184-1190, Sep 2003.

[52] O. Oralkan, B. Bayram, G. G. Yaralioglu, A. S. Ergun, M. Kupnik, D. T. Yeh, I. O. Wygant, and B. T. Khuri-Yakub, "Experimental characterization of collapse-mode CMUT operation," *IEEE Transactions on Ultrasonics Ferroelectrics and Frequency Control,* vol. 53, pp. 1513-1523, Aug 2006.

[53] B. Bayram, O. Oralkan, A. S. Ergun, E. Haeggstrom, G. G. Yaralioglu, and B. T. Khuri-Yakub, "Capacitive micromachined ultrasonic transducer design for high power transmission," *IEEE Transactions on Ultrasonics Ferroelectrics and Frequency Control,* vol. 52, pp. 326-39, Feb 2005.

[54] Y. Huang, E. Hæggström, X. Zhuang, A. S. Ergun, and B. T. Khuri-Yakub, "Capacitive micromachined ultrasonic transducers (CMUTs) with piston shaped membranes," in *IEEE Ultrasonics Symposium*, 2005, pp. 589-592.

[55] M. N. Senlik, S. Olcum, and A. Atalar, "Improved Performance of cMUT with Nonuniform Membranes," in *IEEE Ultrasonics Symposium*, 2005, pp. 597-600.

[56] R. O. Guldiken, M. Balantekin, and F. L. Degertekin, "Analysis and Design of Dual-electrode CMUTs," in *IEEE Ultrasonics Symposium*, 2005, pp. 581-584.

[57] S. Zhou, P. Reynolds, and J. A. Hossack, "Improving the Performance of Capacitive Micromachined Ultrasound Transducers using Modified Membrane and Support Structures," in *IEEE Ultrasonics Symposium*, 2005, pp. 1925-1928.

[58] W. P. Mason, *Electromechanical Transducers and Wave Filters*. New York, NY: Van Nostrand, 1948.

[59] E. S. Hung and S. D. Senturia, "Extending the travel range of analog-tuned electrostatic actuators," *Journal of Microelectromechanical Systems,* vol. 8, pp. 497-505, Dec 1999.

[60] Y. Huang, E. Hæggström, X. Zhuang, A. S. Ergun, and B. T. Khuri-Yakub, "Optimized Membrane Configuration Improves the cMUT Performance," in *IEEE Ultrasonics Symposium*, 2004.

[61] ANSYS, "Coupled Field Analysis Guide." vol. 11.0, 2007.

[62] A. Pierce, *Acoustics: An Introduction to Its Physical Principles and Applications*. New York, NY: Acoustical Society of America, 1981.

[63] D. Blackstock, *Fundamental of Physical Acoustics*: Wiley-Interscience, 2000.

[64] J. Fraser and P. Reynolds, "Finite-element method for determination of electromechanical coupling coefficient for piezoelectric and capacitive micromachined ultrasonic transducers," in *Joint 140th meeting of ASA/NOISE-CON*, 2000.

[65] D. Berlincourt, *Ultrasonic Transducer Materials*. New York, NY: Plenum Press, 1971.

[66] ANSYS, "Commands Reference." vol. 11.0, 2007.

[67] J. McLean, R. Guldiken, and F. L. Degertekin, "CMUTs with Dual Electrodes for Improved Transmit and Receive Operation," in *IEEE Ultrasonics Symposium*, 2004, pp. 501-504.

[68] B. Bayram, G. G. Yaralioglu, A. S. Ergun, and B. T. Khuri-Yakub, "Influence of the Electrode Size and Location on the Performance of a CMUT," in *IEEE Ultrasonics Symposium*, 2001, pp. 949-52.

[69] C. Daft, S. Calmes, D. d. Graca, K. Patel, P. Wagner, and I. Ladabaum, "Microfabricated Ultrasonic Transducers Monolithically Integrated with High Voltage Electronics," in *IEEE Ultrasonics Symposium*, 2004, pp. 493-96.

[70] S.-Y. Peng, M. S. Qureshi, A. Basu, R. O. Guldiken, F. L. Degertekin, and P. E. Hasler, "Floating-Gate Based CMUT Sensing Circuit Using Capacitive Feedback Charge Amplifier," in *IEEE Ultrasonics Symposium*, 2006, pp. 2425 - 2428

[71] R. O. Guldiken, J. McLean, and F. L. Degertekin, "CMUTS with dual-electrode structure for improved transmit and receive performance," *IEEE Transactions on Ultrasonics Ferroelectrics and Frequency Control,* vol. 53, pp. 483-491, Feb 2006.

[72] I. Ladabaum, P. Wagner, C. Zanelli, M. J, P. Reynolds, and W. G;, "Silicon substrate ringing in microfabricated ultrasonic transducers," in *IEEE Ultrasonics Symposium*, 2000, pp. 943-946.

[73] M. Frijlink, D. E. Goertz, L. C. A. van Damme, R. Krams, and A. F. van der Steen, "Intravascular Ultrasound Tissue Harmonic Imaging In Vivo," *IEEE Transactions on Ultrasonics Ferroelectrics and Frequency Control,* vol. 53, pp. 1844-1852, Oct 2006.

[74] N. A. Hall, R. Guldiken, J. McLean, and F. L. Degertekin, "Modeling and Design of cMUTs using Higher Order Vibration Modes for Harmonic Imaging," in *IEEE Ultrasonics Symposium*, 2004.